UNIVERSITY OF CALIFORNIA
RIVERSIDE

Synthesis of Graphene Layers from Metal-Carbon Melts: Nucleation and Growth Kinetics

A Dissertation submitted in partial satisfaction
of the requirements for the degree of

Doctor of Philosophy

in

Mechanical Engineering

by

Shaahin Amini

December 2012

Dissertation Committee:
Dr. Reza Abbaschian, Chairperson
Dr. Cengiz Ozkan
Dr. Javier Garay

The Dissertation of Shaahin Amini is approved:

_____

_____

_____

Committee Chairperson

University of California, Riverside

Acknowledgements

It gives me great pleasure to take this opportunity to acknowledge all the people who supported me in the last several years during my PhD here at UC Riverside.

Firstly, and most importantly, I would like to thank my thesis supervisor Professor Reza Abbaschian for his gracious support, and confidence in me in every step of the way, his patience, kindness, generosity and all the time he spent with me and for numerous critical and stimulating discussions and constructive suggestions. Certainly, these words are not sufficient and will not reflect my deepest gratitude for him. Without his motivation and enthusiasm, the completion of this thesis would not have been possible. He always inspired me by thinking positively and independently, in order to become an independent researcher. I was truly honored to work with him and at this point, all I can say is THANK YOU.

I would also like to acknowledge my internal thesis committee members, Professor Javier Garay and Professor Cengiz Ozkan for all the illuminating and fruitful discussions throughout the course of my research and for carefully reading my thesis and examining my results.

I am also grateful to Professor Alexander Balandin for his endless help and support since the very beginning to the end. I would also like to thank all the members of the Nano Device Laboratory within the Department of Electrical Engineering for providing me the access to their facilities and instruments.

I am grateful to all my friends, colleagues and staff in the Department of Mechanical Engineering at UC Riverside specifically Haamun Kalaantari, Melina Roshandell, Sam Pournazeri, Jun Wang, Roseanna Barron-Lopez, Katie Dell, Sarah Nosce, Paul Talavera, Eilene Montoya, Becki Jo Ray and Terry Traver for extending their unconditional help whenever needed.

Last but not least, I would like to thank my parents Reza and Novid, and my brothers, Arash and Shahram, from the bottom of my heart. I could not have come this far without their unconditional love, support and inspiration.

Shaahin Amini
Riverside
December 2012

We dance round in a ring and suppose. But the secret sits in the middle and knows.

Robert Frost (1874 –1963)

Dedicated to those people around the world struggling for their freedom

ABSTRACT OF THE DISSERTATION

Synthesis of Graphene Layers from Metal-Carbon Melts:
Nucleation and Growth Kinetics

by

Shaahin Amini

Doctor of Philosophy, Graduate Program in Mechanical Engineering
University of California, Riverside, Dec 2012
Dr. Reza Abbaschian, Chairperson

A new method for growth of large-area graphene, which can lead to a scalable low-cost high-throughput production technology, was demonstrated. The method is based on growing of graphene films on the surface of metal-carbon melts and involves dissolving carbon in a molten metal at a specified temperature and then allowing the dissolved carbon to nucleate and grow on top of the melt at a lower temperature. The synthesized graphene layers were subjected to detailed microscopic and Raman spectroscopic characterizations. The deconvolution of the Raman 2D band was used to accurately determine the number of atomic planes in the resulting graphene layers and access their quality. The results indicated that the technology can provide bulk graphite films, few-layer graphene as well as high-quality single layer graphene on metals. It was also shown that upon cooling of supersaturated metal-carbon melts; graphite would also grow inside the melt either with flake or sphere morphology, depending on the solidification rate and degree of supersaturation. At small solidification rates, graphite crystals are normally

bounded by faceted low index basal and prismatic planes which grow by lateral movement of ledges produced by 2D-nucleation or dislocations. At higher growth rates, however, both interfaces become kinetically rough, and growth becomes limited by diffusion of carbon to the growing interface. The roughening transition from faceted to non-faceted was found to depend on the driving force and nature of growing plane. Due to high number of C-C dangling bonds in prismatic face, its roughening transition occurs at smaller driving forces. At intermediate rates, the prismatic interfaces become rough and grow faster while the basal plane is still faceted, leading to formation of flake graphite. At higher growth rates, both interfaces grow with a relatively similar rate leading to initiation of graphite sphere formation, which later grows by a multi-stage growth mechanism. An analytical model was developed to describe the size and morphology of graphite as a function of solidification parameters.

Contents

List of Figure

Chapter I

Literature review

Graphite has been observed to grow during solidification of supersaturated metal-carbon melts with different morphologies. In this chapter, first the graphite crystal structure will be discussed. Then different morphologies of graphite which has been observed to grow within metal-carbon melts will be reviewed. The graphite growth mechanisms and kinetics as well as instabilities inside the melt are later discussed. Finally, the properties and preparation techniques of single layer graphene (graphite building block) will be reviewed.

1.1. Graphite crystal structure

Graphite has a layered structure that in each layer carbon atoms are arranged in a honeycomb lattice called *graphene*. In a graphene sheet each carbon atom is covalently bonded to three carbon atoms with sp^2 hybridization. Three out of four valence electrons of each carbon atom are used in a covalent σ-bond formation with three other carbon atoms in graphene lattice while the fourth electrons forms week Van der Waals forces or delocalized π-bonds. The graphite structure is built up by stacking of 2D graphene layers, as shown schematically in Fig. 1(a). The different inter- and intra-atomic bonding of carbon in graphene makes the graphite a strong anisotropic material with different properties normal and parallel to graphene stacks. For instance while graphite possesses good thermal and electrical conductivity parallel to graphene sheets (*a* direction), it is almost a thermal and electrical insulator normal to the sheet (*c* direction) [1]. In normal condition, graphite is bounded by low index planes of (0001) and $\{10\bar{1}0\}$ family which are the so-called *basal* and *prismatic* planes respectively. These planes have been marked

in the graphite crystal shown in Fig. 1(b). In some cases where the growth of graphite in prism face is unstable, the graphite crystal may be bounded by other planes than $\{10\bar{1}0\}$ family.

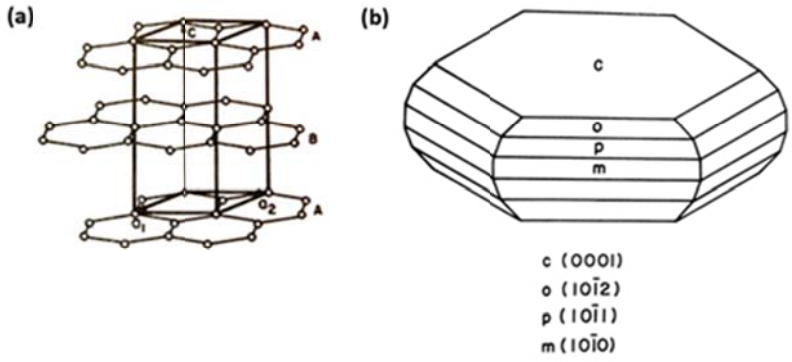

Fig. 1. a) graphite unit cell b) facets of graphite crystal in normal condition [2]

1.2. Metal-carbon systems

The graphite growth has been mostly investigated in metal-carbon systems of Fe, Ni and Co-C. The phase diagrams of these systems have been shown in Fig. 2.

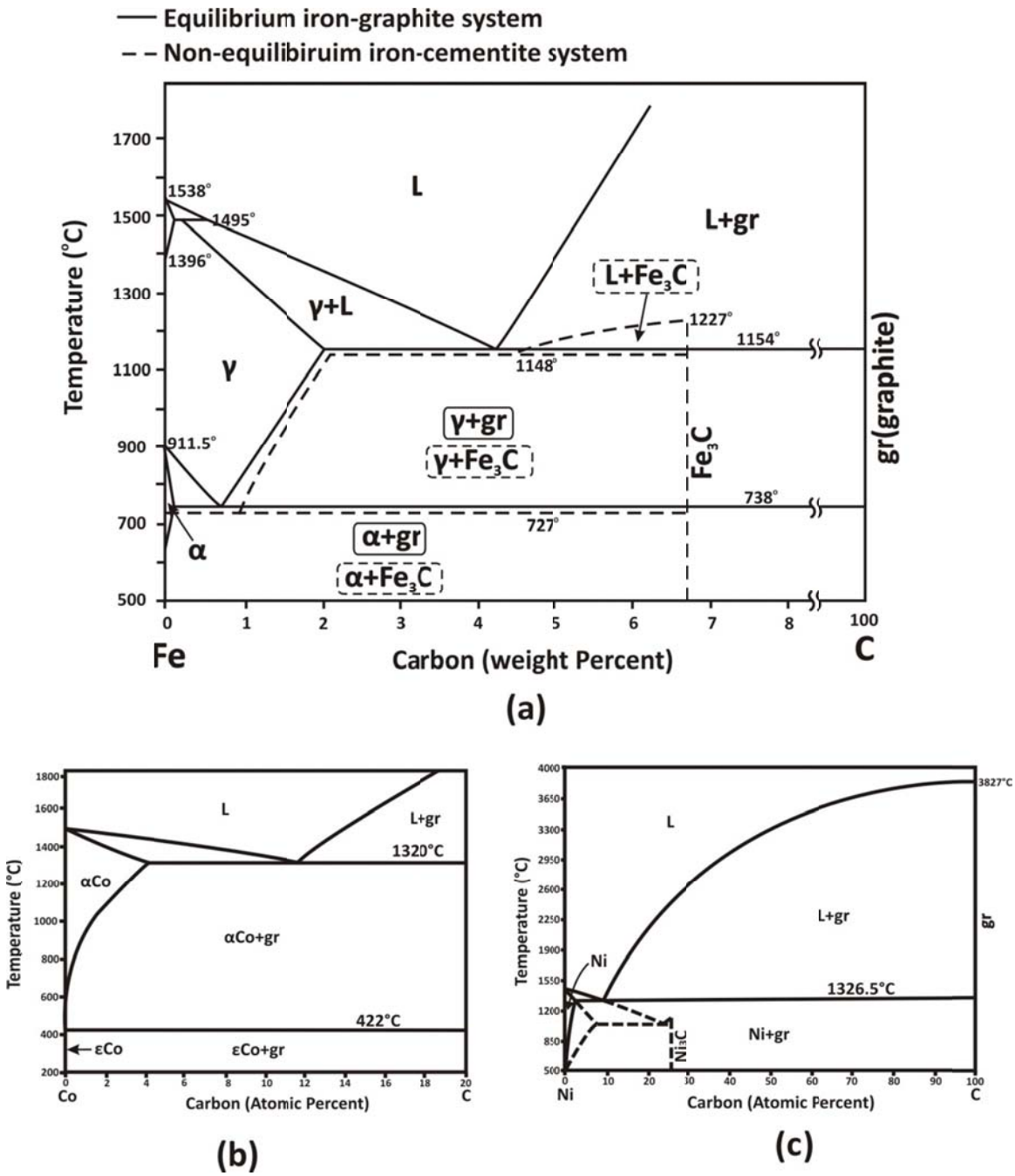

Fig. 2. Metal-carbon phase diagrams a) Fe-C [3] b) Ni-C [4] c) Co-C [5]

Phase diagrams in Fig. 2 contain simple eutectics at 1154, 1320 and 1326.5 °C and composition of nearly 4.2 wt%C, 10 and 12 at%C for Fe, Co and Ni respectively. Beside the graphite which is the stable form of carbon in these systems, there are also possibilities of metastable carbide formation. In Fig. 2(a) and (b) the iron-iron carbide (*cementite*, Fe_3C) and nickel-nickel carbide (Ni_3C) phase diagrams have been shown with dashed lines. Cementite is a metastable compound that decomposes into iron and graphite under some special heat treatments. Nickel carbide has also been observed to form in quenched Ni-C alloys [6]. The tendency to form graphite or carbide is regulated by the melt composition and cooling rate and will be discussed later in section 0.

Among the above systems, Fe-C has been drawn the most attention due to diversity of grown graphite morphologies which makes it the most important casting material with 75 percent of total world tonnage [7]. The Fe-C phase diagram in Fig. 2(a) shows carbon concentration below 7 wt%. This part of the diagram is practically in use and higher carbon concentrations are not industrially significant. Fe-C alloys with the composition less than 2 wt%C are generically called *steels*. It is also observed in diagram of Fig. 2(a) that iron alloys within the composition range of 3.0 and 4.5 wt%C are around the eutectic composition and become liquid at lower temperatures than the one for steel. Thus, iron alloys with this range of carbon are easily melted in lower temperature and suitable for casting. This is beneficial for those brittle Fe-C structures which are difficult to be fabricated by forming techniques. Due to the castability of these alloys, this group of iron materials is called *cast irons*.

1.3. Graphite growing from a melt

It has been observed that graphite grows during cooling of supersaturated metal-carbon melts with different morphologies. The graphite formation is of crucial importance since it will significantly affect the metal-graphite composite properties. For example when the graphite morphologies alter from flake to sphere, the fatigue properties of cast iron will dominantly improve [8]. The nucleation and growth of various graphite morphologies will be reviewed here.

1.4. Graphite nucleation

Similar to growth of any other crystal from a melt, the graphite growth initiates by its nucleation which is either homogenous or heterogeneous [2]. Homogenous nucleation occurs in the interior of a metastable melt and is only induced by random thermodynamic fluctuations and uninfluenced by any extrinsic surfaces. Heterogeneous nucleation, on the other hand, takes place on foreign sites such internal interfaces provided by inclusions or dispersed colloidal particles or through contact with crucible walls. These types of graphite nucleation will be discussed below [9-11].

1.4.1. Homogenous nucleation

The homogenous nucleation occurs by thermodynamic fluctuations and by no means of other effects and therefore has higher barrier energy and is more difficult to obtain [3, 10, 11]. However, in pure systems which are free from impurities, this type of nucleation

may be achieved. Homogenous nucleation of graphite has been suggested to be in the forms of straight or wrapped graphene layers and fullerenes.

1.4.1.1. Straight graphene nucleation

During cooling of a supersaturated melt, dissolved carbon atoms may come together and form graphene layers. It has been suggested that formation of a graphene layer is either by joining of six carbon atoms or by stepwise formation of hexagons [12], which have been shown schematically in Fig. 3.

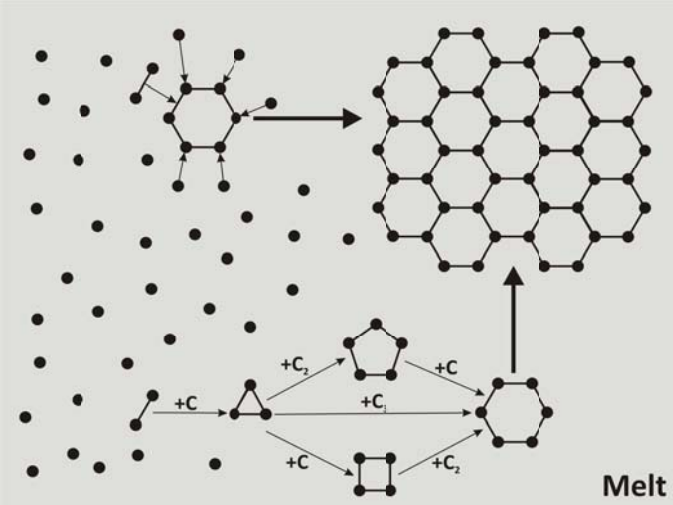

Fig. 3. Homogenous nucleation of a graphene sheet [12]

As the carbon atoms crystallize in a graphene lattice, the second nucleation event may similarly occur on this layer. Consequently, the graphene layers would then build up and form a stiff three-dimensional structure.

1.4.1.2. Wrapped graphene nucleation

Another possibility of homogenous nucleation is when the formed graphene sheets are wrapped within the melt. The wrapped graphene layers can form a loose ball or tangle containing ordered shells. The loose ball may grow epitaxially by addition of carbon atoms to steps of these shells. There is no identifiable barrier energy for this type of nucleation beyond the one for carbon addition in *a* directions [13]. The ball may eventually develop into a sphere and trap a few metal atoms inside [14, 15]. It is pertinent to point out that the graphene layers are prone to become wrapped in pure melts to reduce their surface energies [16, 17].

1.4.1.3. Fullerene nucleation

Another possibility of graphene homogenous nucleation is the formation of fullerene shells [1, 18]. Configurational considerations for a fullerene cage formation impose the presence of pentagonal and hexagonal rings together. The formation may begin by wrapping of two or three hexagons and later continue by additions of carbon atoms. Geometrically, 20 hexagons and 12 pentagons are required to form a fullerene cage. Based on the fullerene configurational limitation, formation of closed fullerene shells have very large driving force and accordingly low growth potential [13].

1.4.2. Heterogeneous nucleation

The heterogeneous nucleation typically takes place on foreign inclusions and thus will be the case for commercial melts which inevitably contain impurities [12, 19]. For instance,

commercial cast irons normally contain elements such as sulfur, silicon and oxygen and accordingly there is possibility of sulfides, silicates and oxides formations within the melt [20-24]. It should be noted that these inclusions may not have a high nucleation potential due to large lattice mismatch with graphite. However, if Me (Ca, Sr, or Ba) and Al elements are added to the melt, hexagonal silicate phases of the $MeO{\cdot}SiO_2$ or the $MeO{\cdot}Al_2O_3{\cdot}2SiO_2$ type can form on the surface of inclusions. The formations of these new phases create coherent or semicoherent interfaces between the inclusions and graphite which favor the heterogeneous nucleation [24].

1.5. Morphologies of graphite growing from a melt

Graphite crystals could grow within a molten phase with variety of morphologies. The ability of graphite to form different morphologies is due to its layered structure, different growth mechanisms in prismatic and basal planes, ability of graphene layers to bend during the growth and the effect of impurities. The graphite morphology which grows, however, depend on melt chemical composition and ratio of temperature gradient to growth rate (G/V) and/or cooling rate (G.V). Some of the most common morphologies of graphite crystals growing from the melt are discussed below.

1.5.1. Graphite flakes

Graphite may grow in the form of flake which is basically a plate-like morphology with higher lengthening rates than thickening. The group of cast iron in which the graphite grows with a flaky morphology called *gray cast irons*. Depending on the graphite growth

condition two types of flakes may form: The primary flakes which grow freely within the melt and the eutectic flakes which grow side by side of metallic phase. Below the morphologies of these two types are explained.

1.5.1.1. Primary flakes (type C)

The morphology of primary graphite flakes has been shown in Fig. 5(c). This form of graphite which is also called type C or *Kish* graphite possesses a straight flaky morphology with a few hundred micron length and a few tens of micron width. This morphology forms prior to eutectic temperature as the graphite grows freely within the melts of hypereutectic compositions without any constraints by the solid phase [8, 25, 26].

1.5.1.2. Eutectic flakes

The eutectic flakes form during a eutectic reaction and side by side of a metal. The growth of these flakes has been shown schematically in Fig. 4(a). It is observed in the figure that upon formation of graphite nucleus inside the melt, it branches out into some flakes. As these flakes grow, they consume the carbon atoms in their vicinity and favor the nucleation of metallic phase which later grow side by side of graphite in the form of spherical eutectic cells. Growing flakes may also change their crystallographic orientation and ultimately produce a fully interconnected plate-like structure [22, 27, 28]. One of these networks of flakes in a eutectic cell whose metallic phase etched away has been shown in Fig. 4(b). Comparing this figure with Fig. 5(c) depicts that eutectic flakes

are finer and more convoluted than the primary ones. This is due to lower growth temperature of eutectic flakes as well as the constraints applied by solid phase during their growth.

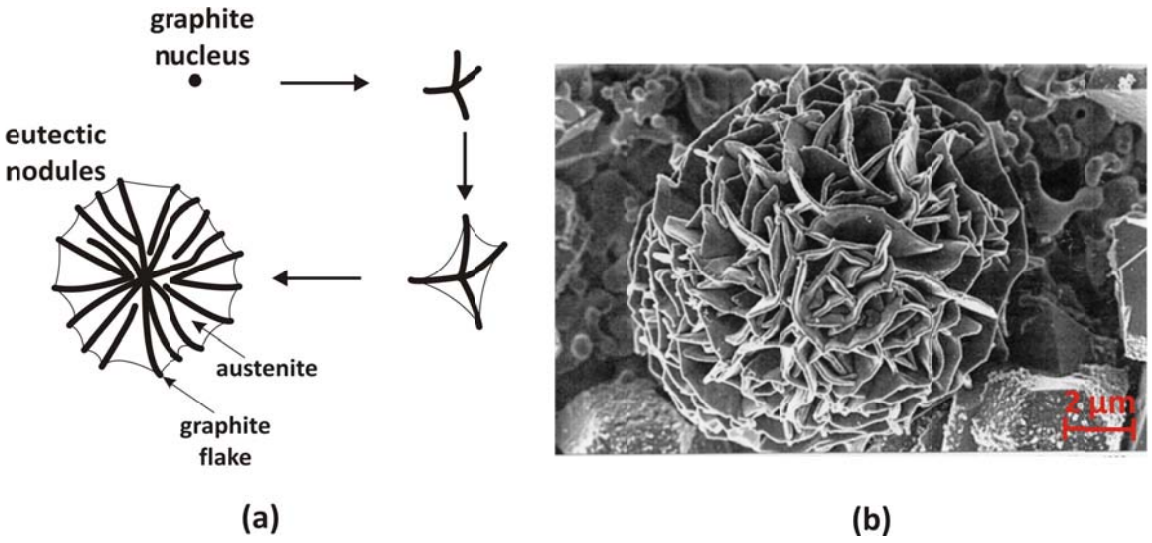

Fig. 4. (a) Schematic of graphite–metal eutectic cells formation (b) graphite flakes in a eutectic cell where the metallic phase etched away [29]

Generally when the cooling rate increases, the eutectic flakes get finer and they tend to form in between the metallic dendrites. According to their morphologies and distributions, eutectic flakes can be further subdivided into several groups which their formation not only depend on solidification conditions but also on the melt composition. Different types of graphite flakes will be described here briefly.

1.5.1.2.1. Type A flakes

The morphology of type A flakes has been shown in Fig. 5(a). It is observed that type A flakes possess a convoluted morphology and arrange in a randomly oriented pattern. Type A flakes form in the area of low cooling rates with a minimum amount of undercooling. Beside the cooling rate, changing the melt composition by addition of Al and Ca will also favor the formation of these flakes due to increase of graphitization potential and reduction of chilling tendency [8, 25, 26].

1.5.1.2.2. Type B flakes

The morphology of type B flakes has been shown in Fig. 5(b). It is observed that this type of flake is in the form of rosettes or clusters and grows in a mechanism similar to the one shown in Fig. 4(b). Type B graphite occurs in gray cast iron with near-eutectic composition which cools faster than the rates associated for type A flakes. This type of graphite forms in thin-walled castings or in the surface of thicker sections. [8, 25, 26].

1.5.1.2.3. Type D flakes

The morphology of type D flakes has been shown in Fig. 5(d). It is observed that these types of flakes possess very fine morphologies with a preferred orientation and a distinct pattern. Normally, they grow in between the metallic dendrites at the final stage of solidification. It should be noted that the formation of type B flake needs higher cooling rates than the one needed for Type A and B, yet lower than the one needed for carbide formation [8, 25, 26].

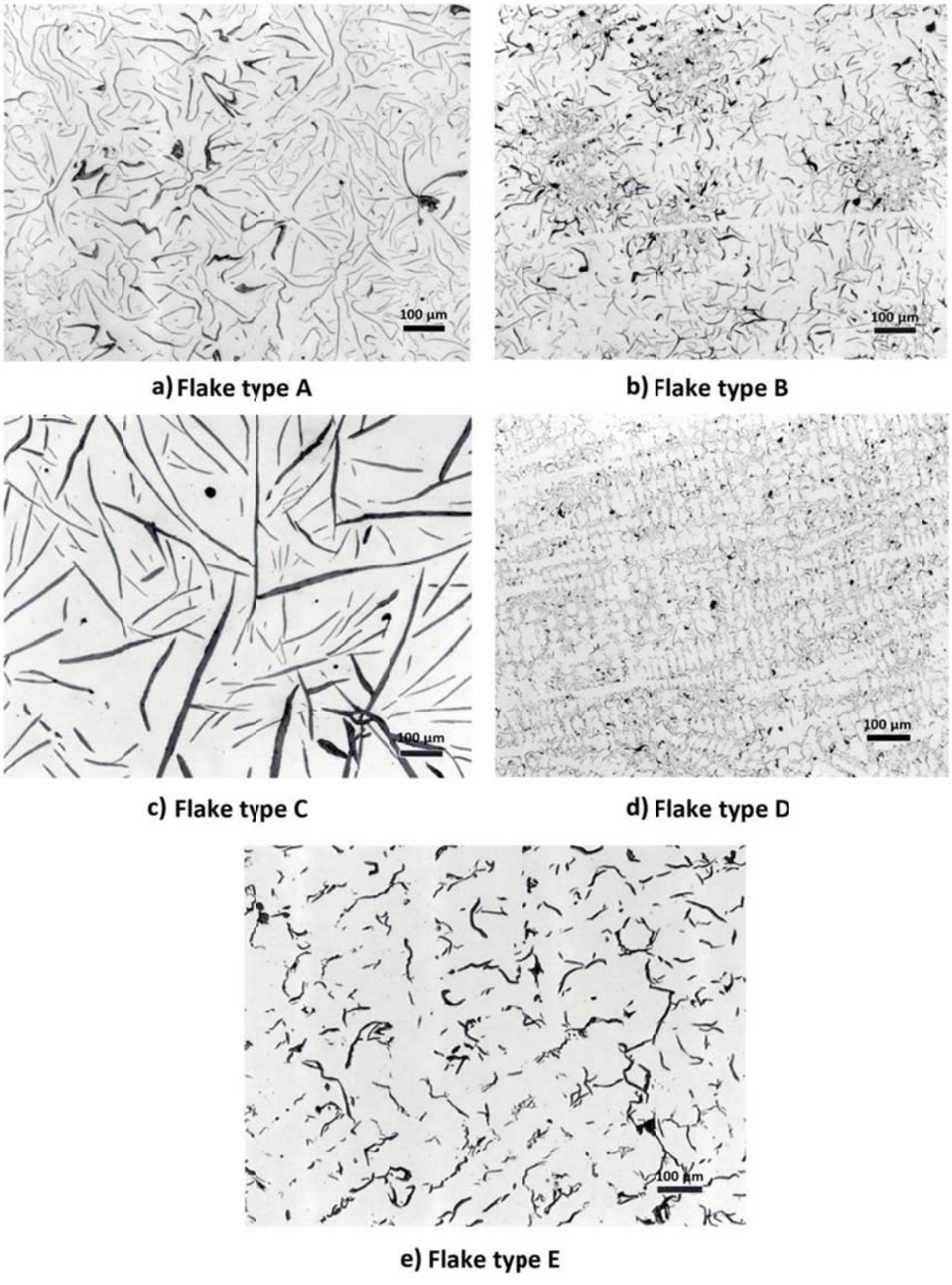

Fig. 5. Different type of graphite flakes [courtesy of Buehler Ltd.]

1.5.1.2.4. Type E flakes

The morphology of type E flakes has been shown in Fig. 5(e). It is observable that Type E flakes possess coarser morphology that type D but a preferred interdendritic distribution. It should be noted that how the plane of polish intersects with the flakes may be responsible for their orientation [8, 25, 26].

1.5.2. Graphite spheres (nodules)

The optical and SEM micrographs of graphite *spheres* (or *nodules*) have been shown in Fig. 6. The cast irons whose graphite morphologies are spherical are generically called *ductile* (*nodular) cast iron.* Compare to gray cast iron, this class has more ductility and better mechanical properties approaching those of steel [30].

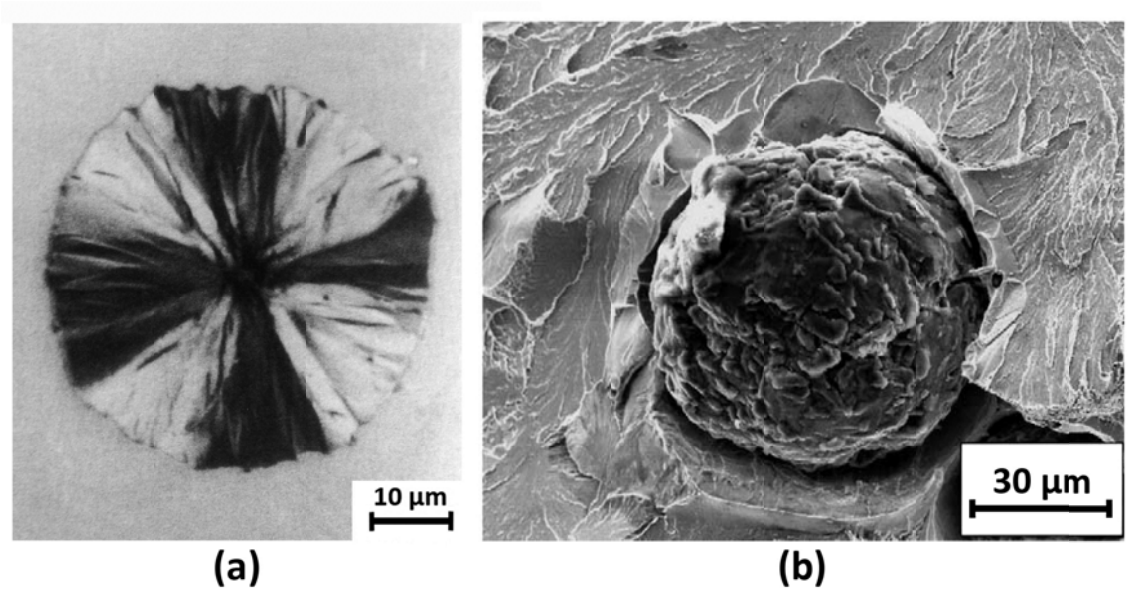

Fig. 6. Graphite spheres micrographs a) optical microscopy [31] b) SEM [32]

The internal structure of graphite spheres will be discussed comprehensively in 1.6.4. However, their growth within the melt will be explained here briefly. During cooling of a ductile iron, graphite spheres and metal dendrites nucleate and grow independently in the melt, a shown schematically in Fig. 7. Initially, the two phases occupy small volume of the melt and move by natural convection without any significant interactions [Fig. 7(a)]. However, as both phases grow, they eventually interact and become interlocked [Fig.

7(b)]. It has been reported that interaction begins when the solid fraction is around 0.3 [33]. As the metallic dendrites grow and expand more, they envelope the graphite spheres and form a microstructure similar to Fig. 7(c) and (d).

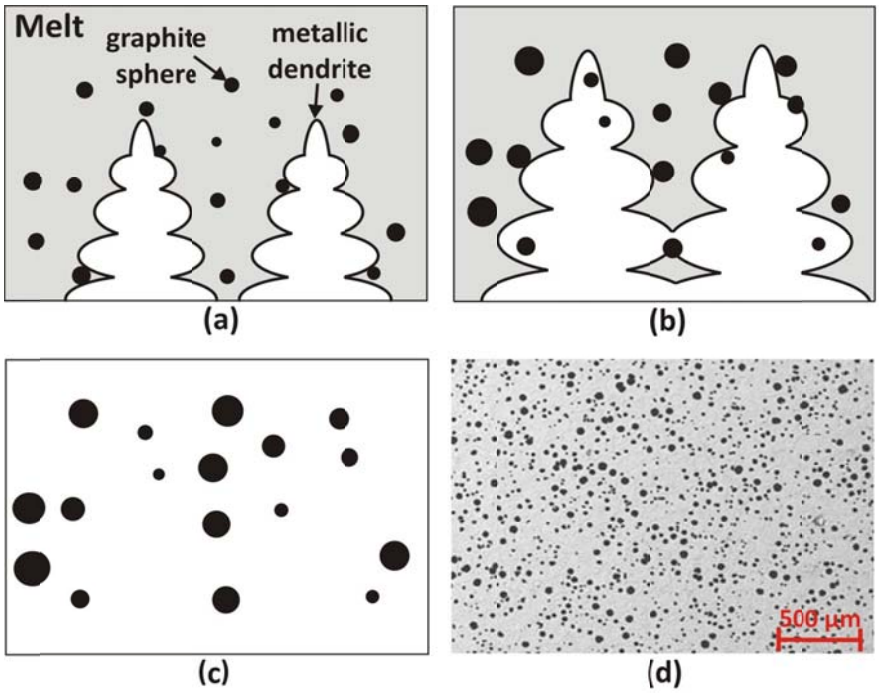

Fig. 7. Solidification of spherical cast iron a) independent growth of metallic dendrites and graphite spheres b) envelopment of graphite spheres by metallic dendrites c) conclusion of solidification d) structure of ductile cast iron [27]

It has been shown that when the melt contains elements such as Mg or Ce the graphite grows in the form of spheres [34-38]. These elements that give rise to formation of graphite spheres are the so-called *nodulizers*. The effect of these elements on the growth mechanisms of graphite spheres will be discussed later in section 1.6.4.

1.5.3. Coral (fibrous) graphite

The coral graphite has a very fine semi-fibrous morphology which is an intermediate form between flake and sphere [39-42]. The optical and SEM micrographs of coral graphite have been shown in Fig. 8(a) and (b). As it is shown in this figure, these fibers are often composed rounded cross sections typically less than one micron in diameter where graphene sheets wrapped around the fiber axis. It is observed that the fibers have branched irregularly and form a highly convoluted and interconnected three-dimensional framework, shown schematically in Fig. 8(c) [43].

The coral morphology normally forms during rapid cooling of iron melt with low sulfur contents (less than 0.001%). However, there is some uncertainty about coral graphite internal structure due to its fine and irregular features.

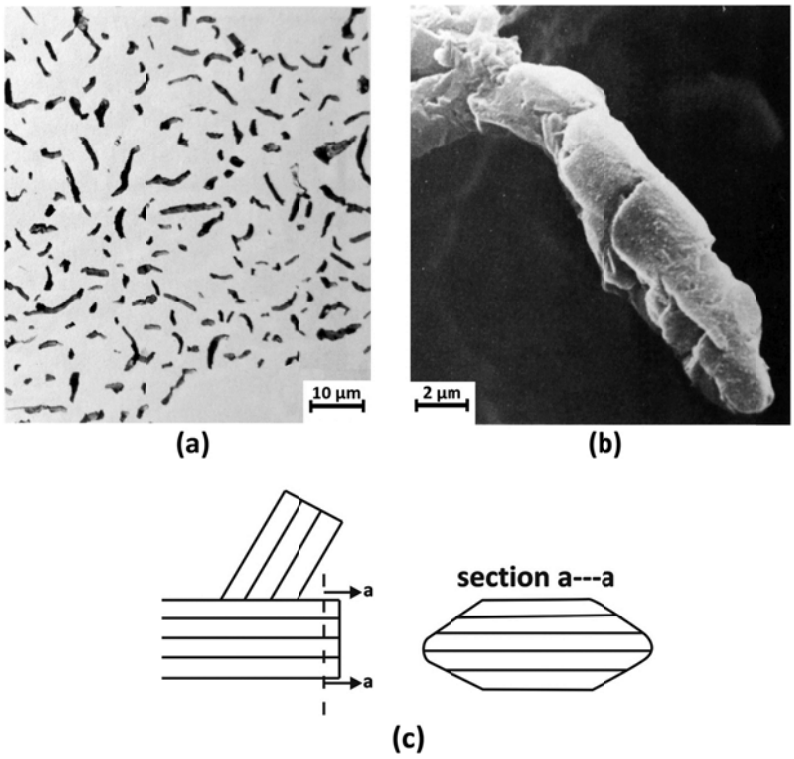

Fig. 8. Coral graphite a) optical micrograph b) SEM micrograph [44] c) schematic of structure [31]

1.5.4. Compacted (vermicular) graphite

The compacted (or vermicular based on the Italian word “worm-like”) graphite also has a morphology between flake and sphere [45]. The optical and SEM micrographs of this morphology have been shown in Fig. 9(a) and (b).

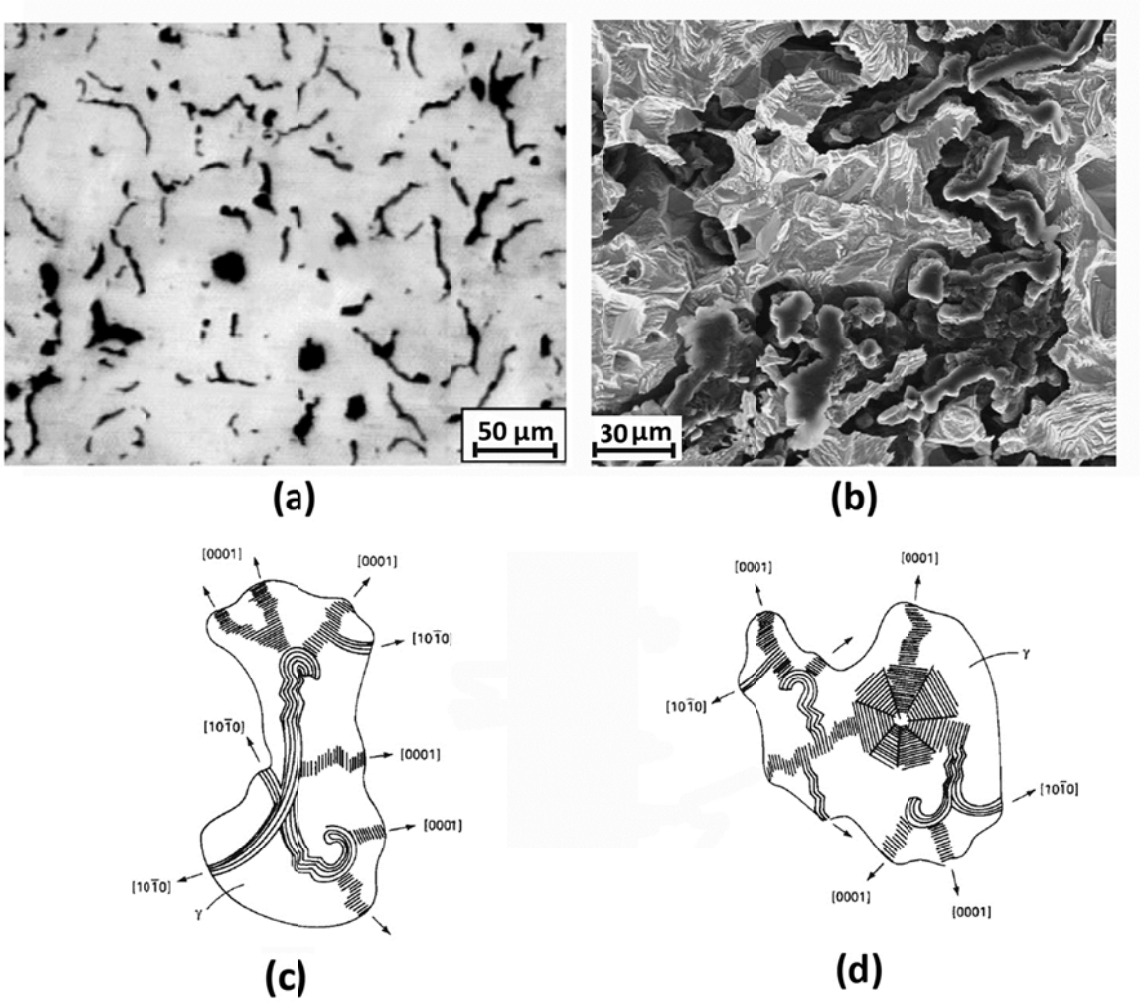

Fig. 9. a) Optical micrograph compacted graphite [46] b) SEM micrograph [47] c) schematic of flake to compacted graphite transition d) schematic of spherical to compacted graphite transition [31]

The compacted graphite has been observed in alloys containing insufficient amount of nodulizers or elements which makes the spherical growth of graphite difficult such as titanium and aluminum [48]. The transformations of spherical/flake to compacted graphite have been shown in Fig. 9(c) and (d).

1.5.5. Degenerate forms of spherical graphite

Some irregular morphologies of spherical graphite may form when the growth of spheres are broken, interrupted or unstable. Below some of these morphologies are explained.

1.5.5.1. Star-like spheres

The morphology and schematic of *star-like* structure has been showed in Fig. 10. The star-like morphology contains graphite pillars which have been extend in the *c* direction irregularly [49]. This structure develops under active nucleation condition, following which the crystal grows rapidly into elongated pillars.

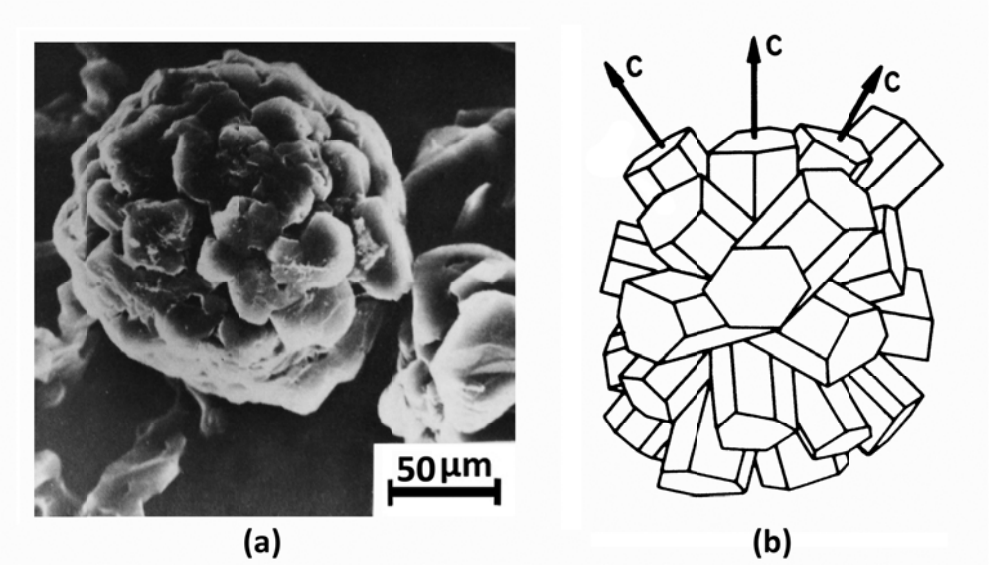

Fig. 10. Star-like structure of graphite a) SEM micrograph b) Irregular growth of budding pillars in *c* direction [49]

1.5.5.2. Exploded spheres

The morphology of *exploded* sphere has been shown in Fig. 11(a) which is similar to broccolis. This form of graphite grows in heavy castings where the spheres will float up into the riser or near the cope surface of the casting. Since these regions have low pressure, Mg will evaporate and cause considerable expansion of spheres. Moreover, the low pressure and lack of mechanical constraint of austenite also aid the spheres to grow freely. These two effects give rise to the formation of an exploded characteristic similar to the one in Fig. 11(b) [50-52].

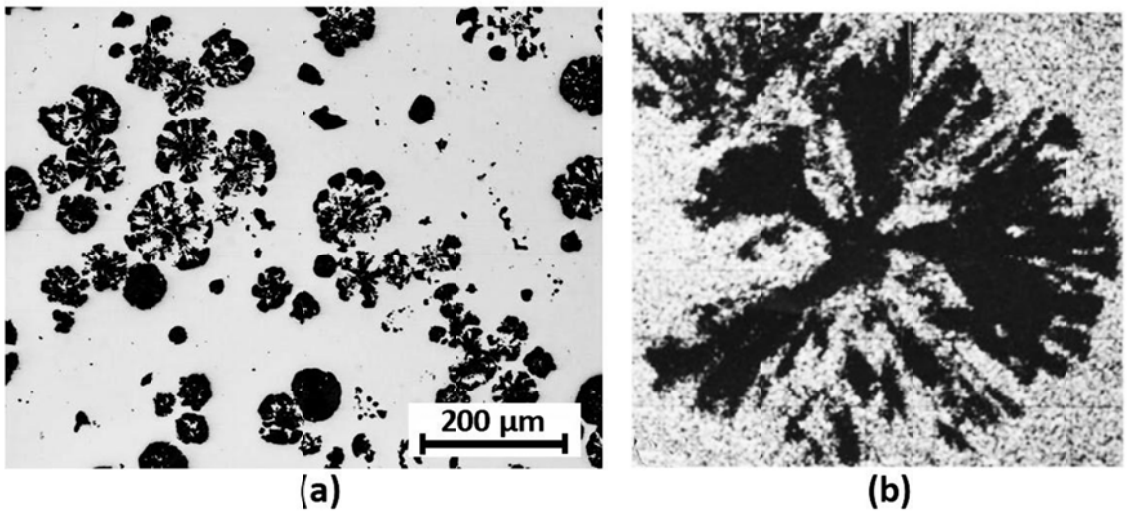

Fig. 11. Exploded nodules [8, 53]

1.5.5.3. Spiky graphite

Graphite spheres which have sharp protrusions are called *spiky* graphite. The morphology of this type of graphite has been shown in Fig. 12. Small amounts of lead, bismuth, titanium and antimony will result in formation of spiky graphite [8].

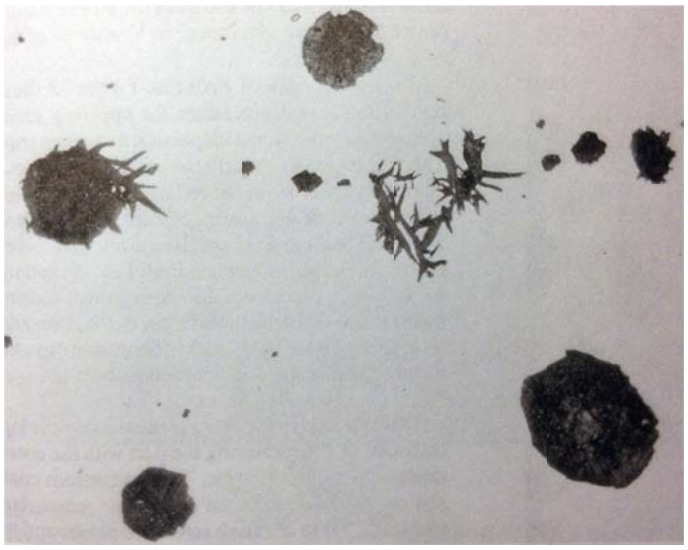

Fig. 12. Spiky graphite morphology [8]

1.6. Graphite growth mechanisms

1.6.1. Liquid-solid interface structures

The structure of a growing interface between the solid and liquid depends on the nature of the interface (thermodynamic) and the amount of growth driving force (kinetics). Normally two extreme cases of interface structures are considered: *non-faceted* (rough, diffuse or continuous) and *Faceted* (smooth, flat or singular) [3]. The structure of non-faceted interface has been shown schematically in Fig. 13(a). It is observed that non-faceted interface is atomically rough and composed of many incomplete atomic layers. During the growth of a non-faceted interface, individual atoms are readily accommodated by closely spaced jogs. The characteristic of this type of interface is this high accommodation factor for arriving atoms and normal grows of interface to itself at all atomic sites. It should be noted that non-faceted interface is thermodynamically in local equilibrium and it will advance by removal of heat or supply of atoms to the interface in the case of pure materials and solutions respectively. This implies that the growth of a non-faceted interface is transport controlled. The faceted interface, on the other hand, is atomically smooth and contains interfacial steps of a few atomic dimensions, the so-called *ledges*. The structure of this interface has been shown schematically in Fig. 13(b). The faceted interface will only grow by provision of atoms into the ledges and their lateral migration. Accordingly advancement of faceted interfaces depends upon constant supply of ledges. The new ledges can be generated by various mechanisms such as, repeated surface 2D nucleation, intersection of a screw dislocation with interface, nucleation at the crystal edges, intersection with other crystals or termination of twins at

the edges [54]. The faceted interfaces appreciably deviate from equilibrium and interfacial kinetics (supercooling or supersaturation) is needed to move them [55, 56].

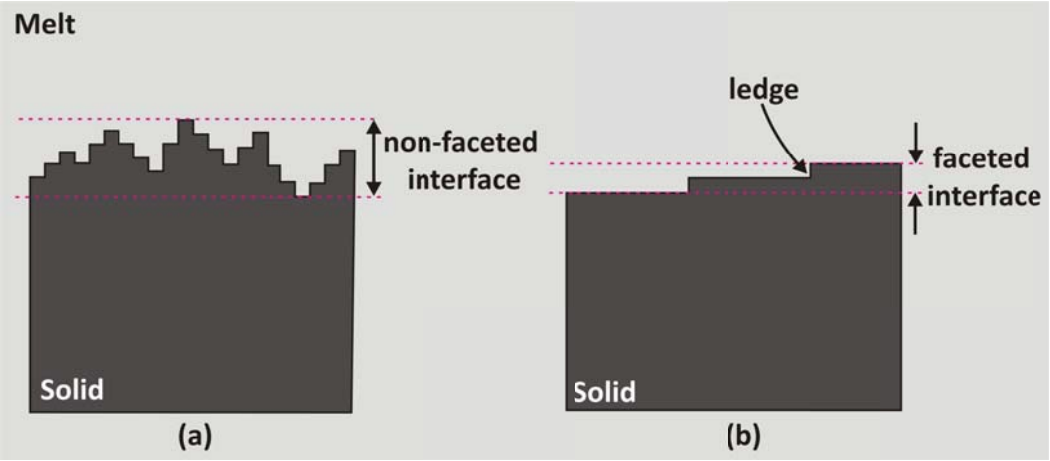

Fig. 13. Atomic structure of a) non-faceted and b) faceted interfaces

It should be noted that although the interface structure is dictated by crystallographic properties, its dynamic structure might show deviations from its static structure, the extents of which depend on the growth driving force or growth speed. It has been shown that at small growth velocities, a naturally smooth interface maintains its faceted structure while at higher growth rates the interface may become *kinetically rough*. As such, a "thermodynamically" smooth interface at small growth rates can become "kinetically" rough at higher growth rates [54-56].

In normal growth condition graphite is bounded by facets planes. However, in non-equilibrium growth condition, graphite interfaces may deviate from these situations.

The characteristic of graphite interfaces during non-equilibrium growth will be discussed comprehensively in section 5.3.1.

To date, different growth mechanisms have been proposed for graphite interfaces which will be described here briefly.

1.6.2. Growth mechanisms of graphite interfaces

Due to different crystallographic characteristic of graphite prismatic and basal planes, different growth mechanisms have been suggested for these families of planes. For instance, it has been shown that graphite prismatic planes are non-faceted in most of growth conditions and their growth is controlled by diffusion of carbon atoms into the interface. On the other hand, graphite basal plane is believed to be faceted, whose growth is controlled by provision of steps created by defects on the surface, i.e. surface controlled. These mechanisms will be discussed bellow.

1.6.2.1. Diffusion controlled growth

Hillert [57] assumed that growth of flake tip (prismatic planes) is controlled by transport of carbon atoms to the interface. He then applied the theory of diffusion controlled growth of a plate tip treated by Zener [58] and found the following equation for growth of graphite prismatic planes:

$$v = \frac{DV_m^{gr}}{2RV_m^L}\frac{x_c^L - x_c^{L/gr}}{x_c^{gr} - x_c^L}$$

Where D is carbon diffusivity in liquid metal, V_m^{gr} and V_m^L are molar volume of graphite and liquid metal, R is tip radius, x_c^L is carbon content of the liquid phase, $x_c^{L/gr}$ is carbon content of the liquid phase with graphite boundary and x_c^{gr} is carbon content of graphite. The equation shows growth rate depends on level of supersaturation ($x_c^L - x_c^{L/gr}$) as well as flake tip radius (R) [10, 58]. This will be discussed in more details in section 5.3.3.1.

1.6.2.2. Defect controlled growth

It has been observed that existence of some defects on graphite interfaces will supply the necessary steps for accommodation of carbon atoms and subsequent growth of interface. For instance, screw dislocations and twisted boundaries are two types of defects which are believed to play dominant role in the growth of graphite basal and prismatic planes respectively [2, 59, 60] and are discussed below.

1.6.2.2.1. Dislocation assisted growth

When the line of a screw dislocation intersects the free surface, a step will be created on the interface. Upon the addition of carbon atoms to this step, it continues to move forward and never disappears [61]. Accordingly, this constant supply of steps will give rise to continues growth of interface at a low level of driving force [11]. This mechanism is the so-called *spiral* or *dislocation assisted growth* and has been shown schematically in Fig. 14. Evidence of spiral growth has been observed for graphite basal plane and shown in Fig. 15.

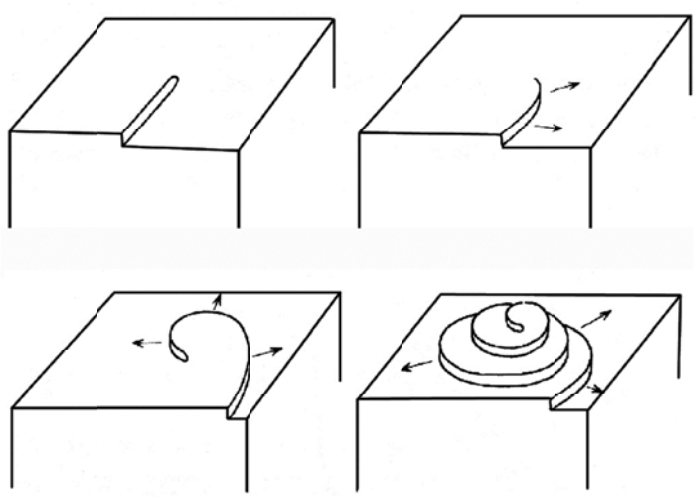

Fig. 14. Dislocation assisted growth mechanism [62]

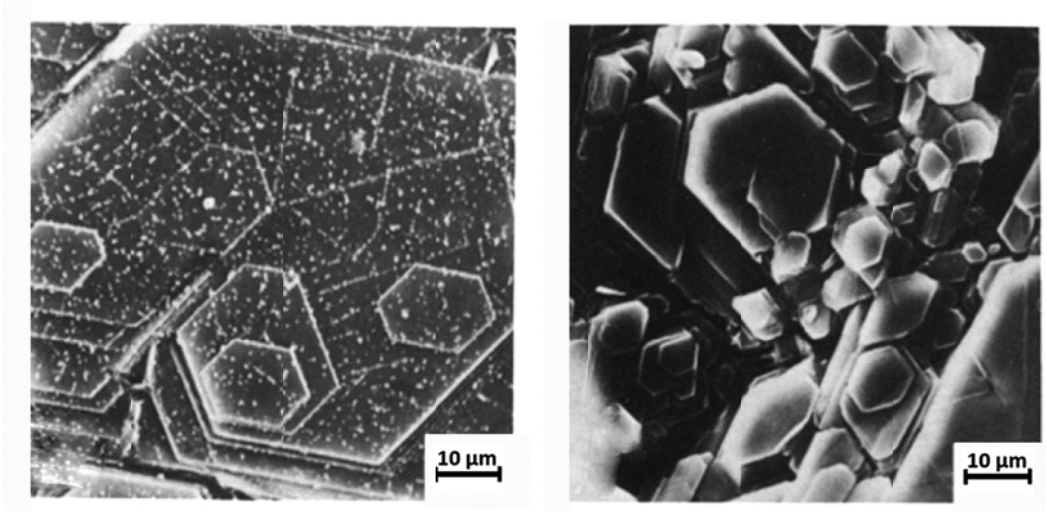

Fig. 15. SEM images of basal planes of graphite grown in liquid nickel [63]

It should be noted that impurities interact strongly with the steps of a screw dislocation and make them immobile in the growing interface. Fig. 16(a) shows the adsorption of impurities on the steps of a screw dislocation schematically. Therefore, small amount of

impurities will adsorb to the steps moving out around a screw dislocation and block the growth. While part of the interface is retarded in growth, the remainder of the crystal will grow over these areas and give rise to formation of holes. Fig. 16(b) shows a formed hole on the basal plane of graphite grown from a nickel melt doped with lanthanum [64]. During the growth of graphite from Ni-C-La liquid, lanthanum atoms form a network on the steps which block growth [65].

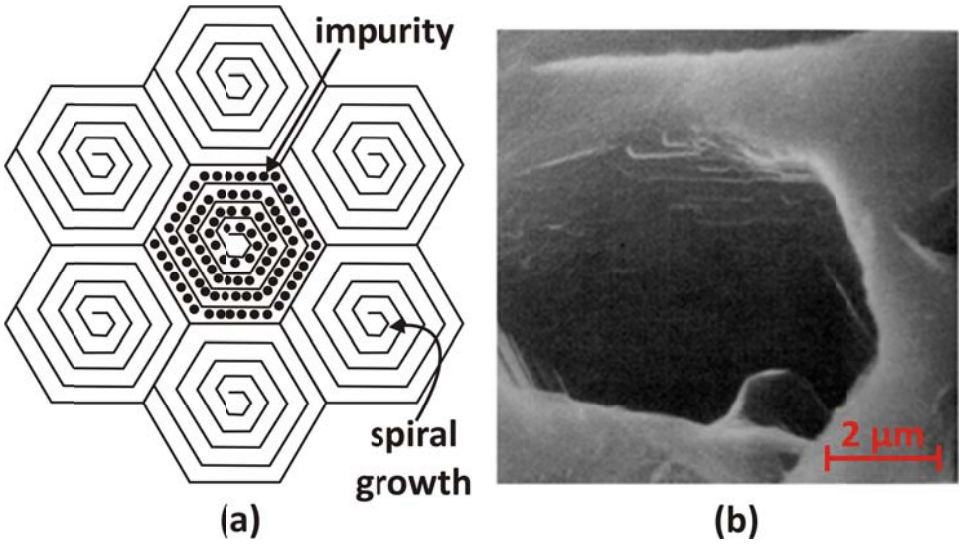

Fig. 16. a) Schematic of impurity adsorption on a screw dislocation steps b) holes in the grown graphite from Ni-C melt containing 0.013 at% lanthanum [64]

It is pertinent to point out that dislocation assisted growth of graphite flakes differ from the growth of spiral cones (section 1.6.4.5) [66]. The configurations of two growth mechanisms have been shown in Fig. 17. Firstly, while the flakes have *c* direction parallel to the dislocation line, in all reported cases of conical growth *c* directions either

lie normal to the cone axis (scrolls) or at some angle of inclination (helical cones). Secondly, the strain energy of spiral cones is greater than the flat arrangement of crystal gown by aids of a dislocation, since for the former the basal planes need to be bent around the cone axis. Finally, the dislocation assisted growth is restricted to regular ABAB graphite basal plane stacking, while the conical arrangements offer other possibilities with higher stacking energies [66, 67]. The conical spiral stacking will be discussed in section 1.6.4.5.

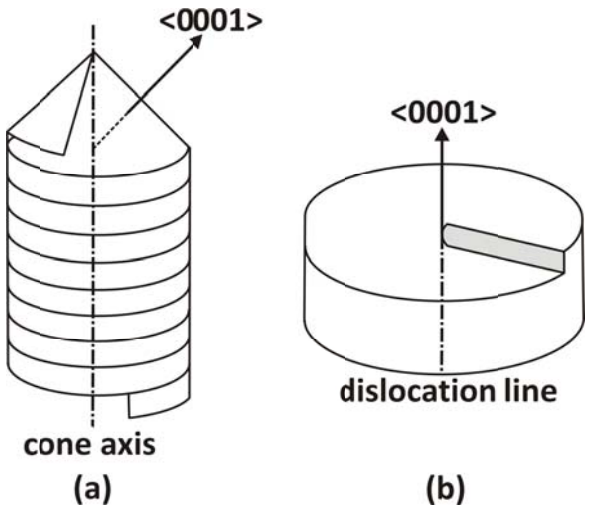

Fig. 17. Two different growth mechanism of graphene sheets a) conical spiral b) dislocation assisted growth

1.6.2.2.2. Growth by means of twist boundaries

The presence of *rotation* or *twist boundaries* in graphite flakes can supply required steps for growth of graphite in prismatic planes. Fig. 18(a) and (b) shows graphite interface without and with the rotation boundary steps. It is observed that the rotation boundary

will provide the necessary sites for attachment of atoms. These steps will aid the growing of the crystal specifically in small supersaturation that the driving force for 2D nucleation is low. An example of rotation boundary in a graphite crystal has been shown in Fig. 18(c). Rotation boundaries were also evidenced by definig the crystallographic directions of graphite dendrites. Fig. 18(d) show a graphite dendrite whose crystallographic direction were determined by X-ray observations using both Laue technique and conical beam camera [68, 69]. Angles between the marked directions implies that the the dendrite is a bicrystal in which the two crystals have rotated by angles of 27.8° about <0001> axis [70]. This rottaion angle is not accidental and in fact it has been reported to be a low energy stacking faults of graphene layers [71].

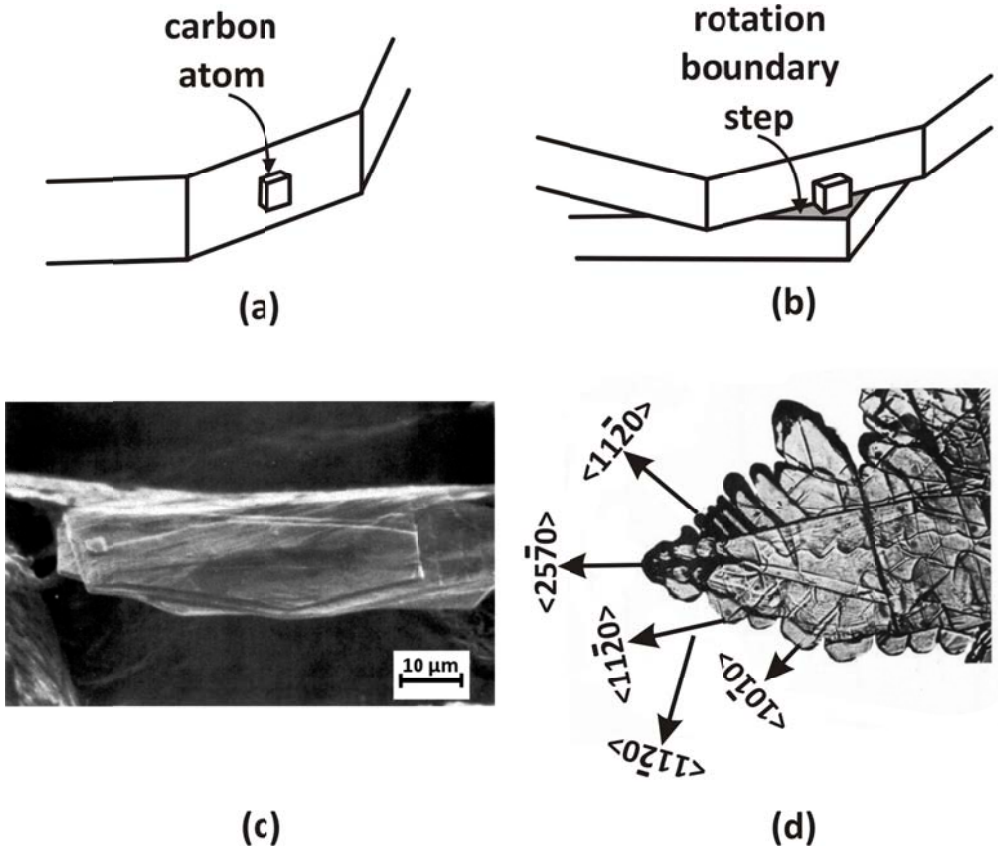

Fig. 18. The graphite growth in the $<10\bar{1}0>$ a) the growth without the rotation boundary steps b) the growth with the rotation boundary steps c) evidence of rotation boundary in a graphite crystal d) an asymetrical graphite dendrites showing the existence of rotation boundary [70, 72]

It is currently believed that the barrier energy for 2D nucleation and growth of defect-free graphite interfaces is too large to occur and the existence of defects for growth of graphite is inevitable [2, 59, 60].

After reviewing general growth mechanisms of graphite interfaces, the growth mechanisms of flakes and spheres as two dominant morphologies of graphite will be described in the following sections.

1.6.3. Growth of flakes

The graphite flakes form since the growth rate of basal plane (*c* direction) is much less than that of prismatic planes (*a* direction). In fact, the higher growth rate of prismatic planes causes the elongation of graphite nucleus in *a* direction and formation of a plate-like morphology, i.e. flakes. However, it is mostly believed that growth of flakes is assisted by impurities. For instance, when the melt contains sulfur and oxygen, these elements may be incorporated into graphene lattice. Since these elements are divalent and can only form two bonds, their addition to graphene lattice will leave saturated. Fig. 19(a) depicts schematic of saturated sites (shown by squares) in a graphene sheet caused by incorporation of sulfur or oxygen into lattice. In spite of the fact that these saturated sites block the growth in those points, the rest of lattice will continue to grow and leaves behind points with one missing bond [Fig. 19(a)]. It should be noted that due to less surface energy of basal plane than that of prismatic planes, the graphene sheets naturally tend to become curved while they grow inside the melt. However, the introduction of these divalent atoms into the carbon network will decrease the surface energy of the prism face and also reduce the graphene sheet bending ability due [73-75]. While the bending of the graphene sheets become less probable by these point defects, nucleation and thickening in the *c* direction continues, as shown schematically in Fig. 19(b). The graphite thickening then reduces the flexibility of graphene dramatically and makes the bending of crystal less possible. As the crystal becomes thicker, it takes the form of a flake and no longer can bend to form other morphologies such as spheres. It should be noted that besides the incorporation of sulfur and oxygen atoms, the rotation boundaries

about *c* axis might also decrease the flexibility of flakes and prevent them from bending (section 1.6.2.2.2). It has been shown by simple calculations that there is more than enough oxygen or sulfur in a typical cast iron to assist the formation of flakes [13].

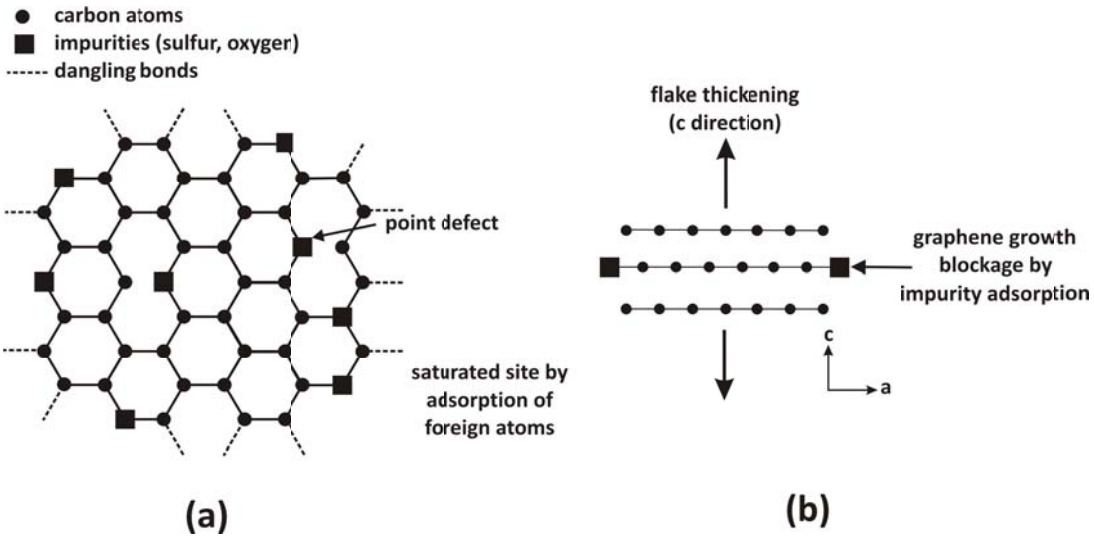

Fig. 19. a) points defects and saturated sites created in the graphene lattice during growth in the *a* direction within a melt doped by oxygen or sulfur b) growth of the flake in the *c* direction [13]

Here some observations which support this model will be described [27, 73, 76-80]. First of all, molten Fe-C-Si alloys were kept in vacuum for a long time (days or weeks) prior to casting to remove the volatile elements of sulfur and oxygen. It was observed that in this situation, the grown morphology of graphite from the liquid is spheres [76]. This is due to the fact that removal of impurities helps the bending of graphene sheets and thus favoring spheres formation. Secondly, Auger analysis shows concentrations of oxygen and sulfur in iron matrix next to flakes [81]. This is on view of the fact that higher amounts of

oxygen and sulfur are available than necessary to cover all the graphite flake surfaces. Moreover, oxygen and sulfur have not been detected at the surfaces of graphite flakes due to limited incorporation of impurities in random sites which are not detectable by Auger analysis [82].

Besides sulfur and oxygen, there are other elements also aiding the flakes formation such as Sb, Pb, Al, Bi and Ti [83-86]. All of these impurities which aid the flake formation are called *subversive impurities* and their effect increases with their atomic weight and concentration.

Based on the proposed model, graphite flakes are a modified shape growing by aid of impurities. In fact, graphite spheres are natural grown morphology of graphite within a pure melt and discussed in the next section.

1.6.4. Growth of spheres

The initial models for growth of spherical graphite proposed that spheres were growing in solid state within an austenite shell by decomposition of cementite [87-91] or by carbon depletion of a supersaturated austenite [92-94]. Although, these mechanisms may contribute to the growth of spherical graphite, later observations including quenching of partially solidified melt [95, 96], graphite flotation [97-99], graphite segregation during centrifuging [96, 99, 100] and records of volume temperature curve [101] have shown that spheres grow directly from the melt. Moreover, investigation of graphite spheres grown from a melt containing cerium showed that while the cerium existed in spheres

structure, it was not detected in metallic austenite [34-38, 99]. Since the solubility of cerium in solid austenite is very low, it is almost impossible for cerium to diffuse through the solid shell. Therefore, this provides another evidence for direct growth of graphite spheres from the melt.

As it was described in section 1.6.3, incorporation of subversive elements reduces the bending ability of graphene sheets and promotes the formation of flakes. However, addition of nodulizers such as Mg or Ce will scavenge the sulfur and oxygen as oxides and sulfides (e.g. MgO and MgS) and favors the formation of graphite spheres.

Although it is observed that sphere grow from the melt until it is enveloped by a metallic shell, growth after the envelopment may continue by solid-state diffusion of carbon through solid shell [102, 103]. Radius measurements of graphite spheres and austenite shell, however, have shown that most of spheres mainly grow in direct contact with the melt [100, 103, 104].

Several models have been proposed for growth of spheres and its structure which will be described below. However, to date there is not unanimity on growth mechanism of spherical graphite.

1.6.4.1. Screw dislocations model

According to this model [105], the foreign atoms of Ce or Mg are adsorbed into growing steps of graphite and causes the generation of screw dislocations. After some spiral growth, since they would not fit together, they divide into new branches and lead to the

formation of graphite spheres, as shown schematically in Fig. 20. It has been indicated that although the screw dislocation plays an important role in growth, it is not necessary to postulate their creation by impurities [2].

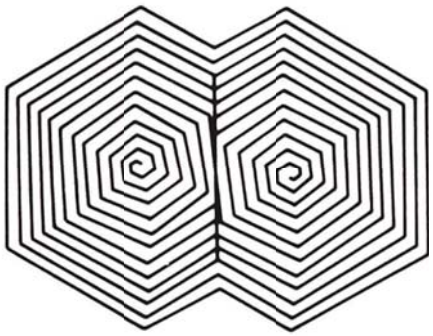

Fig. 20. Growth of spherical graphite from screw dislocations [105]

1.6.4.2. Growth by branching of an acicular crystal

Based on this model by Shubnicov [106], an acicular crystal of graphite initially forms and then steadily branches and causes a spherical form. Different geometries are possible depending on the relationships between growth and branching rates. For a normal crystal which grows in a preferential crystallographic direction and branched repeatedly, two symmetrical exposed cavities can form, as shown schematically in Fig. 21(a) and (b). Shubnicov definition was, however, not correct due to incorrect orientation of (0001) plane. A possible correction by Minkoff [107] suggested that (0001) planes align radially as determined by the relative growth rates normal and in the (0001) plane [Fig. 21(c)].

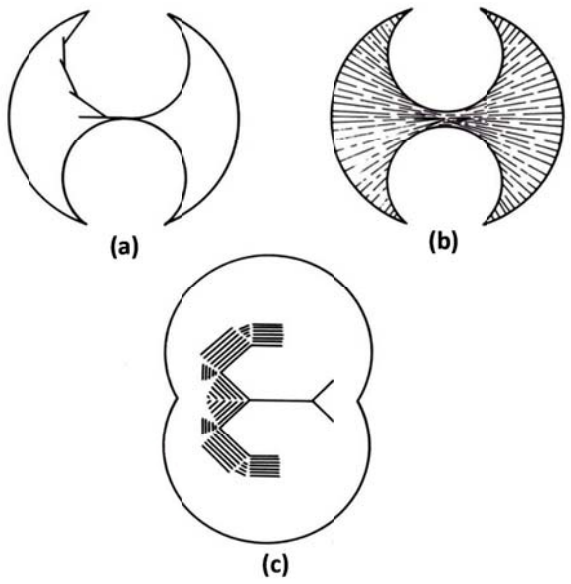

Fig. 21. a) growth of spherical graphite by branching of an acicular crystal b) Shubnicov idealization of graphite spheres by a branching mechanism [106] c) Minkoff suggestion of spherical growth by branching of graphite platelet [107]

1.6.4.3. Interface breakdown model

It was observed in transparent glycerol-water solutions that the spheres are initiated through nucleation of an acicular aggregate in which crystal filaments (*cellular dendrites*) grow outwards radially [108-110]. In the early stage of the growth, the filaments are separated from each other by the melt and later, as the filaments thicken and branch, the interdendritic spaces are occupied. The same model was also proposed for graphite crystals [111], according to which a polyhedral crystal initially grow with stable faceted interfaces, as shown in schematic of Fig. 22. Once a critical size is reached the growth begins to become unstable and interfaces breakdown. Due to faster growth rates of

corners, protuberances lag behind the corners by a distance Ɛ. However, as growth proceeds, the crystal gets the form of an sphere.

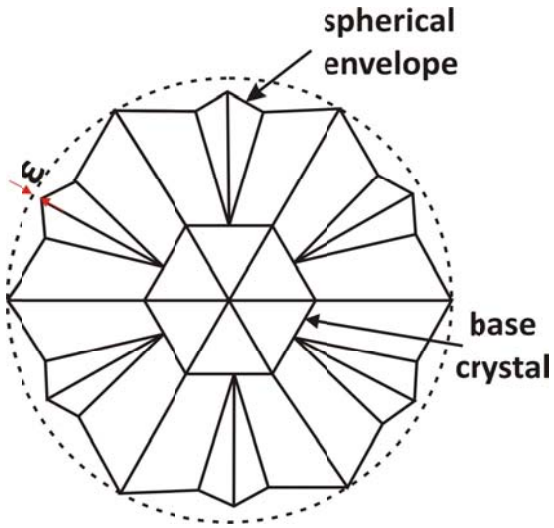

Fig. 22. Growth of a sphere by interface breakdown [2]

1.6.4.4. Circumferential growth model

This model is based on the ability of graphene sheets to become curved as they grow inside pure metals. According to this model [76] the graphite spherical shape results from the growth of curved crystals in *a* direction producing in a pattern similar to cabbage leaves. The morphology of a sphere proposed to be grown under this mechanism along with schematic of growth has been shown in Fig. 23. While growing curved crystals run into each other, boundaries are formed on the surface which later new steps can develop from them. It should be noted that growth of spheres through this mechanism is energetically favorable since low energy basal plane of graphite is always exposed to the melt.

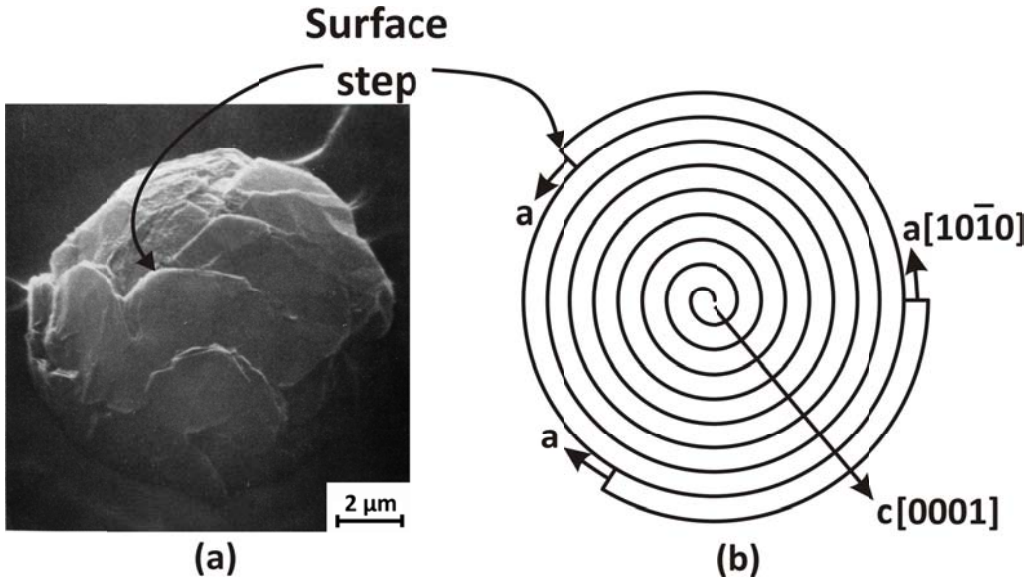

Fig. 23. Circumferential growth of graphite spheres a) Surface of a spheres showing cabbage leaves growth patter b) Diametric section showing growth of curved crystals in *a* direction [76]

1.6.4.5. Growth by spiral cones

Based on this model [66], a graphite sphere is formed by growth of spiral cones. Upon graphite nucleation, graphitic cones grow on the nucleus in 3D space while their basal planes are in contact with the melt. The formation of spheres by growth of spiral cones has been shown schematically in Fig. 24.

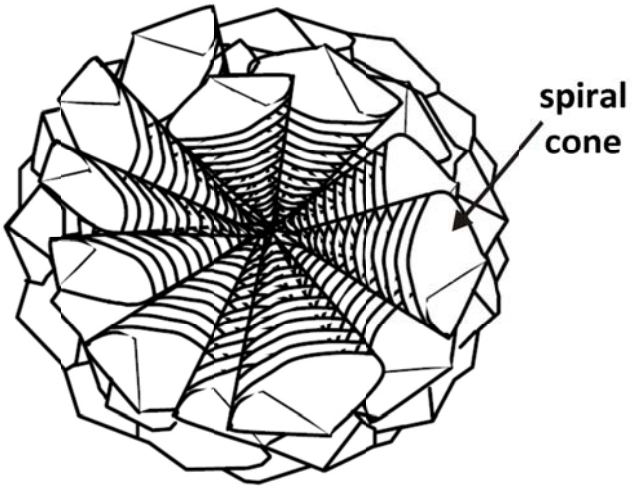

Fig. 24. Sphere formation by growth of spiral cones [112]

It should be noted that spiral cones may be formed by twisting of a radially cut graphene sheet. An individual filament is then composed of numerous interconnected graphite basal planes stacked and rotated on top of each other by a relative rotation angle of θ. The apex of the cone is also defined by the extent of the overlap and has the relationship of $\theta=2\pi\text{Cos}(\alpha/2)$ with relative rotation angle. The geometry of a spiral cone along with its relative rotation and apex angles has been shown in Fig. 25.

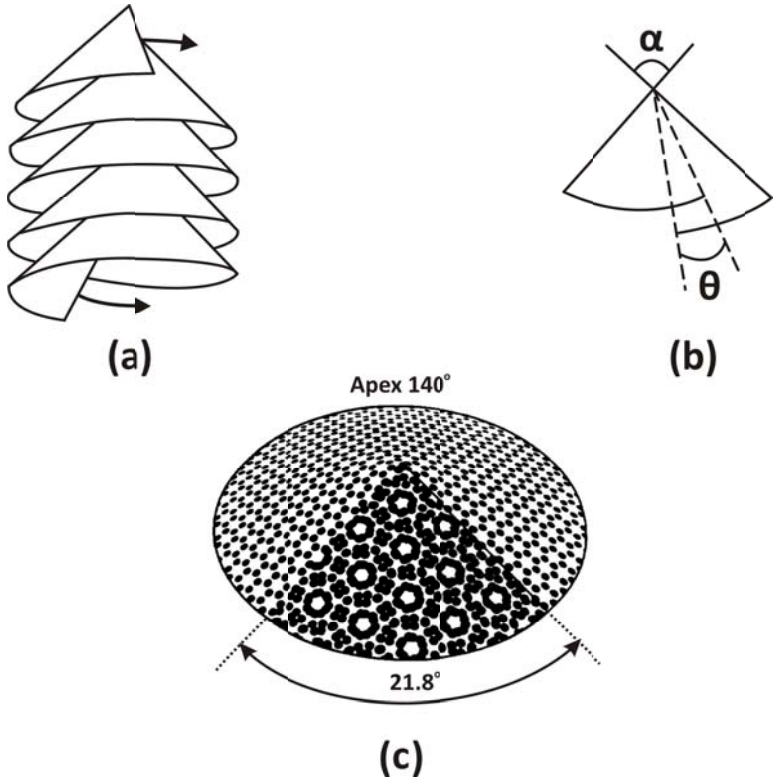

Fig. 25. Geometry of a spiral cone a) formation by twisting of graphene sheets b) apex and relative rotation angles c) formation of a spiral cone from a graphene sheet [66]

The possible cones apex angle are between 0° and 180° where α=180° is for growth around a pure screw dislocation and α=0° forms a cylindrical scroll terminating in a step of purely edge character. In between these two values (0° and 180°) there is a range of spiral cones where the steps have mixed screw and edge character. In series of experiments, it was observed that apex angle of the whisker was 140° [113], as shown schematically in Fig. 25(c). Relationship between the relative rotation angle and the apex angle shows that the rotation angle θ in this case is 21.8°, which represents one of the lowest energy stacking faults of graphite around *c* axis [71]. This implies that spiral cones possess perfect coincidence in between their layers to minimize their stacking energy. It

is also pertinent to point out that the configurations of $\theta = 60n$ are highly preferred since in these cases, each turn of the cone will bring the graphene layers back into exact coincidence.

Structurally any cross-section of the spiral cones has a different pattern depending on the cutting angles. However, the cross sections are normally irregular and appear to be curved or arranged in complex "herring-bone" patterns, as shown in thermally etched section of graphite spheres in Fig. 26. The micrographs show that the general section possesses a concentric pattern [Fig. 26(a)] while the diametral section has a ribbed structure leading to chevron morphology [Fig. 26(b)]. The schematic of this chevron morphology has also been shown in Fig. 27. It is also observable in Fig. 26(b) that the center of sphere is composed of branched flakes morphology.

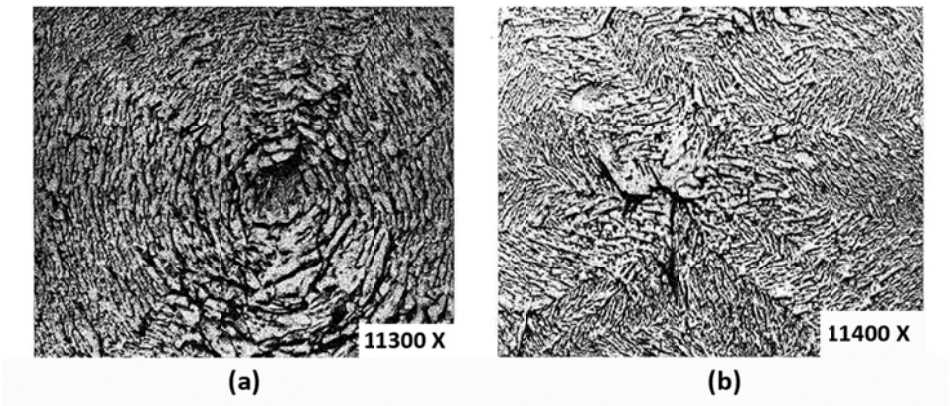

Fig. 26. Sections of graphite spheres a) general b) diametral [114]

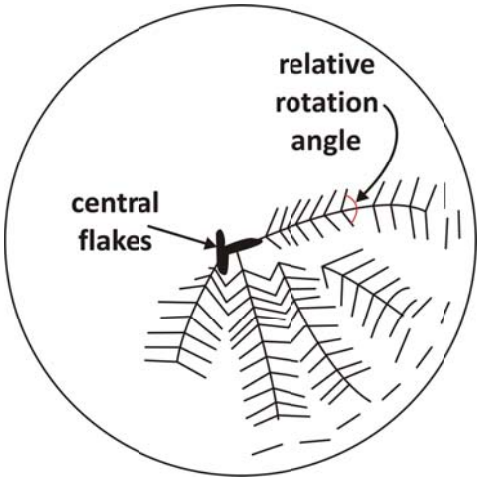

Fig. 27. Schematic features of diametral section of graphite spheres [115]

1.6.4.6. Maltese cross pattern growth model

Based on this model [116], a graphite sphere is formed by dislocation assisted growth of filaments in the c direction within the liquid, as shown schematically in Fig. 28. The model proposed that the structure of cut spheres will be similar to a Maltese cross pattern. The necessary high density of dislocations for sphere growth by this model is believed to be generated by stress induction due to incorporation of foreign atoms in the graphite lattice [116]. This model can be regarded as a special case of growth by conical spirals where the apex angle is 180°.

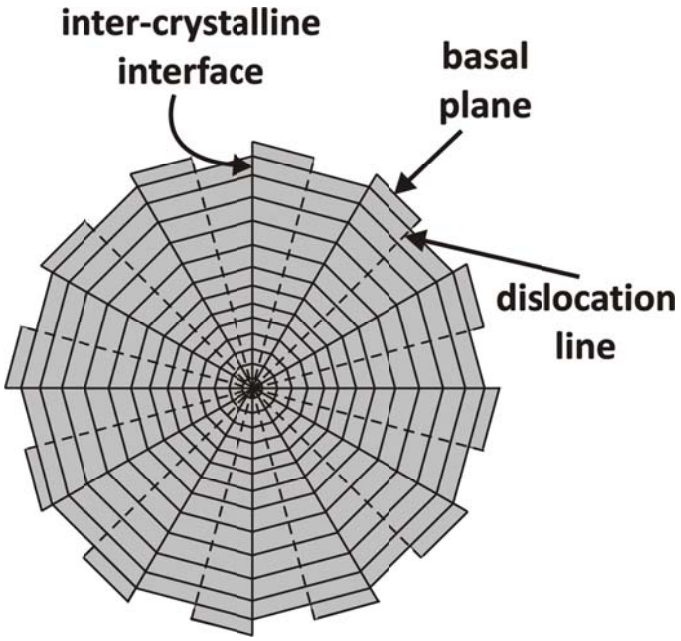

Fig. 28. Formation of spherical graphite by dislocation assisted growth of filaments [116]

1.6.4.7. Growth through the solid shell

As it was explained in section 1.5.2, graphite spheres which initially grow inside the melt are eventually surrounded by metallic solid shells. Based on this model [102, 103, 117-119], graphite spheres could then continue to grow by diffusion of carbon atoms through metallic shell. It has been reported that the formation of metallic shell occurs when the spheres has reached a certain size (e.g. 10 μm in [103]). It is also believed that the necessary space for growth of spheres within the metallic shell is provided by plastic deformation of shell under growing pressure of graphite at growth temperatures [120].

1.6.5. Growth of flakes vs. spheres

Series of directional solidification experiments showed that the growth morphologies of eutectic graphite depend on the amount of nodulizers as well as ratio of thermal gradient to growth rate (G/V) [121-124]. Fig. 29 shows the graphite morphology as a function of G/V ratio and amount of nodulizer (Ce).

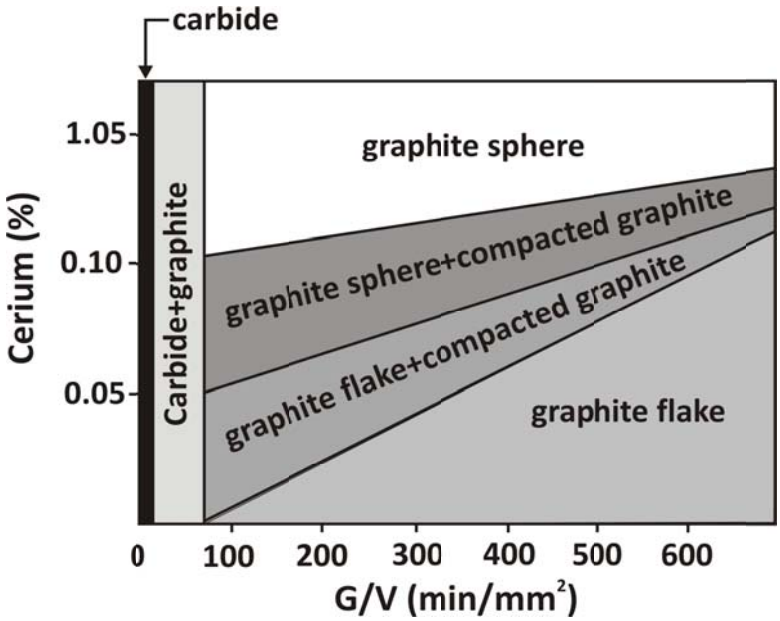

Fig. 29. Effect of G/V ratio and amount of nodulizer on graphite morphology [122]

As can be seen in Fig. 29, at high cooling rates, regardless of the nodulizer amount, the resulted phase is carbide. However, with decreasing cooling rate the *mottled iron* (mixture of white and gray cast iron) will form. With addition of cerium, the transition from flakes to compacted and from compacted to spherical graphite will occur. In spite of chemical treatment with nodulizers, high cooling rates also promote the spheres formation. In fact, in systems of Ni-C, Fe-C-Si, Fe-C and Co-C morphology change from

flake to sphere has been observed by cooling rate increase and even without addition of nodulizers [99, 115, 125-127]. Furthermore, in systems which possess inadequate amount of nodulizers or weak nodulizers, higher cooling rates will promote the formation of graphite spheres [128-131]. For instance, in directionally solidified Ni-C alloys the transition from flakes to sphere occurs when the growth rate is 25 cm/h [125] or 44 cm/h [126]. Fig. 30 shows the microstructure of two cast irons which have been solidified directionally with different growth rates. It is observed that by growth rate increase the morphology will alter from flake to sphere. The characteristic of this morphology change is not fully understood yet. With further increase of cooling rates, however, a graphite to carbide transition may occur which will be explained next.

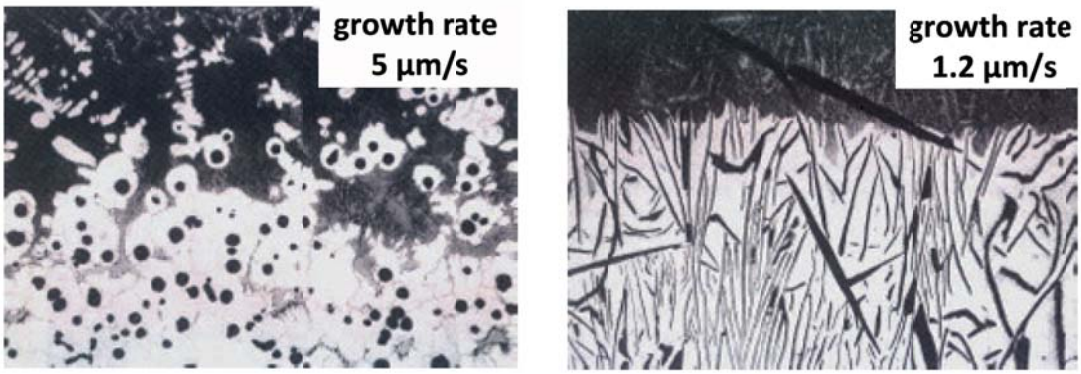

Fig. 30. Graphite morphology change from flakes to spheres with growth rate increase [124]

1.6.6. Graphite to carbide transition

As it was explained in section 1.2 in some of metal-carbon systems there are possibility of both stable graphite and metal stable carbide formation. For instance, in Fe-C system, it has been observed that formation of graphite or carbide mostly depends on the cooling rates, i.e. in high cooling rates the carbide will form while in slower cooling rates the graphite will grow [57, 132]. Therefore, there is a critical cooling rate range below which the graphite will grow (gray structure) and higher than that the carbide forms (white structure). Inside this range a mixture of carbide and graphite will form (mottled structure). These transitions were already shown in graph of Fig. 29.

In order to explain the formation of carbides in higher cooling rates, Hillert [22] calculated the critical thickness of graphite and cementite 2D nuclei as well as growth rate of two phases as functions of undercooling. For this purpose, he used the concept of a disk-shaped 2D nucleus for calculation of nucleus critical thickness (h^*) and also the Zener diffusion controlled growth of a plate for growth of graphite and cementite plate tips [58]. Fig. 31 shows the critical thickness (h^*) of graphite and cementite 2D nuclei as well as growth rate (v_{max}) of the two phase within a eutectic melt functions of undercooling.

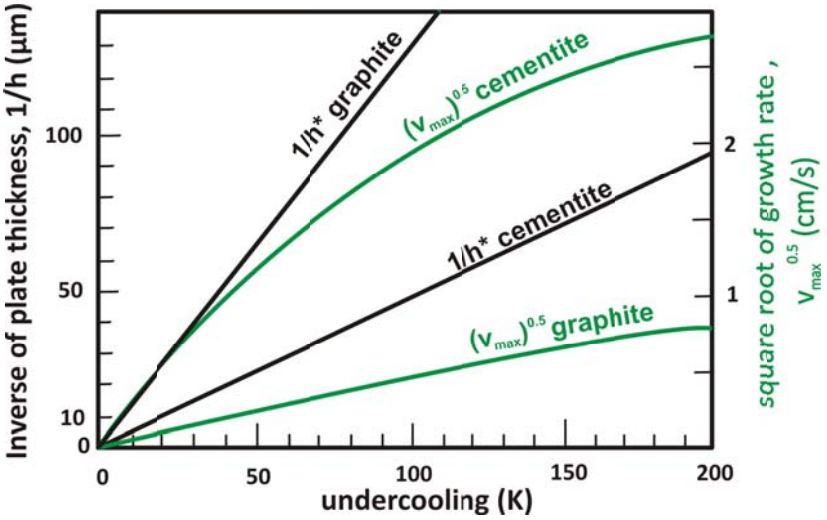

Fig. 31. Critical thickness of graphite and cementite 2D nuclei (h*) as well as growth rate of the two (v_{max}) as a function of undercooling within a eutectic melt [57]

The calculations showed that h^* of graphite is smaller in all temperatures and accordingly graphite nucleates more easily than cementite. On the other hand, based on the calculated values of cementite and graphite growth rates, upon nucleation of both phases the cementite is the one which grows faster. In this matter, the competition between graphite and cementite formation could be explained kinetically as follows. In small cooling rates, graphite nuclei start to form due to less nucleation barrier energy. The solidification will then proceed mostly by formation of graphite crystals (gray structure). Nevertheless, in higher cooling rates and amount of undercooling, due to reduction of nucleus critical thickness (h^*) more cementite nuclei will form. The formed cementite crystals will then grow rapidly in the melt due to their higher growth rates, leading to formation of white structure. It is pertinent to point out that higher growth rate of cementite is due to the fact

that for its formation, there is no need for long range diffusion of carbon and its lattice is more similar to melt structure [12].

As it was shown in Fig. 29, increasing the cooling rate (undercooling) gives rise to graphite morphology changes. In the following section, the effect of undercooling on growth velocities of graphite will be discussed.

1.7. Kinetics of graphite growth

The growth velocities of graphite in prismatic and basal planes can be described by growth driving force (thermodynamics) and growth mechanism (kinetics). The driving force is the amount of undercooling (ΔT) or supersaturation (ΔC) which is controlled by experimental parameters. However, the growth rate or interface mobility is the characteristic of the material and depends on the crystal growth mechanism which is active on the interface. Fig. 32 compares the growth rates of austenite and prismatic face of graphite as well as dislocation assisted growth rate of basal plane [86, 132, 133].

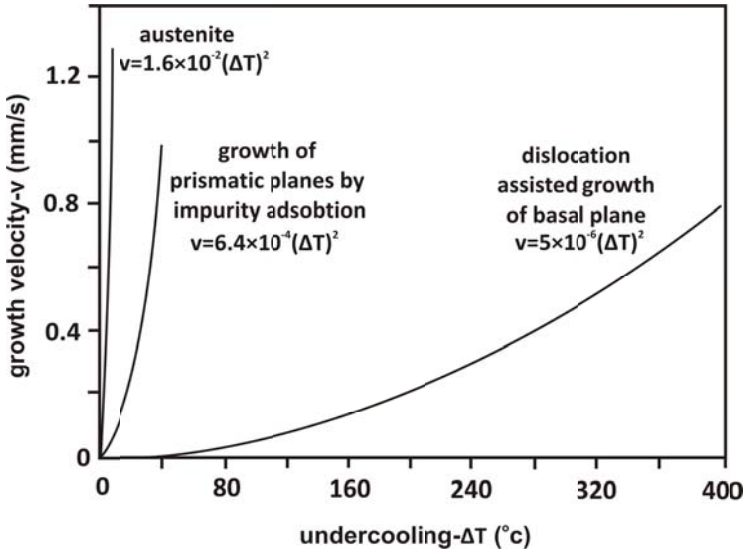

Fig. 32. Growth rates of austenite and graphite prismatic planes as well as dislocation assisted growth rate of basal plane [133]

Fig. 32 shows growth of prismatic planes is orders of magnitude higher than the dislocation assisted growth rate of basal plane. As it was mentioned in section 1.5.1, the higher lengthening rates of graphite in its prismatic plane than that of thickening rates in basal plane of graphite will give rise to the formation of flake morphology. Fig. 32 also shows that the growth rate of graphite planes is orders of magnitude smaller than the austenite which justifies the presence of weekly coupled eutectic between graphite and austenite. Moreover, the spiral growth rate in basal plane is orders of magnitude smaller than austenite. Assuming the Maltese pattern growth of spheres, the growth of graphite in basal plane then lags behind the growth of austenite. This will lead to formation of completely decoupled eutectic of austenite and spherical graphite. The graph also shows that growth of graphite spheres need larger driving force than flakes. It has been observed

that the eutectic graphite flakes can grow in undercooling as small as 1K while the necessary undercooling for sphere growth is at least 10K [115].

Adding impurities to the melt will, however, change the growth kinetics. Impurities can be categorized into three groups [70, 134] 1) reactive element: such as rare earth elements which have strong reaction with graphite; 2) solutes: such as silicon and boron which have no chemical reaction with graphite and 3) weakly reactive element: like sulfur and oxygen which are adsorbed weakly and change the edge energies. Fig. 33 shows the qualitative relationship of undercooling and growth rates for basal and prismatic planes of graphite within pure melt and ,as an example, the melt containing weakly reactive elements [70]. Both prismatic growth curves of Fig. 33(a) are in the forms of $R=exp(-\Delta Q/RT)$ Where ΔQ is the free energy of nucleation for one mole of crystal layer on prismatic face, T is the absolute temperature and R is the gas constants. ΔQ is a function of mechanism of formation and the environment. It is also observed that growth of prismatic planes by means of rotation boundary is to the left of growth curve without rotation boundary. This is owing to the fact that interfaces with rotation boundaries possess less nucleation barrier energy and higher growth rates.

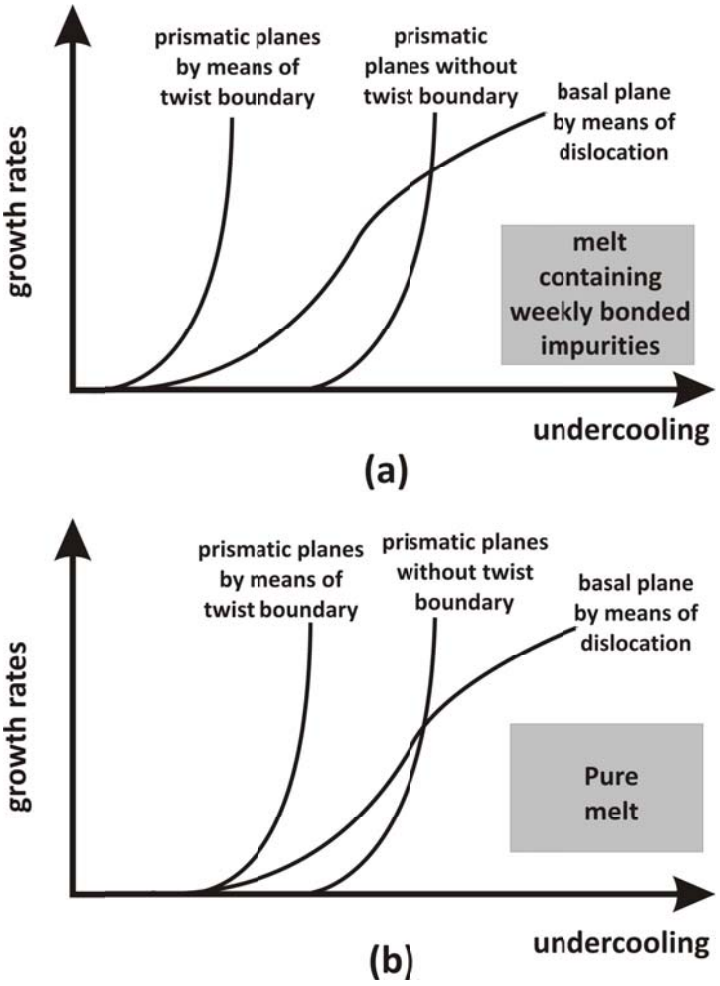

Fig. 33. undercooling vs. growth rate of graphite basal and prismatic planes from experimental observation [70]

Comparing growth rates of prismatic planes in Fig. 33(a) and (b) reveals that weakly adsorbing impurities like sulfur reduce the necessary undercooling needed for a specific growth rate. This is due to the fact that small concentration of these impurities will lower the edge energy of the prismatic planes and will also lower the free energy of nucleation at the step of a rotation boundary.

It is pertinent to point out that in high driving force (undercooling) a gradual change from anisotropic growth (different growth rate in prismatic and basal plane) to nearly isotropic growth (same growth rates in all direction) will occur. Since there is always possibility of carbide formation in high undercoolings, achieving such a large driving force upon cooling seems impossible. However, doping the melt with silicon will increase the activity of carbon and the driving force for graphite growth. Fig. 34 shows the dendritic morphology of graphite in silicon-riched region of iron melt. The formation of dendrites in high silicon content melt implies the isotropic growth of graphite in high driving force.

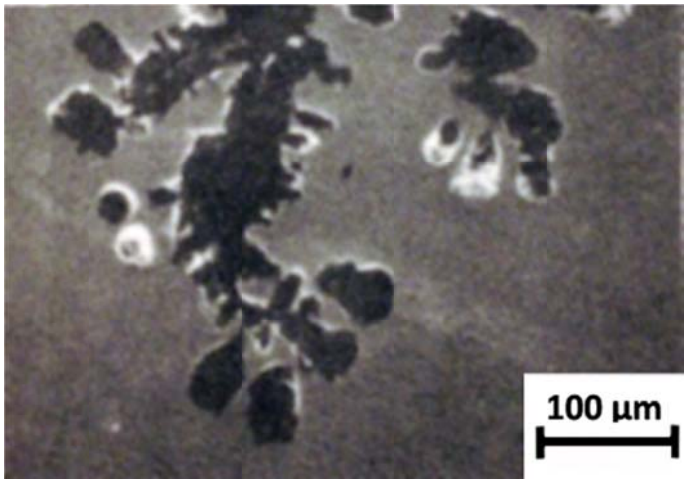

Fig. 34. Dendritic morphology of graphite in silicon-riched region of iron [133]

1.8. Instability of graphite interfaces during growth

The prismatic faces of graphite show some instability during growth due to higher growth rates and presence of faults. Some of these instabilities including side branching of dendrite arms and branching of eutectic flakes have been shown in Fig. 35. It is believed that these instabilities occur on steps of a rotation boundary [70].

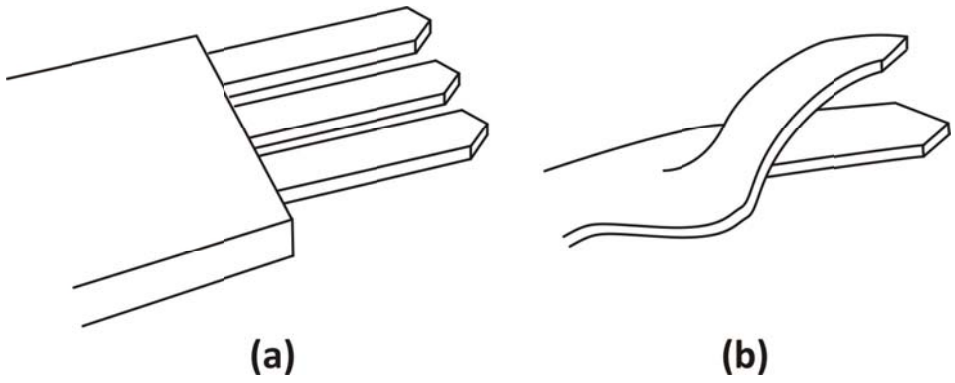

Fig. 35. Growth Instabilities of graphite interfaces a) side branching of dendrite arms b) branching of eutectic flakes [70]

Fig. 36 shows SEM photos of eutectic graphite flakes which frequently branched in the plane of the sheets. The branching is in a way that leaves of graphite growing out of the original lath.

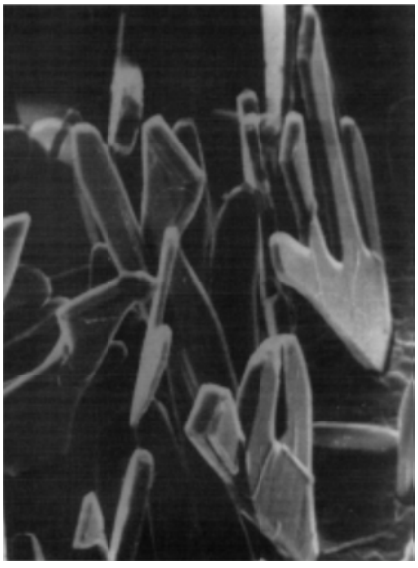

Fig. 36. Scanning electron micrograph of eutectic flakes grown within Ni-C melt [135]

In large driving force other type of instabilities may occur which have been shown schematically in Fig. 37. The instability occurs by a fault of low angle boundary or twin character and is the one discussed for growth of spheres by branching of an acicular crystal (section 1.6.4.2) [70, 106].

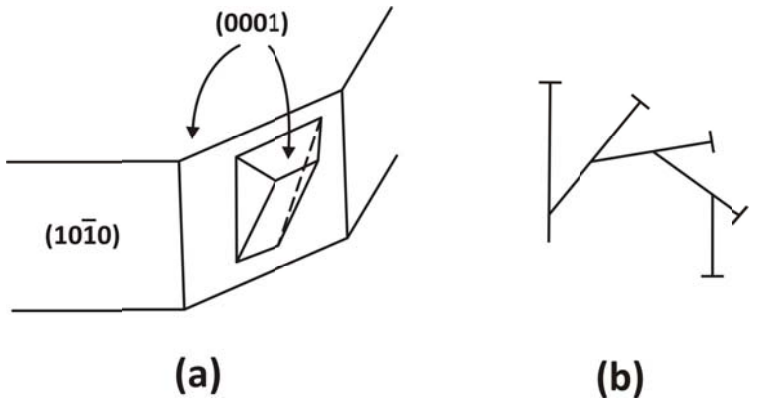

Fig. 37. instabilities in prismatic face under large driving force a) fault of low angle boundary or twin character b) repeated instability forming spheres [70, 106]

Another type of Instability which may occur during the growth of graphite is caused by solutes which have no interaction with graphite such as silicon and boron. These elements may concentrate in the boundary layer of the growing crystal and cause formation of ridges in graphite interfaces, as shown in Fig. 38. It has been observed that due to formation of a boron rich solute, the steps on the growing face became unstable and traversed the surface as elongated ridges [70, 136].

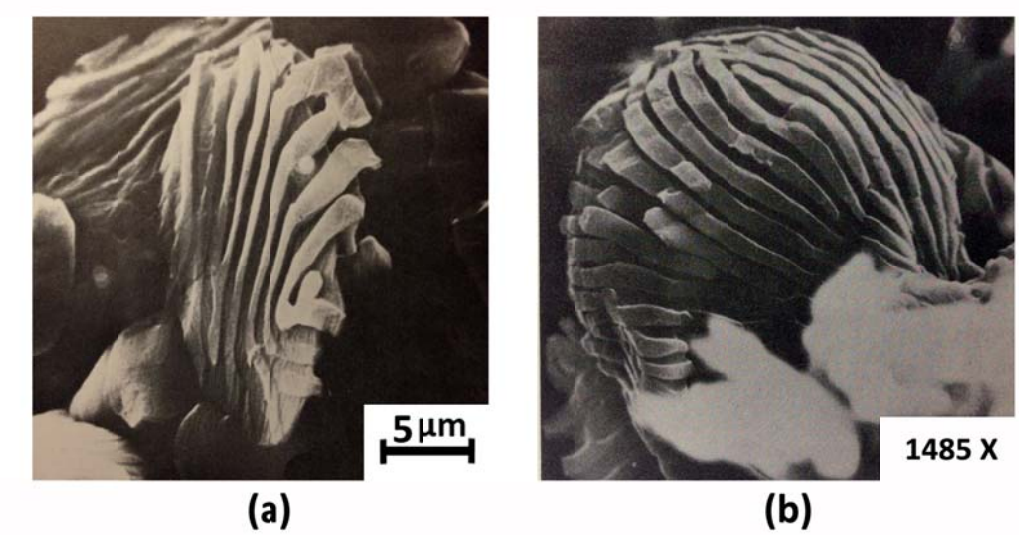

Fig. 38. Graphite crystals growing in the Ni-C-B system a)graphite flake b) graphite sphere [70, 136]

1.9. Single layer graphene

Single layer graphene (SLG) is a two dimensional sheet of sp^2 bonded carbon atoms in a honeycomb network. The three valence electrons of each three carbon atoms in the graphene sheet will create the crystal lattice. This will result in floating of one electron freely and releasing from chemical bonding. All of these free electrons then create a sea of electron which allows them to transfer current with almost no resistance. Therefore, in band structure of graphene the conduction and valence bands just meet at the Fermi energy and the band gap is accordingly zero. The terms "massless Dirac fermions" for graphene carriers is due to this electronic band dispersion. Band structure of single layer graphene has been shown in Fig. 39.

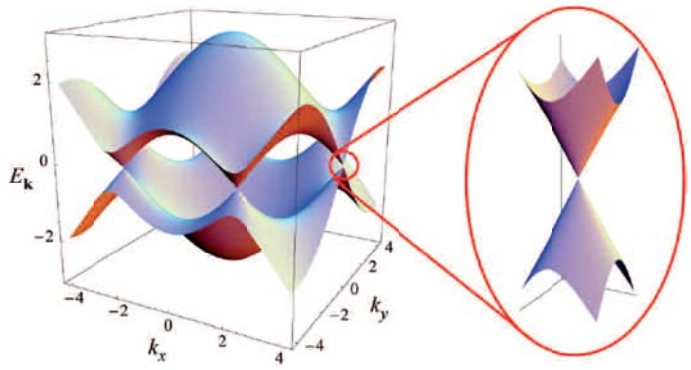

Fig. 39. Single layer graphene band structure [137]

It is observed in Fig. 39 that the π-band energy dispersion relation for graphene near the six corners of the 2D hexagonal Brillouin zone is linear and therefore cones of carriers (holes and electrons) exist in the corners of a 2D Brillouin zone whose points touch at the Fermi energy.

This graphene sheet could be the basic building block of important allotropes of carbonic materials; the stacking of graphene layers in 3D space can form the graphite. It can also be wrapped up into 0D fullerenes or rolled into 1D nanotubes [138].

For a long time it had been thought that two dimensional crystals are thermodynamically unstable at finite temperatures since any atomic monolayer was assumed to roll or fold in order to achieve its lowest potential energy. However, later with using electron microscopy it was observed that there are small ripples in graphene preventing it from rolling into nanotubes or other carbonic structures [138].

Since graphite is stacks of graphene layers, isolation and separating of graphite layers with mechanical forces was always thought as a viable technique for manipulating nano graphitic layers and even single layer graphene. Accordingly the scientists used mechanical exfoliation of graphitic layers to produce thin sheets for some time. In 1999, with utilization of an atomic force microscope (AFM) tip, small pillars were patterned into highly oriented pyrolytic graphite (HOPG) by plasma etching [139]. The thinnest sheets that could be obtained by this technique at the time were 200 nm (600 layers of graphene). Later this technique was modified by transferring the pillars to a tipless cantilever which stamped down slabs on a SiO_2 substrate [140]. The schematic of the process has been shown in Fig. 40(a).

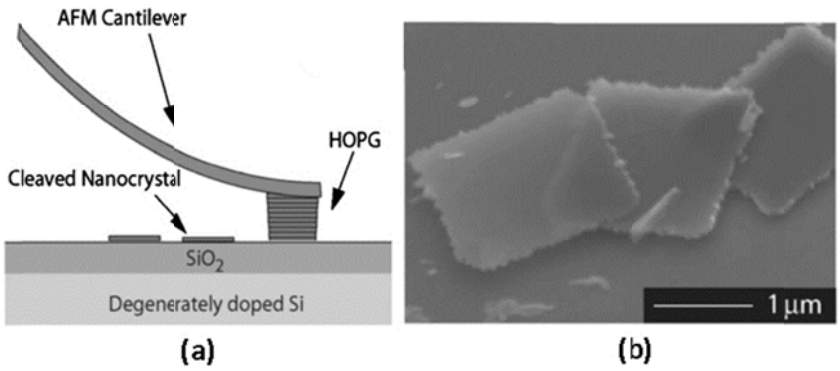

Fig. 40. a) Stamping down slabs of graphene on a SiO_2 substrate b) graphene layers exfoliated by (a) [140]

The sheets isolated with this technique, shown in Fig. 40(b), were as thin as thin as 10 nm (30 layers). In 2001 a single nano-sized graphene sheet was prepared by electrophoretic deposition (EPD) and heat-treatment of diamond nano-particles on HOPG substrate at 1600 °C. The mean in-plane size of the nano-graphene and its inter-layer distance from the substrate were estimated at 10–15 and 0.35–0.37 nm, respectively [141]. Above all of these techniques, the most successful one that resulted in isolation of single layer graphene was a simple approach known as "scotch tape technique" [142]. In this technique a celluphene tape is used to peel off the graphene layers repeatedly [138, 142, 143].

1.9.1. Single layer graphene properties

From the discovery of single layer graphene, numerous researches have been conducted to define its mechanical, electrical and thermal properties. The mechanical properties of the free-standing graphene were measured by indenting the film with an AFM cantilevers

with diamond tip [144]. The results correspond to a Young's modulus of E = 1.0 TPa, intrinsic strength of σ_{int} = 130 GPa and spring constants ranging from 1 to 5 N/ m. These values establish graphene as the strongest material ever known with a strength of two hundred times more than that of steel [145].

Moreover, experimental results from transport measurements also showed that graphene has high electron mobility of 15000 $cm^2V^{-1}s^{-1}$ at room temperature [138]. The corresponding resistivity of the graphene sheet is found to be 10^{-8} Ω·m, which is even less than the resistivity of silver, the substance with the lowest resistivity known at room temperature. The superior electrical properties of graphene have not yet been observed in any other element or compound.

Furthermore, the thermal conductivity of graphene was also found to exceed ~3000 W/mK at room temperature for the large suspended graphene flakes [146-149]. The enhanced current and heat conduction properties are beneficial for electronic, interconnect and thermal management applications of graphene. It has also been demonstrated that graphene devices can operate at very low-levels of the electronic flicker noise, which is important for applications in sensors and communications [150-152].

1.9.2. Single layer graphene preparation techniques

There are different techniques for graphene preparation, above all, three major purposes are followed. First of all, the technique must produce high quality crystal in a 2D lattice

to ensure high mobility of carriers. Secondly, if the technique deals with growing of the single layers, it must provide fine control over crystallite thickness so that in the application inside the electronic device it delivers uniform performance. Finally the technique should be scalable industrially. Below some of the graphene preparation techniques are reviewd.

1.9.2.1. Mechanical exfoliation

In this technique the graphene layers are peeled off utilizing a scotch from a graphite flake. For this purpose millimeter-thick platelets of HOPG are pressed on a 1-mm-thick layer of a fresh wet photoresist spun over a glass substrate. Then the substrate is baked which leads to attachment of the flakes to the photoresist layer. The graphene layers are then peeled off form the rest of the HOPG by a celluphene tape. Finally thin flakes left in the photoresist are released in acetone and picked up by a Si wafer. The wafer is finally washed in water and propanol. The wafer is then investigated with optical microscope and Raman Spectroscopy for the possible presence of graphene layers. Fig. 41 shows mechanically exfoliated graphene layers on a Si wafer. The technique results in high-quality crystallites of more than 100 μm^2 in size [142]. It should be noted that due to light interference effect, single layer graphene is observable on a on Si wafer with a 300 nm SiO_2 [142].

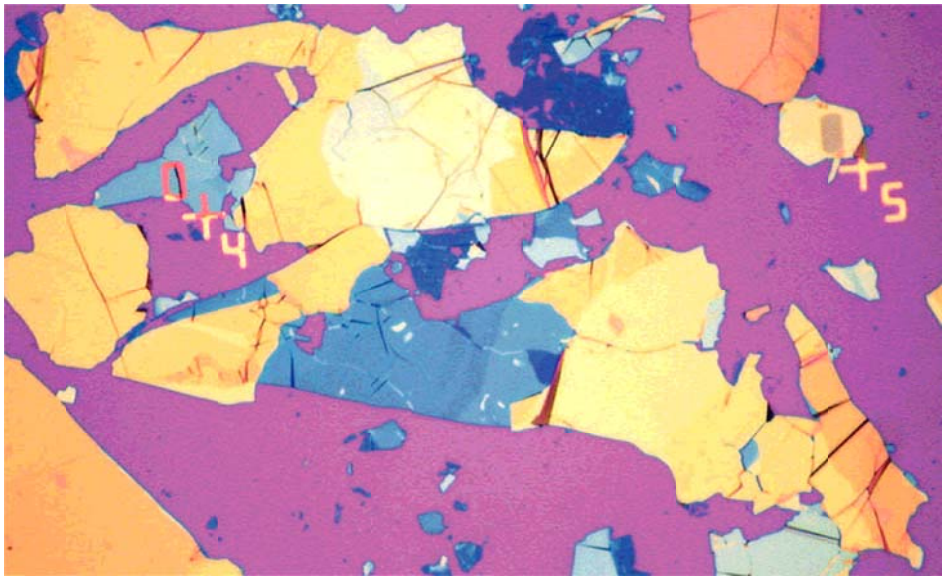

Fig. 41. Mechanically exfoliated graphene layers on Si wafer [137]

1.9.2.2. Epitaxial growth of graphene

In this technique graphene is prepared by high temperature sublimation of silicon from the surface of silicon carbide (SiC) [153]. For this porpose, a substrate of SiC is first flattered by oxidation or hydrogen etching and is then heated at high temperatures (1000-1500 ºC) and ultrahigh vacuums (10^{-10} Torr) [154]. This will lead to sublimation of silicon and leave behind islands of graphitized carbon. The photolithography can later be used to pattern epitaxial growth in predetermined locations and to make devices [155]. The epitaxial graphene properties are dependent on both the silicon carbide substrate and growth parameters [156, 157].

1.9.2.3. Chemical vapor deposition

In chemical vapor deposition (CVD) techniques, a hydrocarbon gas decomposes on a transition metal (substrate) at high temperature leaving behind carbon adatoms which grow as graphene layers [158-161]. The growth of graphene monolayers on single crystalline transition metals such as Ni [162, 163], Pt[164], Co [165] , Ru [166-168] and Ir [169, 170] is well known. However, there are different approaches for CVD growth of graphene which will be discussed here briefly. In the first approach, graphene layers nucleate and grow directly on the surface of a solid while a hydrocarbon gas decomposes on the surface in temperatures around 1000 °C [171-173]. Normally the graphene nucleation occurs on grain boundaries of solid substrate which leads to inhomogeneity in density and size distribution of graphene layers. So, liquefaction of the substrate may give rise to formation of a uniform layers graphene. Accordingly, the second approach is based on CVD growth of graphene layers on the surface of a melt [174] . In the third approach the carbon atoms coming from decomposition of a hydrocarbon gas diffuse into the metal in elevated temperatures. Later upon cooling, the substrate become supersaturated and excess amount of carbon diffuse to the surface and form graphene layers. It has been shown that in this approach cooling rate is one of the most critical parameters controlling the growth of thin graphene layers. In the case of extremely fast cooling rate the atoms will lose mobility before they can diffuse and accordingly in this case no layer could be formed at the surface. On the contrary at extremely slow cooling rate the carbon atoms will diffuse to the metal bulk so there will not be enough carbon segregated at the surface to form any layer. In the case of medium cooling rates, a finite

amount of carbon can favorably segregate at the surface which could form few and single layers graphene. This effect of cooling rate has been shown schematically in Fig. 42.

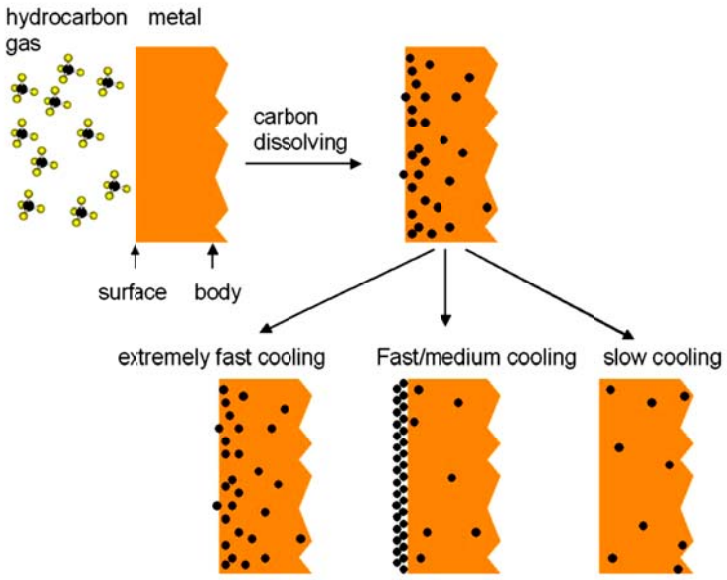

Fig. 42. Schematic of CVD process and carbon segregation at metal surface [160]

1.9.2.4. Graphite intercalation

Graphite can readily be intercalated using alkali metals due its layered structure. For this propose KC_8 (an intercalation compound) is synthesized by adding stoichiometric amounts of potassium and high-purity graphite at 200°C. Later while KC_8 is reacted with aqueous solvents solution of potassium ions along with hydrogen gas evolution will aid the exfoliation of graphitic layers. The exfoliated graphite sheets may curl onto themselves upon sonication and forming carbon nanoscrolls [175].

1.9.2.5. Chemically derived graphene from graphite oxide

In this method the graphite oxide dispersed in water is exfoliated with mechanical energy. Basically, the hydrophilicity of graphite oxide leads water to readily intercalate between the sheets and due to strength of interactions between water and the oxygen-containing functionalities in basal plane the graphene oxide layers will be exfoliated. The dispersed graphene oxide layer will later be reduced to single layer graphene [176].

1.9.3. Curved graphene layers

Due to the strong bonds of carbon in the graphene sheets, they can bend and form curved structures without losing their crystalline network. These curved graphene layers are good candidate for various applications including high energy density supercapacitor electrodes [177], modern optical devices [178], Reversible Hydrogen Storage [179] and electronic devices [180].

Nano-curved carbonic materials are currently synthesized by slow condensation of carbon vapor in high-temperature processes [1], ball milling [181], annealing of diamond particles [182] and unzipping of carbon nanotubes [183]. Molten metals can also be utilized as a medium for growing of curved graphene layers. For instance, the macroscopic curved graphite layers have been grown by melting small amount of iron on graphite in high vacuum by electrons bombardment [184]. The curved graphite by this technique had approximately 1 mm radius of curvature and consisted of solely one single arc shaped graphite.

Although graphene layers have been synthesized by different above-mentioned techniques, yet there is no report on growth of graphene layers from a molten phase. Moreover, despite all of the research in the growth of graphite from metal-carbon melts, the exact mechanisms of nucleation and growth of graphite and the characteristic of morphology changes due to variation of cooling rates are not fully understood yet. In this research, the graphene layers have first been synthesized on the surface of metal-carbon melts. Later different morphologies of graphite grown within the melt along with their nucleation and growth mechanisms were investigated.

Chapter II

Experimental Procedures

Since the main scope of his research was investigation of graphene layers growth from a metal-carbon melts, different metal-carbon systems and melting processes were deployed which will be explained below.

2.1. Alloys preparation

Ni and Al chunks (99.99%) and Cu (99.99%) wire of 0.25" diameter by Alfa AESAR™ and graphite powder or chunk (99.98%) by POCO™ graphite were selected as raw materials. For alloying of carbon and metal two approaches were utilized. First, the desired amounts of carbon were added to the molten metal in the form of graphite chunk or powder inside copper chilled plate or boron nitride crucibles. Second, the melting process of the metal was carried out in graphite crucibles as carbon source.

2.2. Melting process

2.2.1. Arc melting

For the arc melting process a Centorr™ arc-melting furnace was utilized which has been shown in Fig. 43. The arc melting furnace utilized a Direct-Current Electrode Negative (DCEN) process. The processing chamber was initially vacuumed to 150 μm-Hg and then backfilled with argon for two times to minimize oxidation during the arc-melting process. Prior to each melting, a titanium getter was remelted to absorb the remaining oxygen of the chamber.

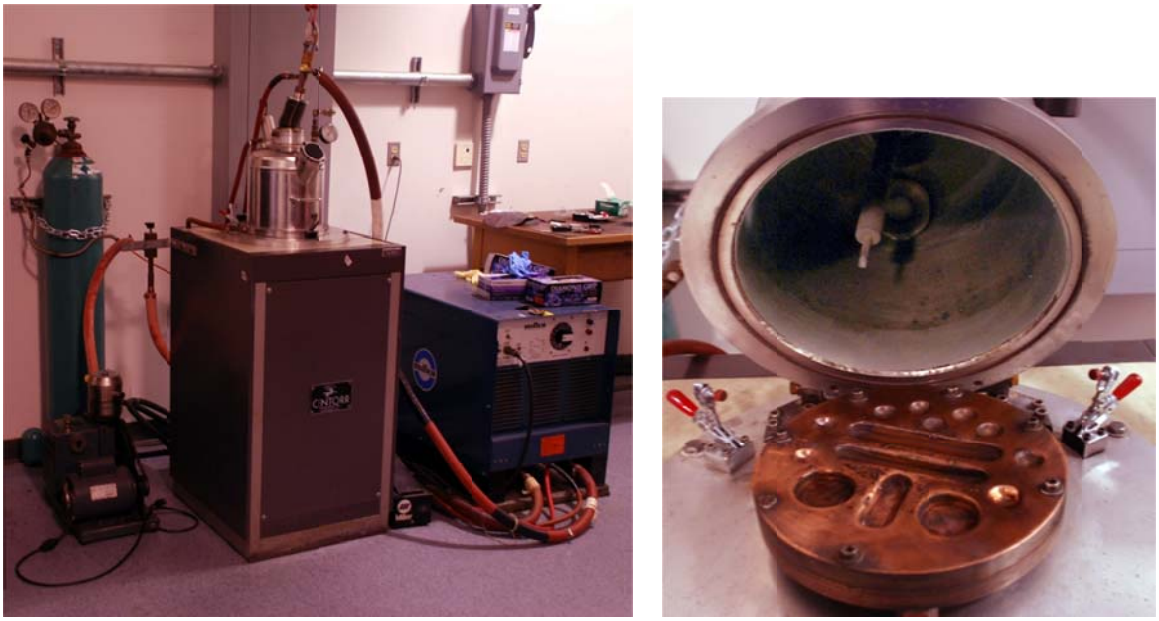

Fig. 43. Arc-melting furnace

2.2.2. Resistance melting

Another approach for alloying was use of a resistance furnace which has been shown in Fig. 44(a). For this purpose metal shots were placed inside machined graphitic crucibles which have been shown in Fig. 44(b). Upon putting the samples inside the furnace, the chamber was first vacuumed to 10^{-6} torr and then backfilled with purified argon. After reaching 1500 °C, the samples were kept for 16 hours and then cooled to ambient temperature. Both heating and cooling rates were 10 °C/min.

(a)

(b)

Fig. 44. a) Utilized resistance furnace b) graphitic crucible used for malting process inside the resistance furnace

2.2.3. Electromagnetic levitation

In order to achieve containerless melting process, an Electromagnetic Levitation (EML) apparatus were used for this study. The 1.5 g shots of metal-carbon which had already been alloyed in arc melting furnace were levitated in the EML apparatus, schematically shown in Fig. 45. The levitation coil was made of a dehydrated-soft copper refrigeration tube of 1/8" O.D. x 0.030" wall thickness sleeved with insulating fiberglass. The sleeved coil with a desirable length was cut and both ends were drilled to ensure decent cooling water flow through the coil. The coil was then shaped into a configuration consisted of a double wound in opposite directions. It was important to minimize the spacing between each round to ensure the uniformity of the magnetic generated by this coil. The coil was then powered by a 20-kW high-frequency (8 MHz) generator. A two-color pyrometer was employed to measure the temperature of the sample continuously. The accuracy of the pyrometer readings was checked by measuring the melting temperature of pure nickel and pure copper. It was found that the measured temperatures were within ±10 °C of the expected values with small oscillations due to sample rotation and vibration, as well as liquid circulation. Based on computed velocity and temperature fields for a 6-mm-levitated iron droplet proposed [185], a severe circulation is expected within the sample as well. The fluid flow field in levitated metal droplets can only be driven by two forces, i.e., electromagnetic force and the buoyancy force fields. The computational analysis of the temperature and flow fields in the levitated droplet can be found in [185]. This vigorous circulation causes a uniform temperature distribution with a maximum 7 °C difference from surface to core of droplet.

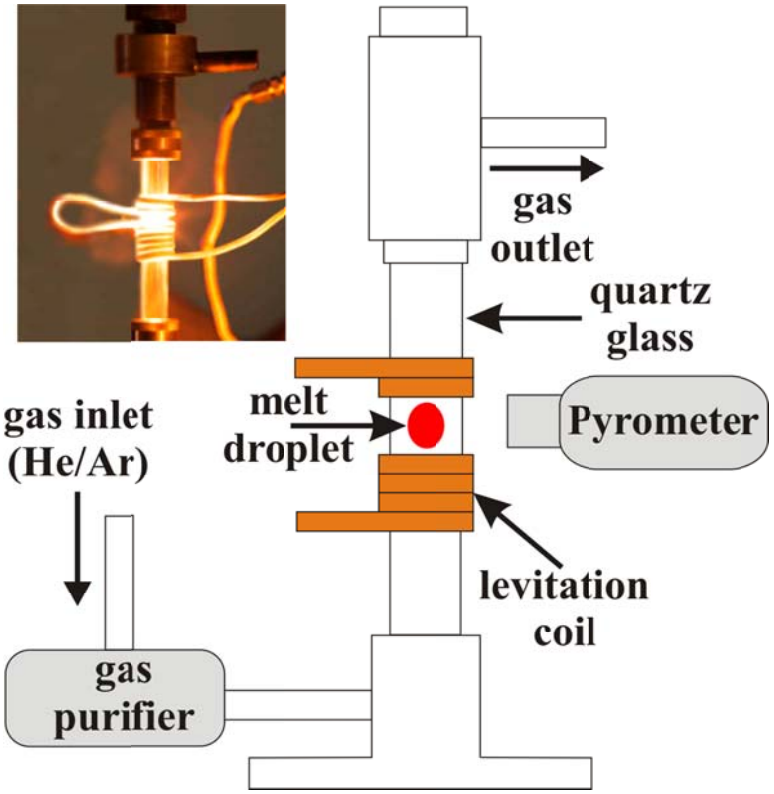

Fig. 45. The electromagnetic levitation apparatus used for containerless melting processes

2.2.4. Induction melting

For induction melting the same power supply and gas delivery system of EML apparatus were used. However, a copper coil with 0.25" O.D. which was wounded 5 times in the same direction was used to induct the heat. The metal shots were then placed inside a boron nitride or graphitic crucible for the melting process. The configuration of the induction melting process has been shown in Fig. 46. A quartz tube with 16-mm diameter and 0.5-mm thickness was inserted inside the coil through which inert gases of Ar and He flowed to prevent melt oxidization and cooling. Both argon and helium gases were purified prior to entering the system using a gas purifier with a titanium getter at 800 °C.

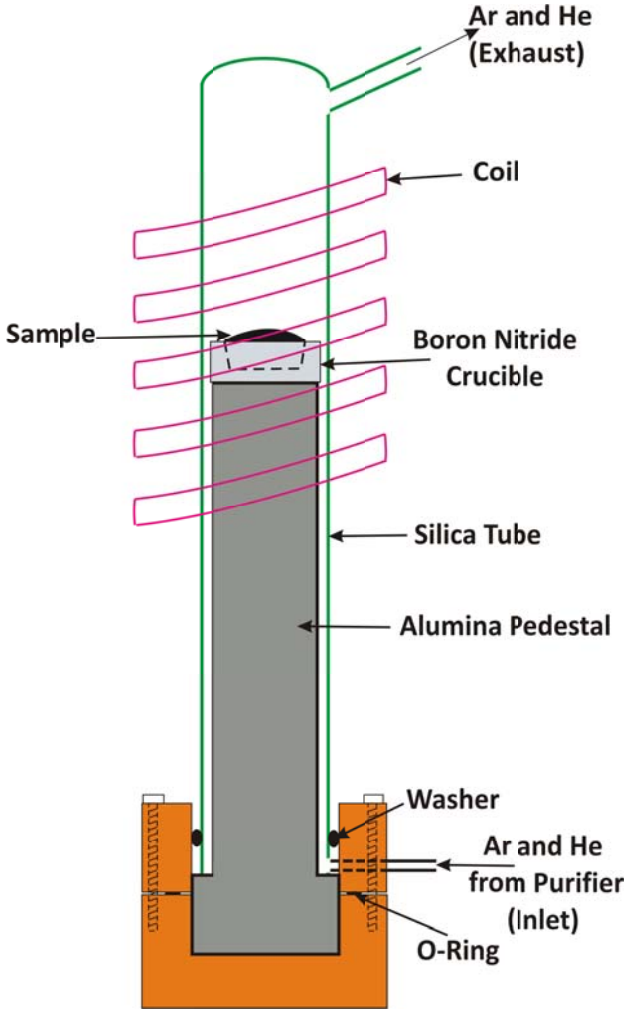

Fig. 46. The configuration of the induction melting process

2.3. Sample preparation for characterization

2.3.1. Transfer of graphene layers

For better characterization of graphene layers grown in the surface of the melts, the graphene layers were transferred to a silicon wafer by the method previously reported for the transfer of carbon nanotubes and graphene layers [186, 187]. To achieve this, a layer of poly methyl methacrylate (PMMA) was spin coated on the substrate (1800 rpm for 30 seconds). Afterwards, the metal substrate was etched away by a nitric acid solution (1:2) allowing the PMMA/carbonic layer to float on top of the solution. The layer was then placed on a glass substrate and washed with isopropanol and water. The dual layer of PMMA and carbonic layer was then transferred to a Si/SiO_2 wafer. The film was annealed at 60°C for 1 hour to adhere firmly to the target substrate. The PMMA is then dissolved with the acetone drops gradually and the carbonic layers are left on the substrate. The wafer with the carbonic layers is washed with isopropanol and dried with the nitrogen gas.

2.3.2. Polishing and etching

The specimens were sectioned using a South Bay Technology™ diamond saw and then mounted using a Buehler™ mounting apparatus. The specimens were then grinded using 180, 400, 800 SiC grinding papers for a rough surface finishing. The polishing solutions for a fine surface finishing were the water-based alumina (α-Al_2O_3) solutions of 1 and

0.05 micron accordingly. The specimens were finally etched using HCl-H_2O-$FeCl_3$ (50mL-100mL-5g) solution to reveal the microstructures.

2.4. Characterization techniques

2.4.1. Microscopy

The microstructure of polished and as-received samples were mapped using a Nikon™ stereo microscope and a Nikon™ Optiphot equipped with a digital imaging system with a Nikon™ Coolpix 5000 digital camera. The electron micrographs of the samples were captured using a XL30 FEG scanning electron microscope. The chemical composition of different phases were determined by energy dispersive spectroscopy (EDS) system at 20 kV using a standard ‘‘ZAF’’ (Z-atomic number, A-absorption, and F-fluorescence, plus background and dead time corrections) technique.

2.4.2. Raman spectroscopy

Raman spectroscopy has been utilized as a convenient technique for identifying and counting graphene layers [188-191]. Raman spectroscopy has been carried out using a Horiba Jobin Yvon micro-Raman spectrometer. All spectra were excited with visible (632.8 nm) laser light (power 3.6mW) and collected in the backscattering configuration. The spectra were recorded with a 1800 lines/mm grating. A 100X objective to focus the excitation laser light on different spots of the samples were used.

The most prominent features in the Raman spectra of graphitic materials are the G band (~1582 cm^{-1}) , D band (~1350 cm^{-1}) ,D´ band (~1620 cm^{-1}) and the 2D band (~2700 cm^{-1}) [188, 192]. The G band is Raman active for sp^2 carbon networks. In contrast, sp^3 and sp carbon show characteristic Raman features at 1333 cm^{-1} (diamond) and in the range 1850–2100 cm^{-1} (linear carbon chains), respectively. The D and D´ bands are defect induced Raman features. Thus these bands cannot be seen for highly crystalline graphite without any defect. The integrated intensity ratio for the D band and G band (I_D/I_G) is widely used for characterizing the defect quantity in graphitic materials. The 2D (or G´) band corresponds to the overtone of the D band observed in all kinds of graphitic materials and exhibit a strong Raman band which appears in the range 2500–2800 cm^{-1}.It has been shown[188] that the evolution of the 2D band Raman signatures with the addition of each extra layer of graphene can be used to accurately count the number of layers. A rough estimate on the number of layers can also be obtained from analysis of I_G/I_{2D} ratio [188, 193]. What is also important in our case is that the micro-Raman spectroscopy based graphene identification was shown to be reliable for graphene on various substrates (not only on Si/SiO_2) [194, 195]. It also has been shown that among the metallic substrates, nickel is an appropriate one for direct Raman Spectroscopy investigation[160].

Chapter III

Synthesis of graphene layers

3.1. Synthesis of graphene layers on the surface of the melt[1]

The technique is based on dissolving carbon atoms in a transition metal melt at a certain temperature and then allowing the dissolved carbon to grow out at a lower temperature as single layer graphene. The schematic of the process with nickel is shown in Fig. 47.

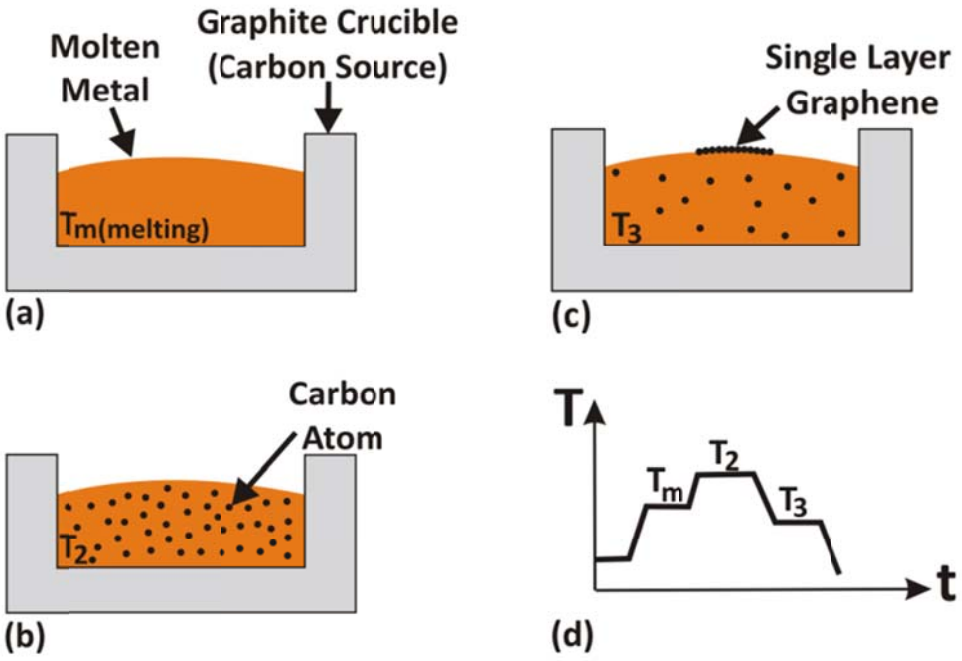

Fig. 47. Schematic of graphene growth form molten nickel a) Melting nickel in contact with graphite as carbon source, b) dissolution of carbon inside the melt at high temperatures, and c) reducing the temperature for growth of graphene. d) shows temperature-time Diagram of the process

[1] Partially reprinted from Journal of Applied Physics, Vol. 108, S. Amini, J. Garay, G. Liu, A. A. Balandin, and R. Abbaschian, ″Growth of Large-Area Graphene Films from Metal-Carbon Melts″, Issue 9, p 09432, Copyright © 2011, with permission from American Institute of Physics and Journal of Materials Science, Vol. 46, S. Amini, H. Kalaantari, J. Garay, A. A. Balandin and R. Abbaschian , ″ Growth of graphene and graphite nanocrystals from a molten phase ″, No. 19, pp 6255-6263, Copyright © 2011, with permission from Springer.

In Fig. 47(a) nickel is melted in contact with a carbon source. As the carbon source one can use a graphite crucible (in this case the melting process is carried out inside the crucible), graphite powder or chunk, which is simply placed in contact with the melt. Keeping the melt in contact with carbon source at a given temperature results in carbon's dissolution and saturation of carbon atoms in the melt. The process is described by the binary phase diagram of metal-carbon [Fig. 47(b)]. Upon lowering the temperature, the solubility of carbon in the molten metal decreases and the excess amount of carbon precipitates on top of the melt [Fig. 47(c)]. The temperature-time diagram of the process is shown in Fig. 47(d). The floating layer can be either skimmed or allowed to freeze for removal. The described processing technique was utilized with copper and nickel for which the corresponding phase diagrams have been shown in Fig. 48. The processing temperatures, indicated in Fig. 47 are also shown in Ni-C phase diagram in Fig. 48(b).

The goal of this process is to grow single and few layer graphene controllably. Fig. 49 shows calculated thickness of graphene layers formed on the surface of supersaturated semispherical copper melts with different diameters (D) during cooling from different temperature. The graphs were obtained from the calculations based on the lever rule [3] on Cu-C phase diagram. Fig. 49 shows that cooling of the melt from 1200 and 1800 °C to the melting point of copper (1080°C) results in the formation of layers with the thickness ranging from several nanometers to several micrometers respectively. Selecting the higher alloying temperatures leads to dissolution of more carbon atoms in the melt and, consequently, larger amount of carbon precipitating on the melt upon cooling. The latter will result in the formation of a thicker graphite layer. However, the formed graphite

layer on the melt may not be uniform and its thickness varies from single layer graphene to bulk graphite. The thickness of the layers will be discussed in section 3.3.

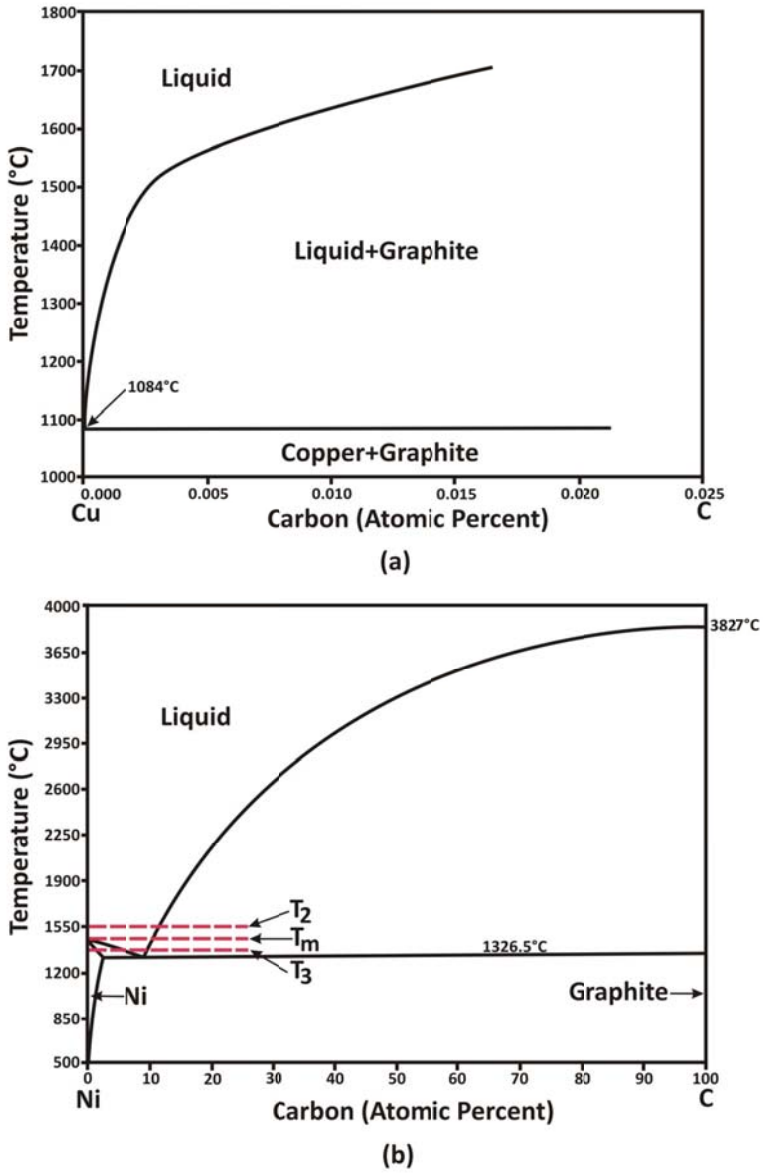

Fig. 48. Phase diagrams of selected binary systems a) Cu-C b) Ni-C the processing temperatures of Fig. 47 are marked in the Ni-C phase diagram

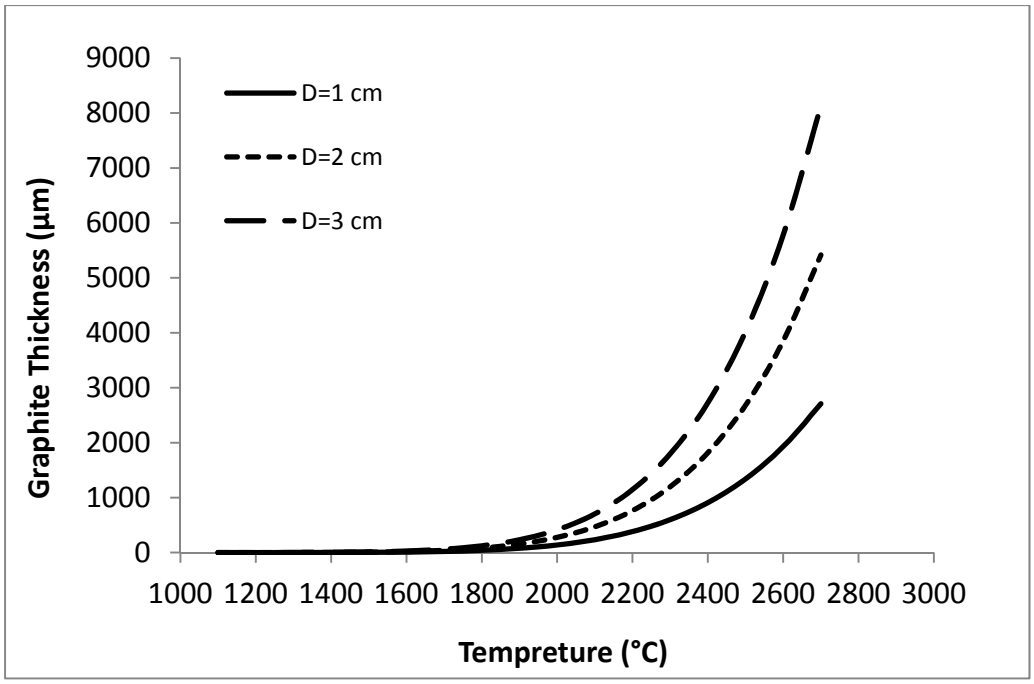

Fig. 49. Thickness of graphene layers formed on the surface of supersaturated semispherical copper melts with different diameters (D) during cooling from different temperature, calculated based on the lever rule on Cu-C phase diagram

Direct visual observation of graphite growth on top of the melt was utilized by means of a portable microscope. Fig. 50 shows video frames of a hypereutectic Ni-C melt which is cooled from uniform liquid to liquid + graphite region in phase diagram and once more heated up. Frames 1-4 demonstrate the cooling while the frames 5-6 show the heating process. The frames show two distinct regions of different brightness, with the brighter area showing graphite layer. The graphite is completely dissolved in higher temperature (frame 1). Nevertheless, there are observations that propose the phase in frame 1 is not purely bare metal and it is possible that thin graphitic shell is present over the entire surface [184]. As the melt is cooled down to lower temperature (liquid + graphite region) the excess amount of carbon grows as graphite patches on the surface (frame 2-3). With

continuous cooling those patches grow until they cover the entire surface (frame 4). This process is reversible as upon heating, the graphitic layer will dissolve back into the melt (frame 5-6).

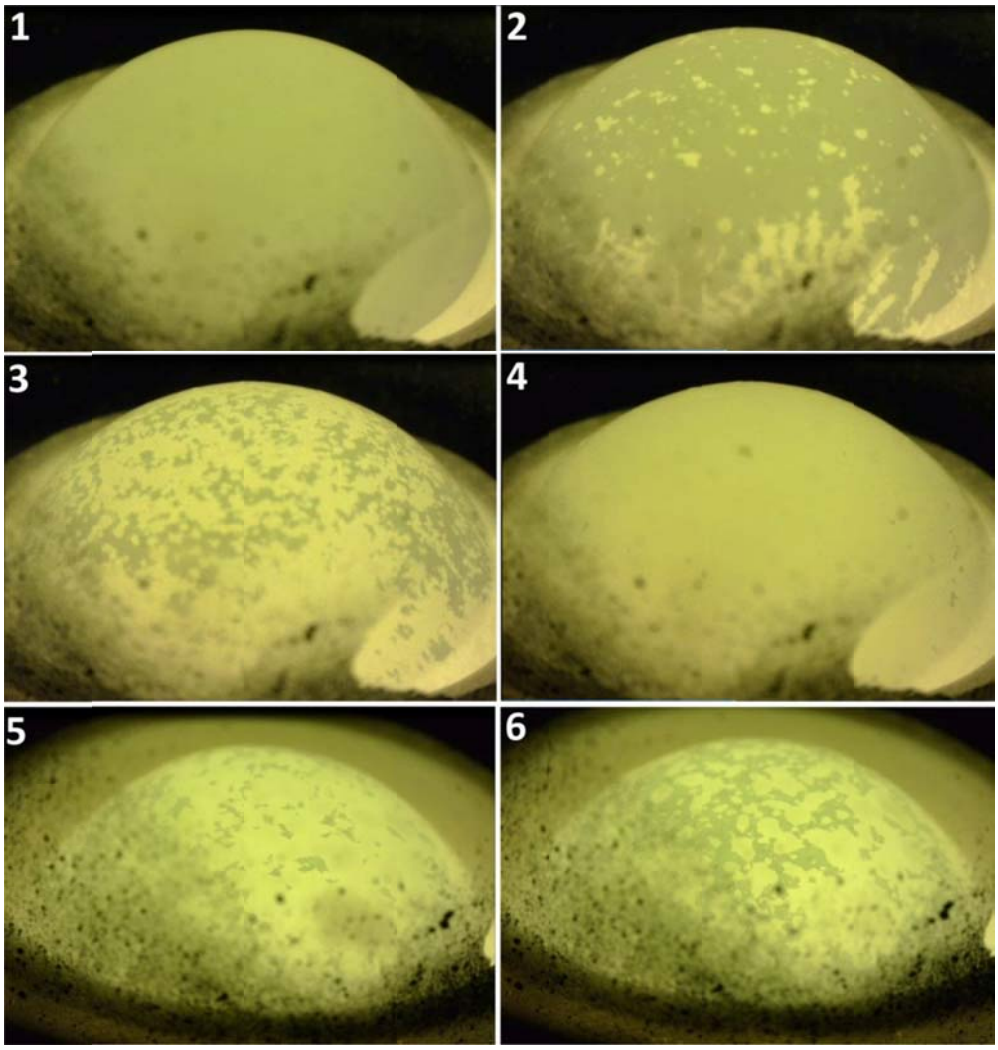

Fig. 50. Video frames of graphite growth on top of the melt: Frames 1-4 demonstrate the melt cooling and subsequent growth of graphite films, frames 5-6 show the melt heating and succeeding graphite dissolution (the brighter phase is graphite)

Fig. 51 shows a graphite film which has been skimmed from the surface of molten nickel by means of a boron nitride substrate during the growing stage (frame 3 in Fig.2). The boundaries show polygonal shape which is the characteristic of faceted growth of graphite.

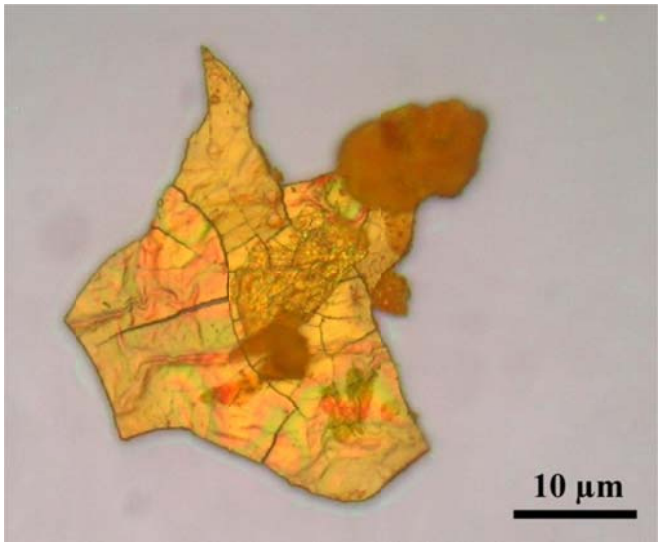

Fig. 51.Skimmed graphite film from the surface of molten nickel during early growth (Frame 3 in Fig. 50)

3.2. Morphology of surface graphene layers

Fig. 52(a) shows the graphite layer which has been formed on top of nickel upon complete solidification of the Ni+2.35wt%C melt. Magnified view of the layer in Fig. 52(b) reveals that the film has a specific morphology of smooth surface areas which have been separated from each other by out-of-plane faceted wrinkles. The structure at the joint between the wrinkles is more complicated, but the faceted structure is still evident. Fig. 52(c) shows typical Raman spectra of graphite in smooth areas and wrinkles. The two curves, which have been shifted slightly for the ease of visualization, are basically identical. The spectra show an intense G band as well as an asymmetric 2D band. No D (~1350 cm^{-1}) and D′ (~1620 cm^{-1}) bands could be noticed in either spectrum. As discussed in section 2.4.2, D and D′ bands are indicative of defects. Similar Raman Spectroscopy was carried out in different spots of the graphite and the results were identical.

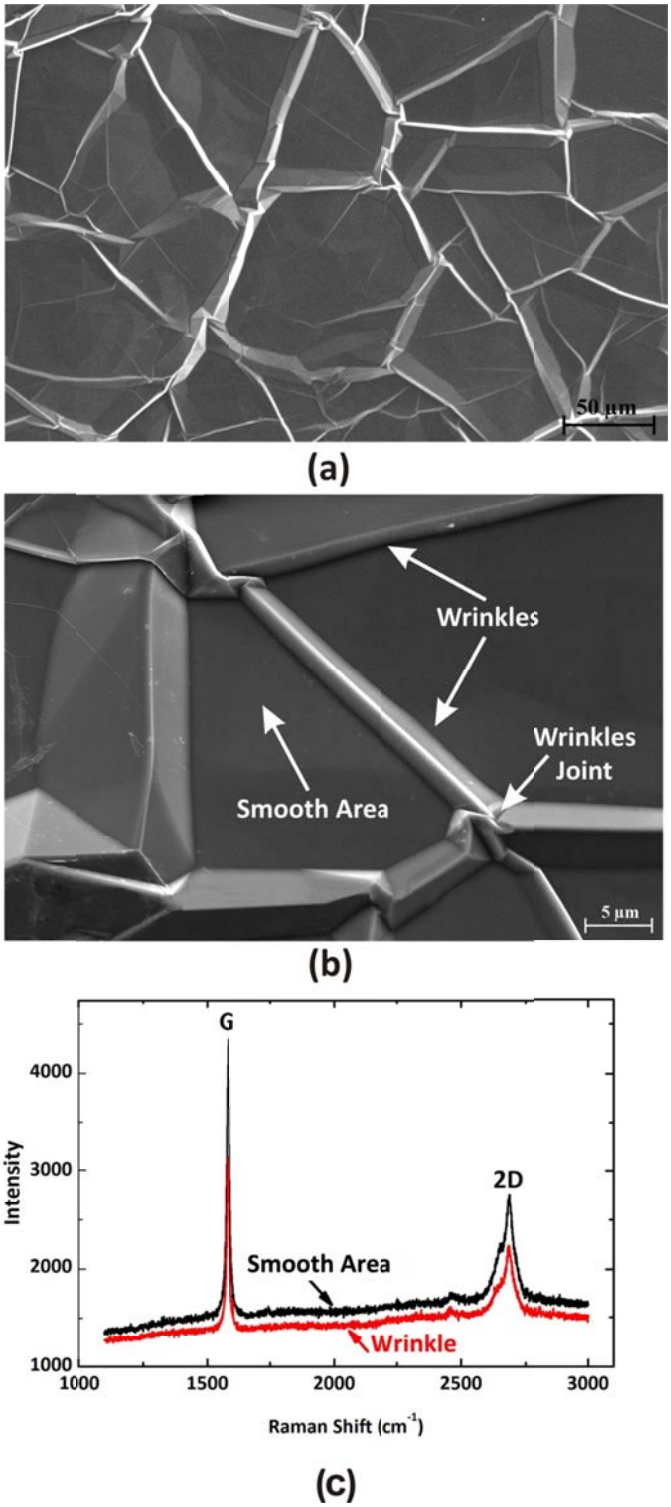

Fig. 52. a) SEM Photo of graphite layer formed on top of the nickel b) magnified view of wrinkles and smooth area in formed surface graphite c) Raman spectra of smooth areas and wrinkles

The Raman features shown in Fig. 52(c) were found to be similar to those of bulk crystalline graphite reported in literature [188]. By comparing the smooth areas and wrinkles Raman features it is evident that the structure of wrinkles is identical to flat areas. In fact, the wrinkles are part of the graphite film and hold the same crystal structure of flat areas.

The wrinkled feature of the graphite layers is believed to be due to the accommodation of the thermal expansion coefficient difference between the metal substrate and the graphite layer [196]. After the formation of the graphite shell on top of the melt and conclusion of the eutectic reaction both nickel and graphite contract as the sample cools down. The thermal expansion coefficient of nickel [197] varies from 21.0 to 12.89×10^{-6} K^{-1} for the temperature range from 1200 to 27°C while the in-plane thermal expansion coefficient of graphite [198] changes from 1.25 to -1.25×10^{-6} K^{-1} for the same temperature range. This difference in the thermal expansion coefficients gives rise to a larger lateral contraction of the metal substrate than that of graphite film. As a result, a compressive biaxial stress [196] will develop on the graphite layer which consequently leads to the formation of triangular folds in the film. The wrinkle formation is schematically shown in Fig. 53. The ab initio studies [198] as well as experimental results [1, 199] indicate that the bulk graphite below 400°C and single layer graphene possess negative thermal coefficient that intensify the thermal coefficient expansion mismatch even further.

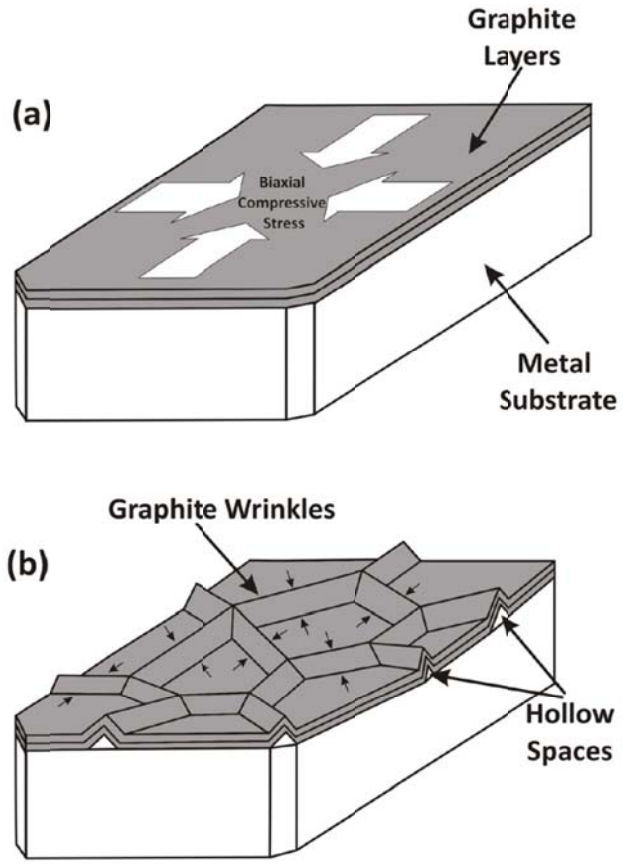

Fig. 53. Schematic of wrinkle formation on graphite layers due to thermal expansion coefficient mismatch

It is believed that the weak van der Waals forces among the graphene layers allow them to simply shift upward under the biaxial stresses. Although the individual layers are rather stable owing to the strong covalent bonds, the graphene layers can bend or fold without losing their crystal structure. It has been shown that deformation of graphene layers and formation of the creases are due to kinking [200] or twining [201]. The strong in-plane covalent bonds and the resilient structure of graphite are comprehended by the formation of these wrinkles. It is apparent that as the graphite films deform, they shift upward they lose their week out-of-plane bonds in some areas and detached from each

other. An example is shown in Fig. 54 as a wrinkle was cross sectioned using Focused Ion Beam (FIB). The hollow spaces which have been shown schematically in Fig. 53 can be observed clearly in the cross section of Fig. 54.

Fig. 54. Cross section of a wrinkle by Focused Ion Beam cutting

During the cooling, each individual wrinkles in the graphite layer contributes to the strain accommodation. The difference in thermal strain of graphite layer and nickel is $\Delta\varepsilon = \Delta T(\alpha_{Ni} - \alpha_{gr})$, where α_{Ni} and α_{gr} are the bulk and in-plane thermal expansion coefficients of nickel and graphite and can be found as functions of temperature in literature [1, 197, 198]. For calculating the thermal strain, the mean values were selected for nickel and graphite which are 18.04×10^{-6} and $0.5\times10^{-6}\,K^{-1}$ respectively. The total strain needed to be accommodated is then $\Delta\varepsilon = (T_{eutectcic} - T_{ambinet})(\alpha_{Ni} - \alpha_{gr}) = 0.023$. Based on the examining of different wrinkles on the surface, the lateral size and roof

angle can be considered approximately L=10 μm and φ=120° respectively. Based on the wrinkles geometry, the amount of layered material shifted from adjacent regions towards the wrinkle approximately corresponds to: $\Delta L = 2(L/2\cos 30) - L = 1.55\,\mu m$. To completely accommodate a 2.3 % strain, an array of wrinkles should be formed with spacing of: $r = \Delta L / \Delta\varepsilon = 67\,\mu m$. This value is as the same order of magnitude (50 μm) which is observed in Fig. 52(a).

3.3. Thickness of surface graphene layers

Various thickness of graphene layers were observed on the surface of metals. The examples of thick graphite layers were previously shown in Fig. 52. In Fig. 55, the SEM photos of electron-transparent graphitic layers on metallic substrate have been shown. Layers Transparency indicates that the layers are thin enough to serve as window for 5 keV and 10 keV electrons to pass along.

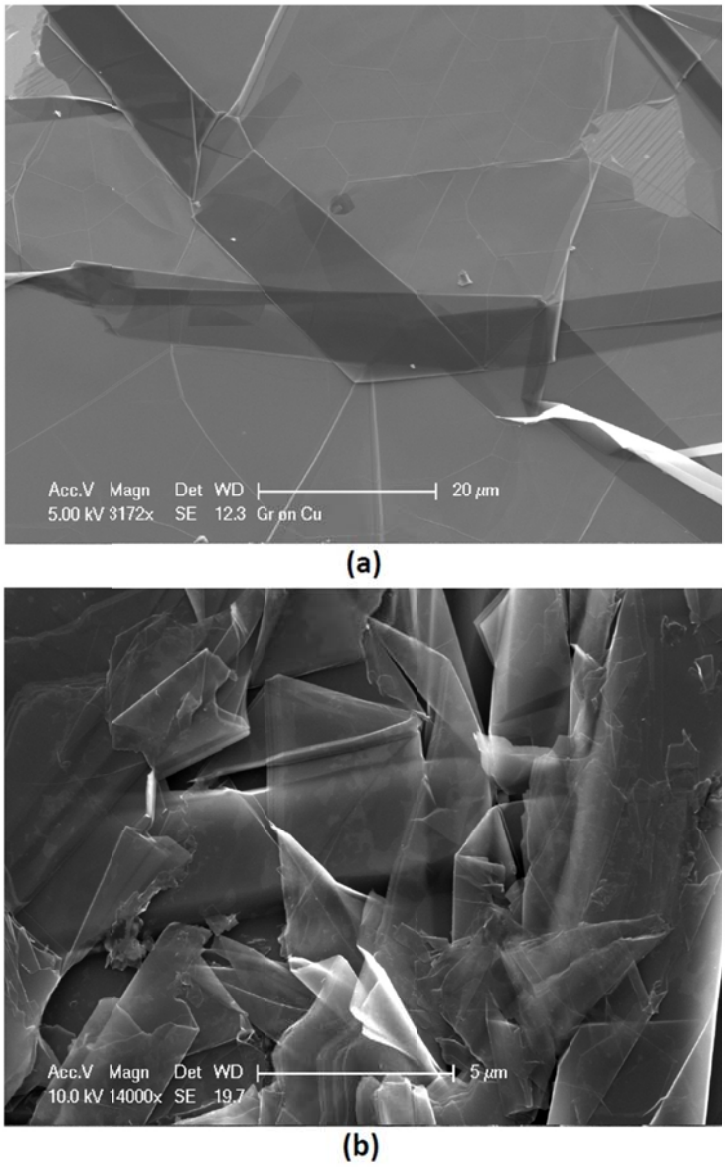

Fig. 55. SEM Photo of electronically transparent thin graphite films on (a) copper and (b) nickel

In Fig. 56(a) the few layer graphene formed on the surface of nickel has been shown. The Raman spectrum shows a G band at 1583 cm^{-1}. The 2D band deconvolution reveals two Lorentzian peaks at $2D_1$= 2688 cm^{-1} and $2D_2$= 2660 cm^{-1} ($\Delta\omega$=28 cm^{-1}).

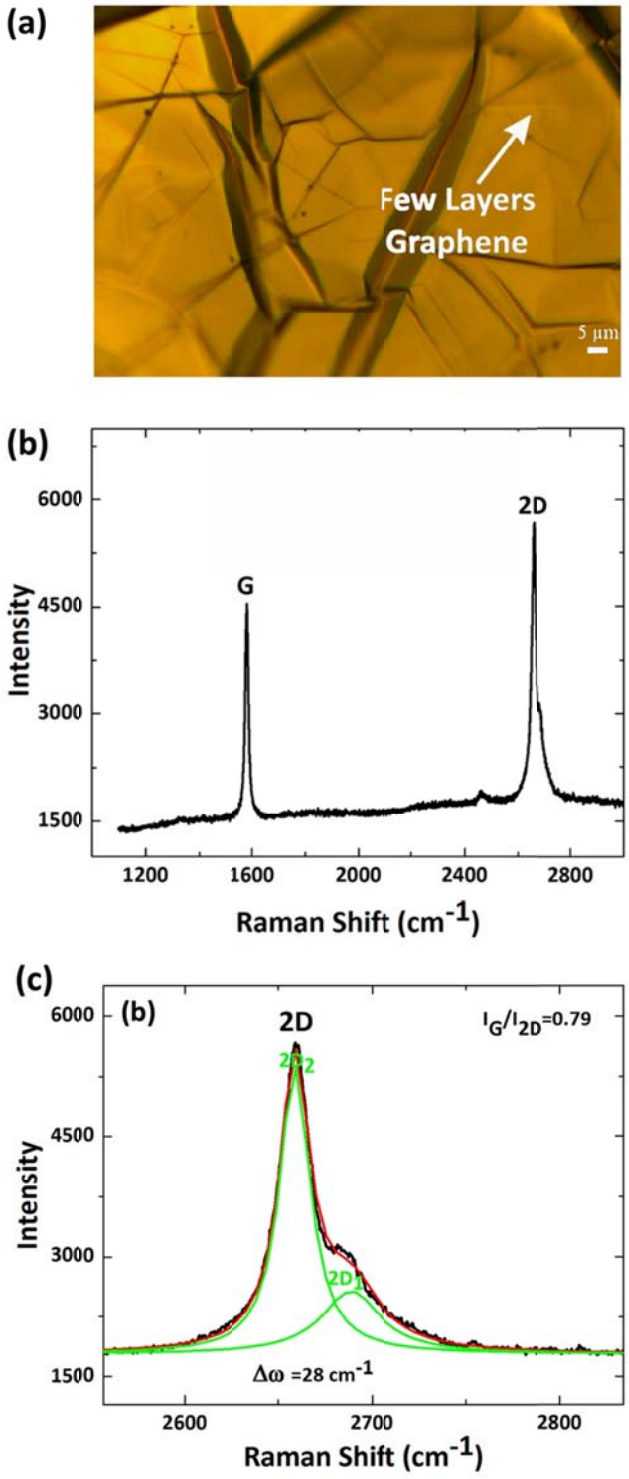

Fig. 56. a) Optical micrograph of FLG on nickel b) Raman spectrum of FLG formed on nickel c) deconvolution of 2D band in (b)

The characteristic of the Raman bands and I_G/I_{2D} ratio in Fig. 56(b) along with the deconvolution of 2D band in Fig. 56(c) indicate the presence of 4-layer graphene [191, 193, 194, 202]. The absence of D and D′ bands represents defect free few layer graphene on nickel.

Additional details of one of the grown few layer graphene island, which was transferred to silicon wafer, have been shown in Fig. 57(a). Different color contrasts in this film indicate areas which are rather thick, but connected by thinner regions, similar to that shown schematically in Fig. 57(b). As a graphitic layer nucleates on the melt, it expands laterally and normally by 2D nucleation and faceted growth, in a manner similar to that observed for 2D nucleation and growth of faceted materials [56]. The Raman spectrum shown in Fig. 57(c) represents the region which labeled as "few layer graphene" on the film. The I_G/I_{2D} ratio is the evidence that the existing flake has few graphene layers. The spectrum features a symmetric 2D band and intense D and D′ bands. The symmetric 2D band denotes the existence of turbostratic graphite (without ABAB stacking). The intense D and D′ peaks show layers with have high amount of defects.

Few layer graphene can also be formed at the edges of thick graphite. By transferring the graphitic layers to Si/SiO_2 substrates it was found that the color contrast at the edges of formed graphite islands is different. Thus, there is a possibility of finding few layer graphene at the edges. One of the islands grown on copper and the Raman spectrum of its edge are presented in Fig. 7. The spectrum features a symmetric 2D band and intense D

and D′ bands. The I_G/I_{2D} ratio indicate the presence of 5-6 layers graphene[189]. The symmetric 2D band again suggests a possibility of formation of turbostratic graphite.

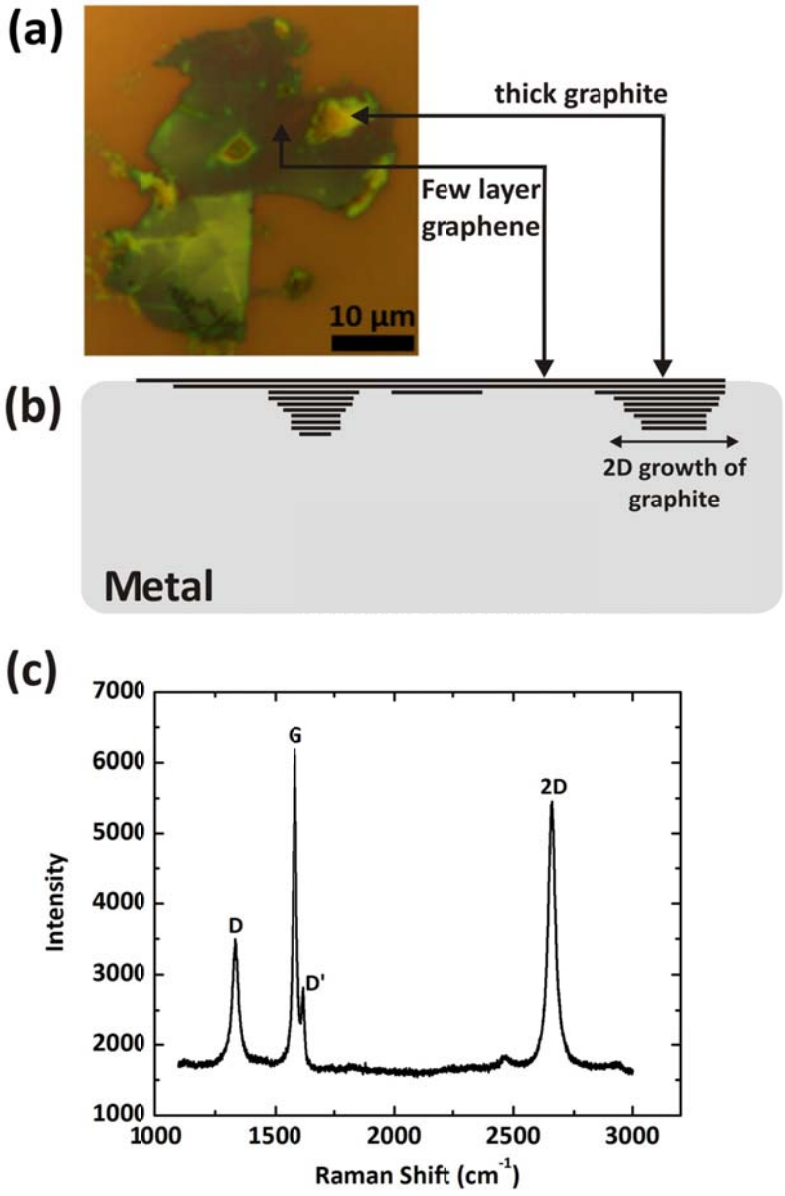

Fig. 57. a) Optical Microcopy of a graphite film formed on copper and then transferred to Si/SiO2 , b)schematic of 2D growth of graphite, c) Raman spectrum of the spot labeled as “few layer graphene” in (a)

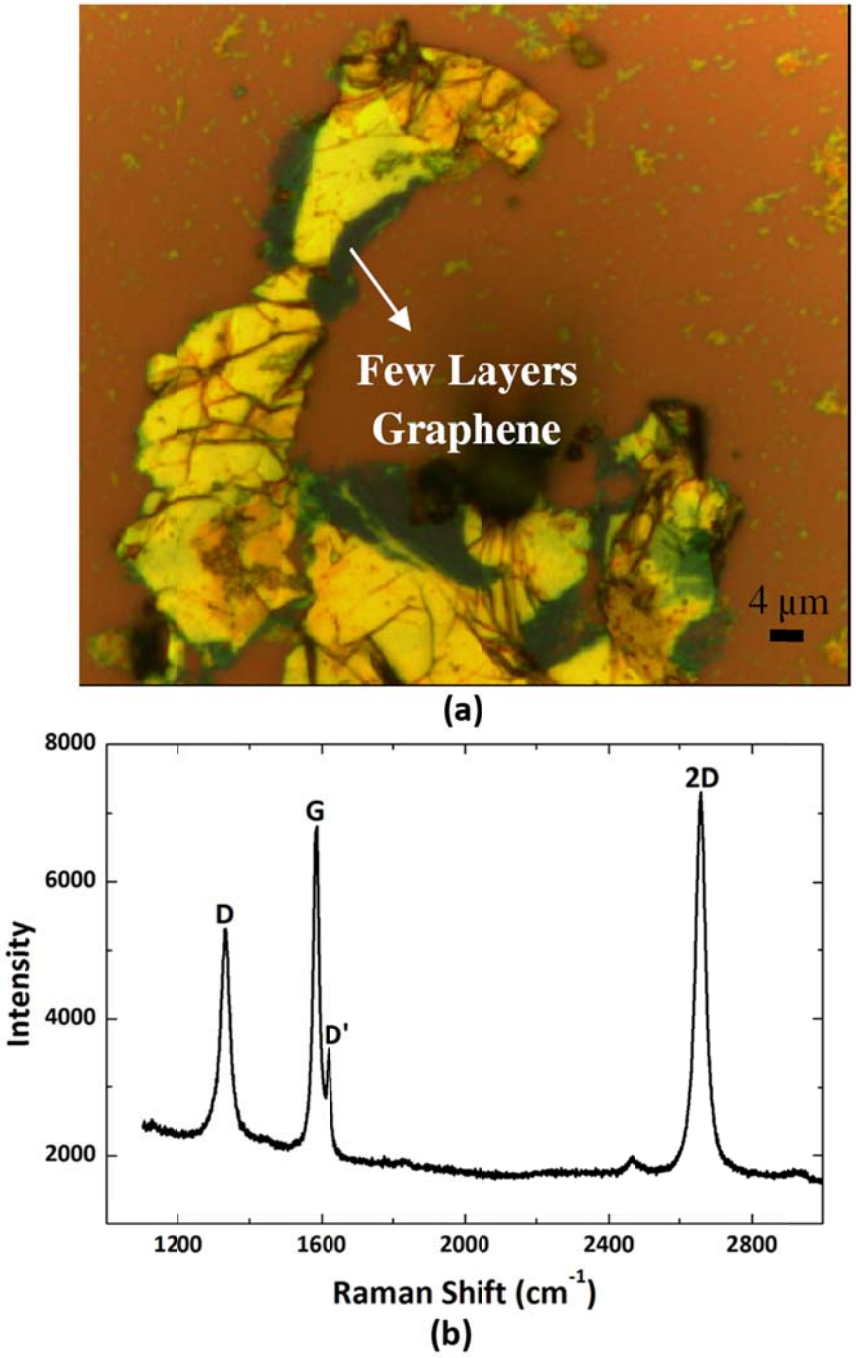

Fig. 58. a) optical Microcopy of a graphite island formed on top of copper and then transferred to Si/SiO_2
b) Raman spectrum at the edge of island

The large number of defects in Raman spectra of formed layers on copper due to intense D and D′ peaks (Fig. 57 and Fig. 58) is believed to be due to high cooling rate of copper. The high thermal diffusivity of copper (nearly five times of nickel) will lead to high cooling rate and consequently more defect formation including cracks and entrapped vacancies [203]. The lower thermal diffusivity of nickel will result in lower cooling rate and subsequent pristine graphene films formation (Fig. 56).

Interestingly, nickel substrate was found to have inactive Raman spectrograph and not affecting the Raman features of graphene and owing to this fact nickel lends itself as an appropriate substrate for direct characterization of graphene layers without the need for transferring the layers to silicon wafer. Pristine SLG layers were observed in various locations on nickel substrate. A pristine SLG and its Raman spectrum are shown in Fig. 59. The area of the grown SLG is larger than 125 μm^2. The Raman spectrum in Fig. 59(b) shows G band at 1583 cm^{-1} and an asymmetric 2D band at 2660 cm^{-1}. The absence of D peak proves that the formed SLG is high-quality and defect free. The full length at half maximum (FWHM) of the Raman peak of the grown SLG is 17 cm^{-1} (as compared to the reported value of 25 cm^{-1} [188]). The I_G/I_{2D} ratio is 4.53 and the deconvolution of 2D band indicates a complete symmetry as it is expected for SLG.

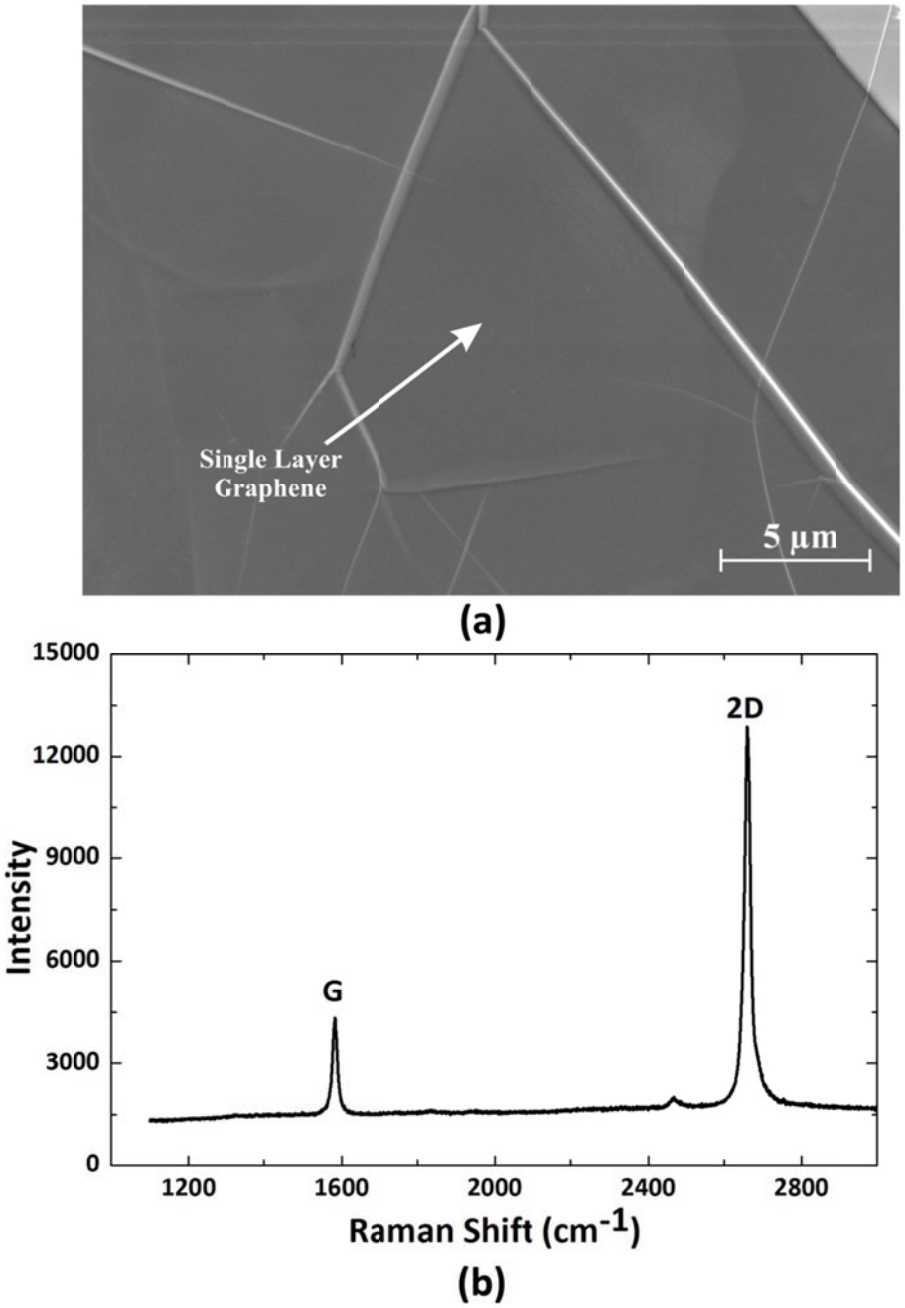

Fig. 59. a) SEM photo of Single layer graphene formed on nickel b) its Raman spectrum

The amount of graphite forming on the melt and its characteristic will strongly depend on the amount of carbon dissolved in the melt and the solubility limit of carbon in the liquid as well as cooling conditions employed. For the present investigation the two alloy systems of Cu-C and Ni-C show extensive differences in solubility limit. It appears that the Ni-C system is more conducive to the formation of large and defect free layers.

One should mention here that the formation, structure and energetics of the growth of single and few layer graphene from molten metal have many features in common with the mono-layer and multi-layer carbon formation by segregation and precipitation from the bulk solid solutions. In particular, the data on the equilibrium segregation of carbon to nickel surface and carbon interaction with nickel surfaces investigated in details and reported earlier [204-210] can be used for optimization of graphene growth from the metal-carbon melts proposed in this work.

The developed technology can lead to applications of the resulting graphene-metal composites as thermal interface materials (TIM) for heat dissipation in electronic chips and other devices. The layered graphene-metal composites are expected to have enhanced thermal conductivity exceeding that of metals [146, 147]. The improved thermal management and advanced TIMs are currently important areas of research due to increasing power dissipation in state-of-the-art electronic, optoelectronic and photonic devices [211].

3.4. Synthesis of curved graphene layers on metallic dendrites[2]

Based on the nickel-carbon phase diagram [4], upon cooling of a hypoeutectic alloy, the first phase to solidify is nickel, which initially grows with plane front, and eventually forms dendrites. The microstructure of exposed Ni-Cu dendrites in the surface is shown in Fig. 60(a) During alloy solidification, carbon atoms are rejected by the solid and a boundary layer richer in carbon than the bulk liquid is formed at the solid-liquid interface. As the metallic dendrites continue growing, the amount of carbon in remaining liquid goes up to eutectic composition. Applying Scheil equation [3] reveals that prior to eutectic reaction, the metallic dendrites would occupy more than 85 vol% of the alloy. Consequently, the eutectic liquid at the conclusion of solidification forms very thin films or even isolated droplets. However, during the medium stage of solidification the residual melt in between the dendrites may be sucked away to feed solidification shrinkage elsewhere. To filter the liquid through network of solid dendrites, a competition between various pressure terms exists [212]. The pressure drop in the channels and pressure against surface tension of solid-liquid are required to overcome to drive the flow. The necessary pressure is believed to be provided by metallostatic head pressure, atmospheric pressure, gravity and volume shrinkage which pulls the liquid inside the channels. Nevertheless, the flow is more difficult through narrower channels and it may be entrapped and solidifies in constricted channels prior to decanting.

[2] Partially reprinted from Journal of Materials Letters, Vol. 88, S. Amini and R. Abbaschian, ″Synthesis of curved graphene layers on metallic dendrites″, pp 129-131, Copyright © 2012, with permission from Elsevier.

Fig. 60(b) shows two channels in which liquid has been decanted thoroughly and entrapped. It is estimated visually that the melt did not flow through micro channels of less than 10 μm [Fig. 60(b)].

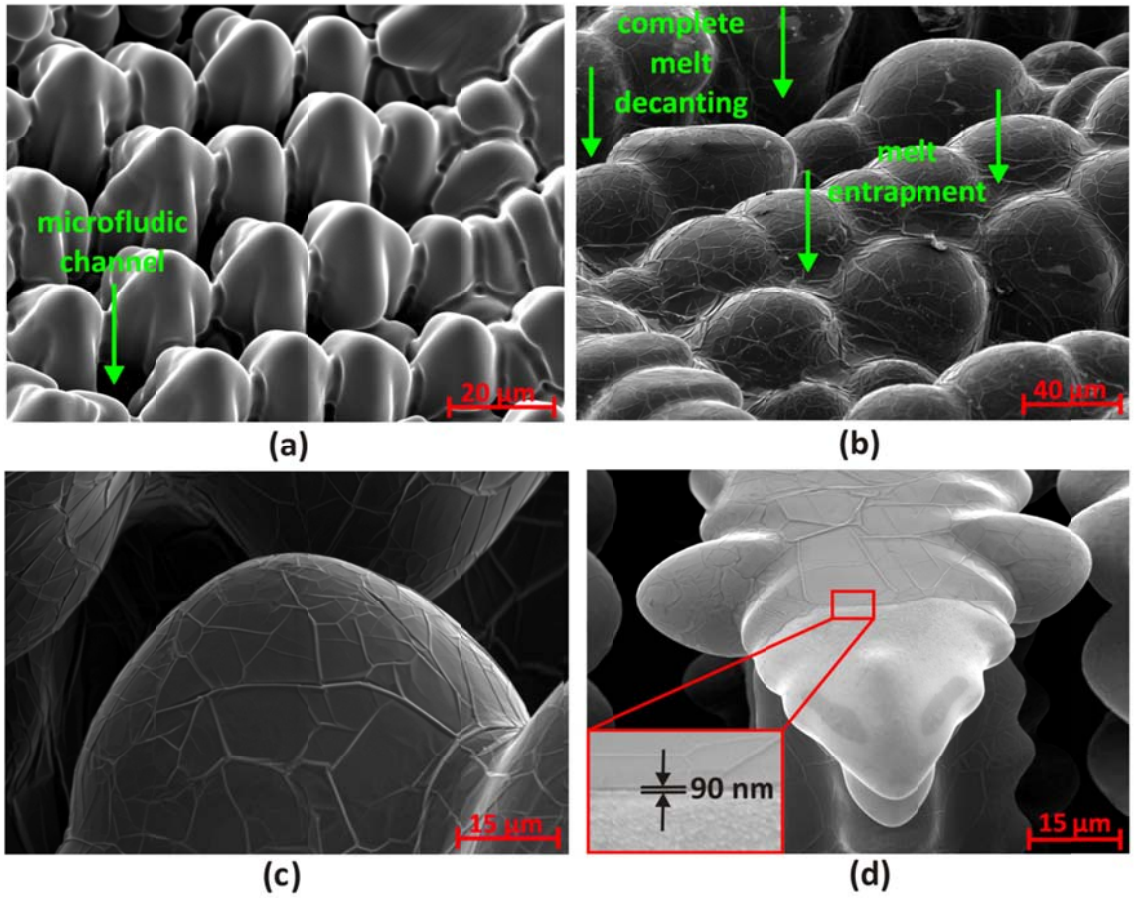

Fig. 60 a) bare nickel-copper dendrites tip grown from the melt b) melt decanting and entrapment in microfluidic channels due to different channel size c) curved graphene layers on the nickel-copper dendrite d) nickel-aluminum dendrites partially covered by 90 nm-thick graphene layers

As the wetting liquid solidifies, the metal atoms inside the residual melt continue to grow on the dendrites arms while the carbon atoms are rejected and form graphene shells enclosing and conforming to the curved surface of dendrites. The schematic of the processing technique for growth of curved graphene layers has been shown in Fig. 61.

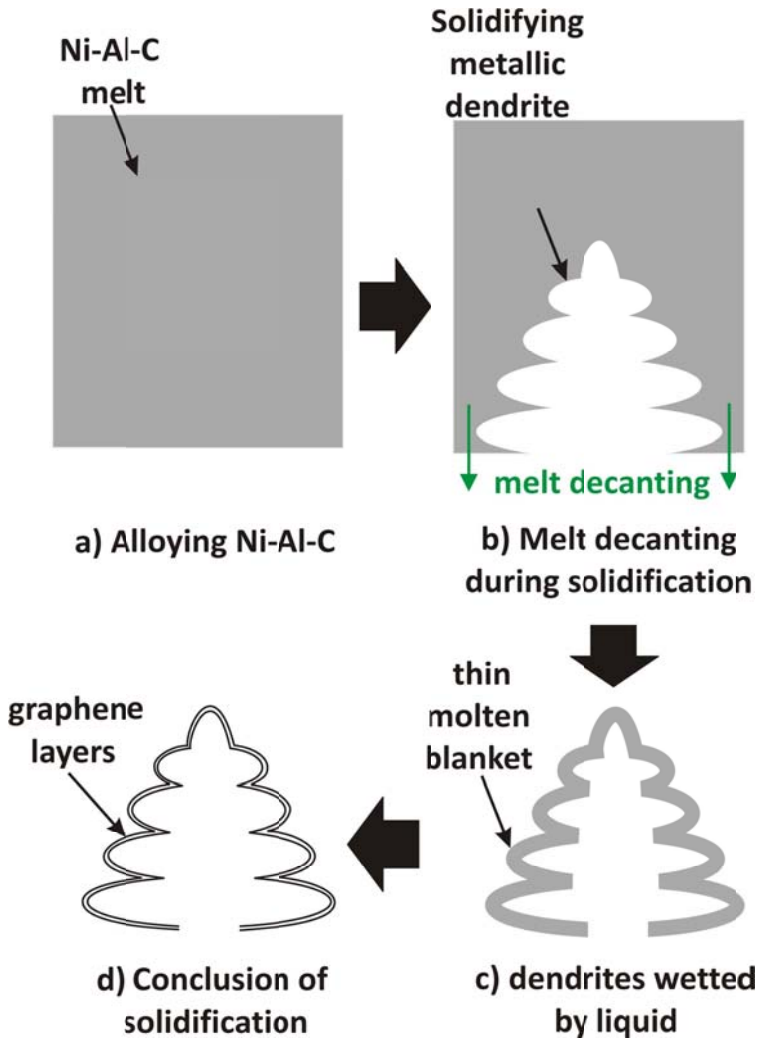

Fig. 61. Schematic of the processing technique for growth of curved graphene layers

Fig. 60(c) shows the curved graphene films with approximately 20 μm radius of curvature which has been grown on a dendrite arm. The films thickness can be visually observed in locations where there was a partial coverage by graphene layer spallation.

Fig. 60(d) shows a dendrite stem in between two channels in which the graphene films did not cover the substrate completely. The thickness of the films was determined to be around 90 nm. Detailed micro-Raman spectroscopy precisely revealed that the thickness of the layers varies from thick graphite layers to a few layer graphene. Fig. 62 shows the Raman spectrum of curved layers on Ni-Cu dendrites along with the 2D band deconvolution. The spectrum is similar to those reported for a few layer graphene [189]. The missing D and D´ bands in the spectrum as well as asymmetry of 2D band reveals the high quality and ABAB Bernard stacking of graphene layers.

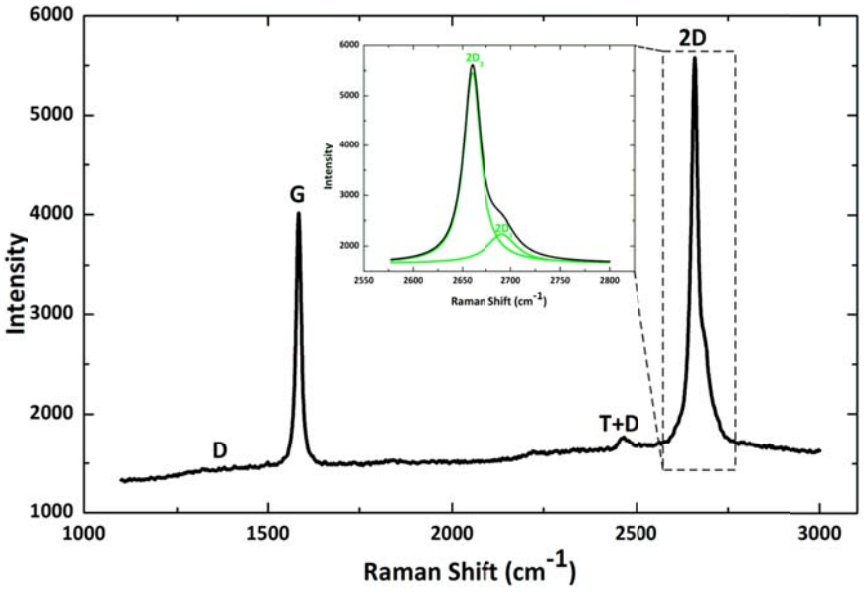

Fig. 62. Raman spectrum of curved a few layer graphene film on Ni-Cu dendrite along with the Lorentzian deconvolution of 2D band

Following the graphene films formation both dendrites and graphene films contract as they cool down in solid states and due to the different thermal expansion coefficients a network of wrinkles forms in graphene layers (section 0). The schematic of wrinkles formation on dendrites has been shown in Fig. 63(a). Owing to geometry, the wrinkling phenomenon is intense on concave regions between dendrite arms. This could be observed in Fig. 63(b) which shows a highly wrinkled area in between dendrites. It should be noted that since the graphene layers are highly resilient, they maintain their continuity and crystallinity over the wrinkles through deformation mechanisms of kinking or twining. This was confirmed by the similarity of Raman spectra of flat regions and faceted wrinkles and observation of no defect bands in Fig. 52(c).

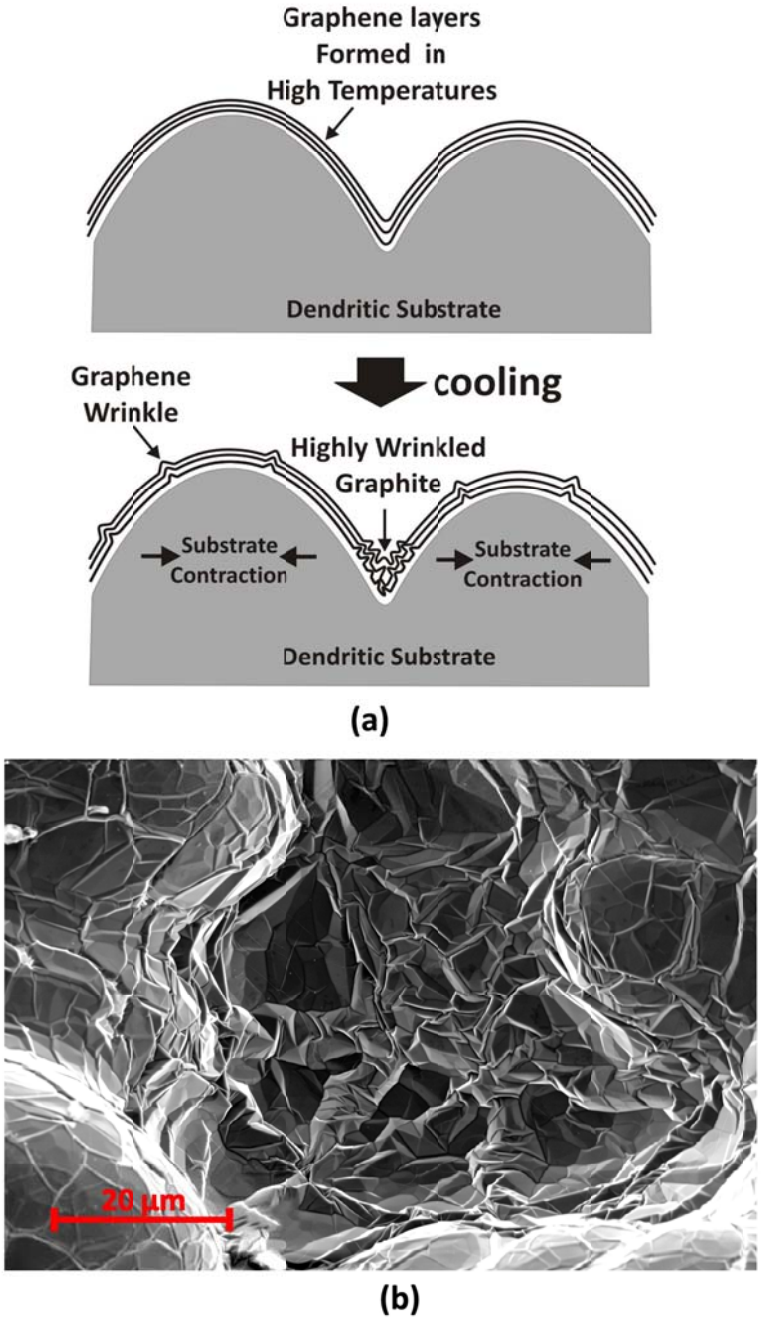

Fig. 63. a) Wrinkles formation on dendritic substrate b) highly wrinkled graphene layers on dendrites

Chapter IV

Graphite crystals grown within metal-carbon melt[3]

[3] Partially reprinted from Journal of Acta Materialia, Vol. 60, S. Amini, H. Kalaantari, S. Mojgani and R. Abbaschian, ″Graphite crystals grown within electromagnetically levitated metallic droplets″, pp 7123-7131, Copyright © 2012, with permission from Elsevier.

It was shown in chapter I that upon cooing of supersaturated melts graphene layers grow on the surface of the melt. It should be noted that graphene layers also grow in the bulk with various morphologies. In this chapter, nickel and carbon system was utilized to investigate different morphologies of graphite grown within a metal-carbon melt. The containerless melting process of electromagnetic levitation has been utilized for heating and cooling of supersaturated melts to eliminate the effect of crucible wall during solidification. It is shown that melt composition, cooling rate and the mixing of the melt by electromagnetic forces affect the microstructure and the subsequent graphite morphologies. Graphite crystals grow in this system including graphite flakes, spheres, entrapped and engulfed agglomerated particles, curved surface graphite and eutectic flakes are discussed.

4.1. Cooling curves of the melt

The Ni-C phase diagram consists of a simple eutectic reaction at 1326 °C and 1.9wt%C along with a limited solid solubility of carbon in nickel [Fig. 48(b)].

Fig. 64 shows typical cooling curves during solidification of hypo (Ni+1.8wt%C) and hypereutectic (Ni+3.0wt%C) alloys within the levitation coil. In hypereutectic melts, as the melt cools down from 1800°C, a recalescence is observed around 1710°C which raised the temperature to about 1730°C (ΔT=20°C). As will be discussed later, the maximum recalescence temperature (1730°C) corresponds to graphite liquidus (T_{gr}). Subsequent to this recalescence, the cooling rate increased abruptly until the melt reached the temperature of about 1500°C. Another slope change occurs near the end of

solidification around 1235°C which corresponds to nucleation of nickel (T_{Ni}). In hypoeutectic melts on the other hand only one slope change is observed around 1250°C. These slope changes are related to the formations of graphite and nickel and will be discussed later. To investigate the effect of cooling rates, the hypereutectic alloys were cooled with the rates of 3, 7, 13, 40 and 55 K/s. Effect of cooling rate will be discussed later in chapter V.

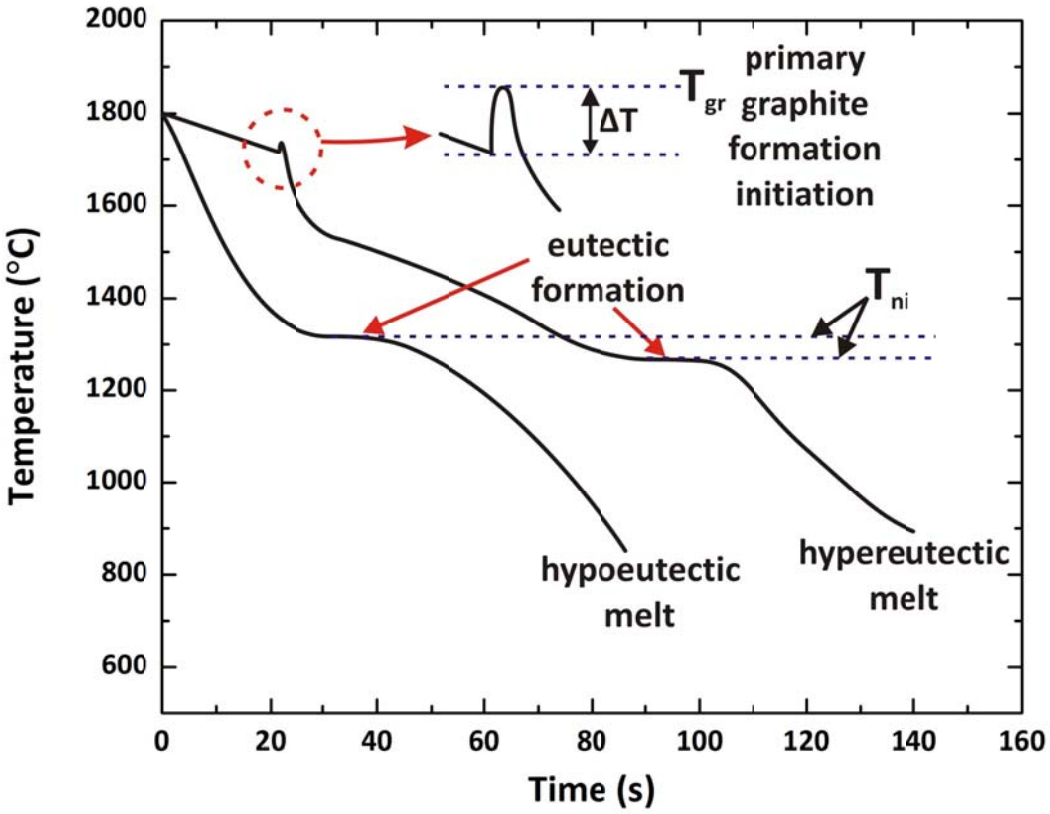

Fig. 64. Typical cooling curves of hypo and hypereutectic Ni-C melt

4.2. Microstructures

Fig. 65 shows structure of a hypoeutectic alloy solidified within the levitation coil. The microstructure in Fig. 65(a) is uniform and it contains graphite particles engulfed in nickel matrix or embedded in between the nickel dendrites [Fig. 65(b)]. Fig. 66 shows microstructure of hypereutectic alloys which has been solidified within the levitation coil. It is observed in Fig. 66(a) that the graphite morphologies are not uniform and in the center and close to the surface are dissimilar. The two distinct regions in the center and at the periphery have been separated by a dashed line marked as boundary in Fig. 66(b). The microstructure near the center is similar to hypoeutectic structure of Fig. 65(b), i.e. graphite morphology is agglomerated particles. Close to the surface of the samples, however, relatively large primary graphite flakes and spheres are observed [Fig. 66(b)]. Flakes have few hundred micron length and a few tens of micron width and possess coarse forms and smooth surfaces. This form of the graphite flake is the so-called Kish graphite (or type C) shown in Fig. 5. The primary flakes and spheres are surrounded by a very fine form of eutectic flakes which is observed in magnified view of Fig. 66(c). This graphite morphology is the so called type D (Fig. 5) which grows side by side with nickel during a coupled growth mechanism [8, 31, 213].

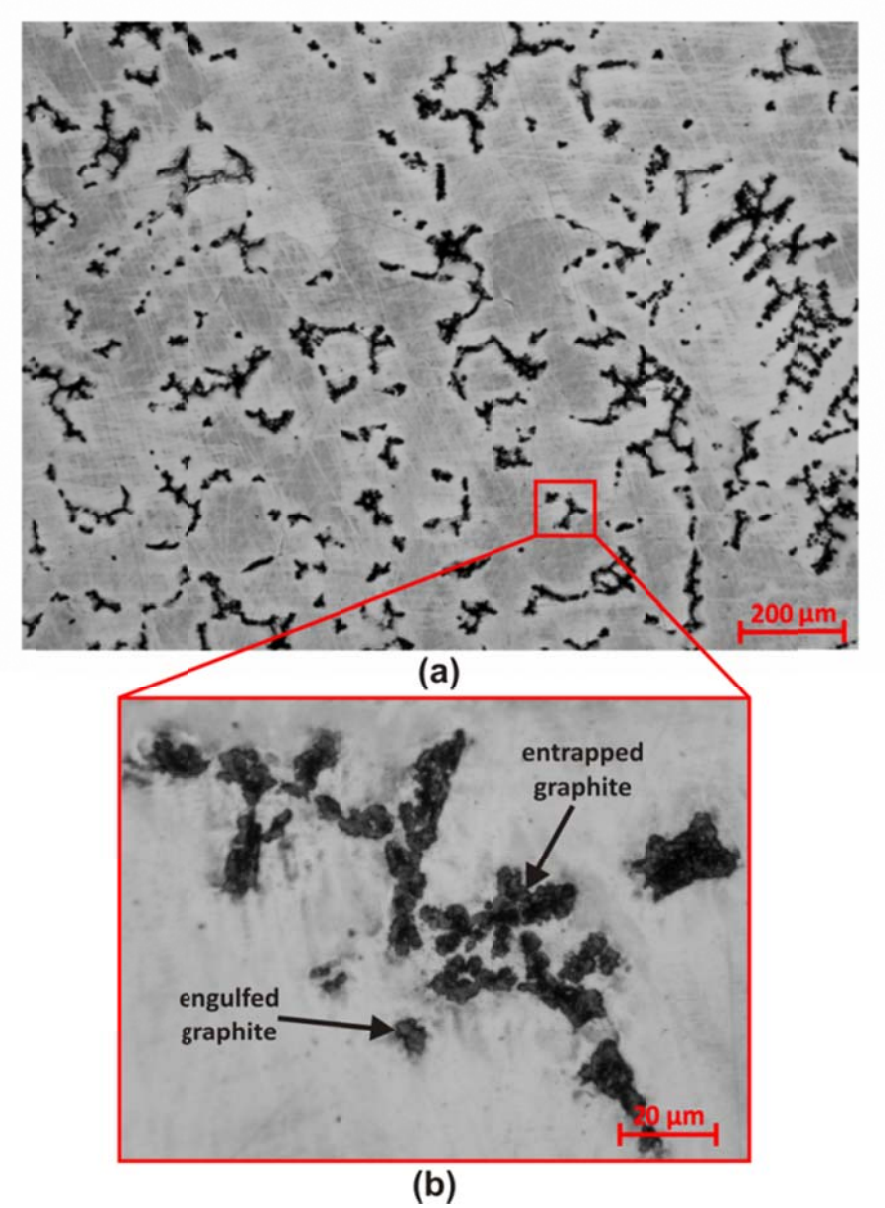

Fig. 65. a) Microstructure of a hypoeutectic melt solidified in levitation b) magnified view of engulfed and entrapped graphite particles

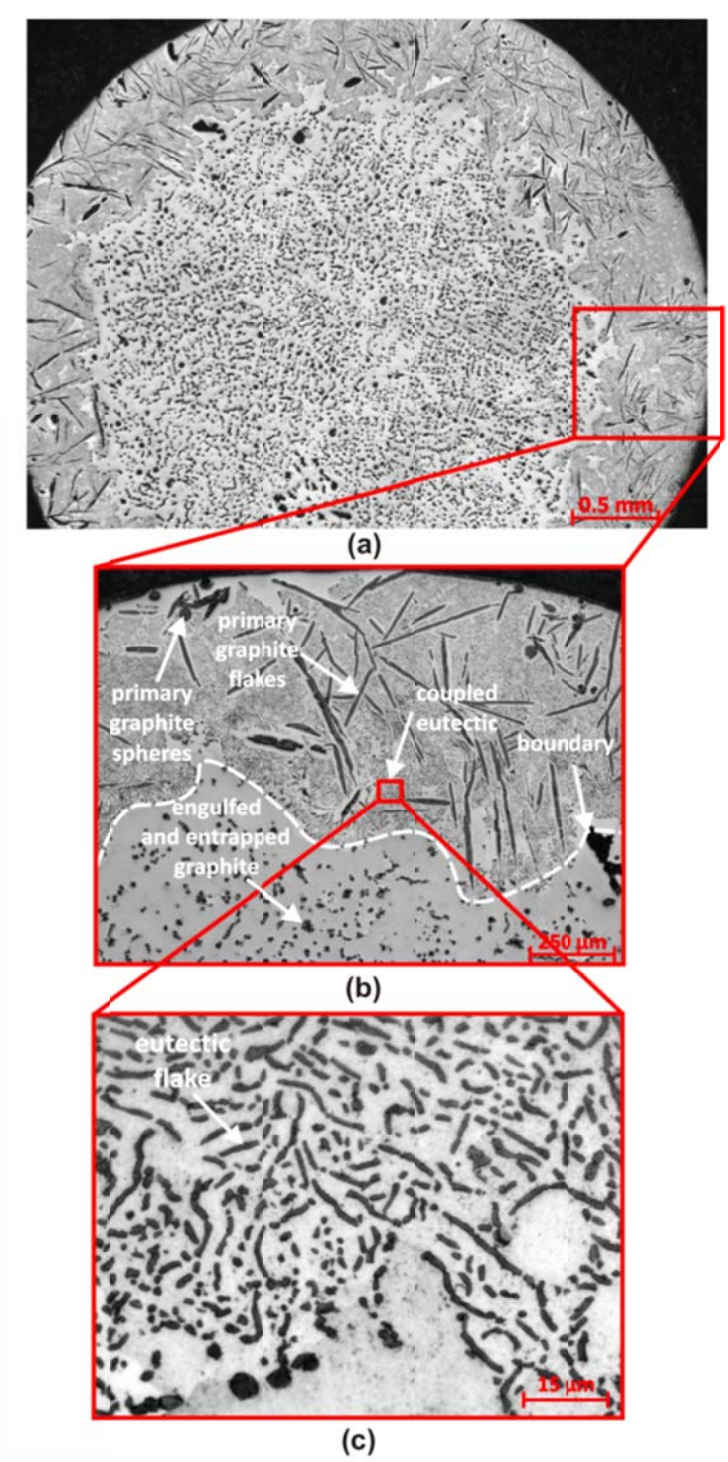

Fig. 66. Microstructures of a hypereutectic melt solidified within the levitation coil

The non-uniformity of microstructure is attributed to mixing of the melt caused by EM currents and will be discussed later in section 4.3.

4.3. Primary graphite morphologies

When the hypereutectic melt is cooled down, the primary graphite flakes and spheres start forming as the melt intersects the graphite liquidus. The necessary undercooling for the initial nucleation of graphite can be understood from the cooling curve. In the cooling rates of 3 and 7 an undercooling of around 20°C was observed on the cooling curve of

Fig. 64. Nevertheless, in the higher cooling rates (i.e. more flow of He gas) this is not observable due to slow response of the pyrometer. Therefore, it is conceivable that $\Delta T \approx 20°C$ is driving the initial graphite nucleation. As the primary graphite form inside the melt, it can also form on the surface of the liquid droplet. The formation or accumulation of surface graphite will cause a sudden drop of temperature in the cooling curve of Fig. 64. As the melt is continuously cooled down nickel begin to nucleate. The plateau in cooling curve of Fig. 64 shows that Ni is often nucleated 90 °C below eutectic in 1235 °C. The solidification will be concluded with the formation of nickel-graphite eutectic [Fig. 66(c)].

Upon cooling of hypereutectic alloys, the primary graphite flakes and spheres form as the melt intersects with the graphite liquidus temperature in phase diagram. The graphite nucleation causes the first recalescence in cooling curve of hypereutectic melt in Fig. 64. Non-uniformity of hypereutectic microstructure in Fig. 66 is owing to circulation of the

melt during solidification [185, 214, 215]. Because of mixing while primary graphite crystals are growing, they accumulate at the surface of the melt due to shear during flow. This can be observed schematically in Fig. 67. As the primary graphites grow larger, they become interlocked and the entire solid-liquid region rotates as a semisolid crust. This could be understood by analogy with the flow of water under the leaves in a pond. Upon more cooling and reaching the eutectic composition, the liquid in between the graphite flakes and spheres next to the surface solidifies as coupled eutectic while the liquid in the center formed a divorced eutectic of nickel and agglomerated graphite particles. The formation of these two forms of eutectic will be discussed in more details in sections 4.4.1 and 4.4.2.

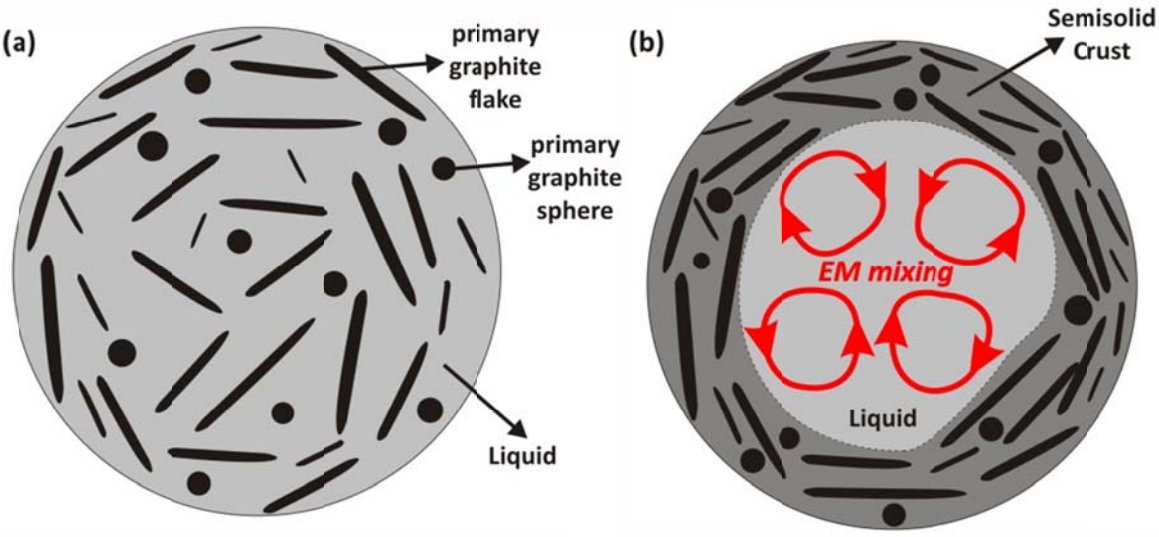

Fig. 67. Primary graphite flakes and spheres in a hypereutectic of Ni-C when there is (a) no EM mixing (b) EM mixing

4.3.1. Graphite flakes

Fig. 68 shows the morphology of a primary flake which was deeply etched and filtered. The flakes have a plate-like morphology where the expanded face and the tip are the basal and prismatic planes respectively.

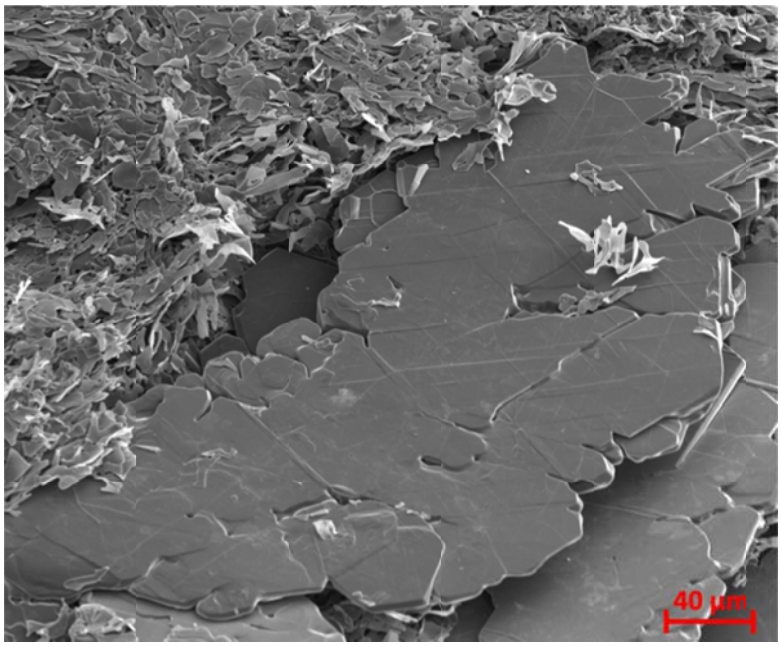

Fig. 68. Morphology of a primary graphite flake

The geometry of the flakes reveals the higher growth rates of prismatic planes than the basal plane. The growth rate of graphite interfaces will be discussed extensively and modeled in section 5.3.3. Just to mention briefly, it is conceivable that in current cooling rates (3-55 K/s) the basal plane is faceted and grows by 2D nucleation and migration of ledges or spiral growth. Fig. 69(a) and (b) show the evidence of ledge-assisted and spiral growth on the graphite interfaces which have been marked by red arrows. The prismatic planes at the flakes tip, however, are rough and grow faster by a diffusion controlled

mechanism. The different growth rates of graphite interfaces results in elongation of graphite crystals in the tip and formation of plate-like morphology.

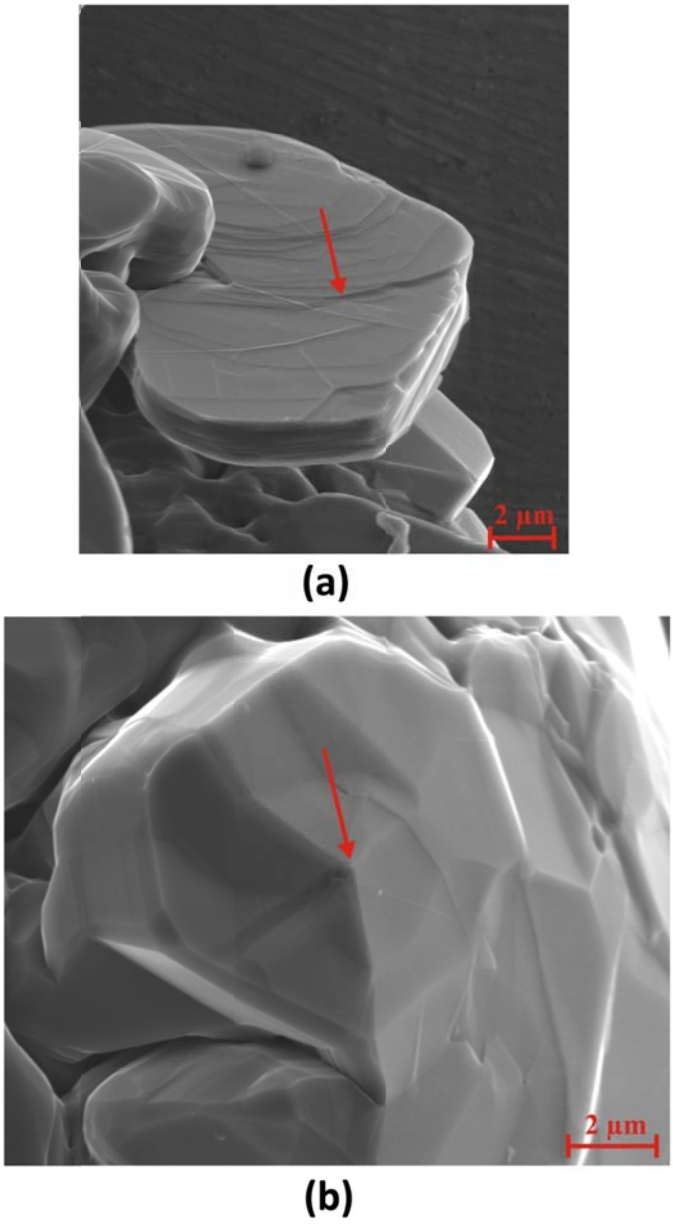

Fig. 69. Evidence of graphite growth in basal plane by a) 2D nucleation and migration of ledges and b) Spiral growth

4.3.2. Graphite spheres

Fig. 70(a) shows the morphology of a graphite sphere which has been extracted from its metallic matrix and transferred to an arbitrary substrate. The SEM photo depicts that the sphere is a poly crystal including some pillars which have been grown radially from the core. The pillars are evidently the stacks of graphene layers grown normal to graphite basal plane. Although Fig. 70(a) reveals the outer morphology of spheres, it will not provide information about the core morphology. The inner morphology of spheres, however, could be observed in the spheres which have grown partially. Fig. 70(b) shows two partially grown graphite spheres next to each other. The core structure consists of graphene layers which have grown circumferentially and covered the crystal similar to leaves of a cabbage. Detailed microscopy of graphite spheres which either grew partially or their growth has stopped in early stages revealed that graphite spheres structure evolves during multiple growth stages.

It is believed that upon formation of graphite nucleus, due to ample availability of carbon atoms in the vicinity of the nucleus, the growth driving force is high and graphite interfaces grow in *a* and *c* direction with the similar speed. This is the initial stage of the growth which has been shown in schematic view of Fig. 70(c) as stack of graphene layers. As the growth proceeds, it may slow down and cause the formation of some curved facets which conform to crystal. Introduction of defects into the fast growing crystal may assist the bending mechanism. As these facets are growing, new ones will also nucleate which provide necessary ledges for lateral growth. As it is shown

schematically in Fig. 70(c), the formation of curved facets at the second stage of the growth brings about a structure similar to cabbage leaves.

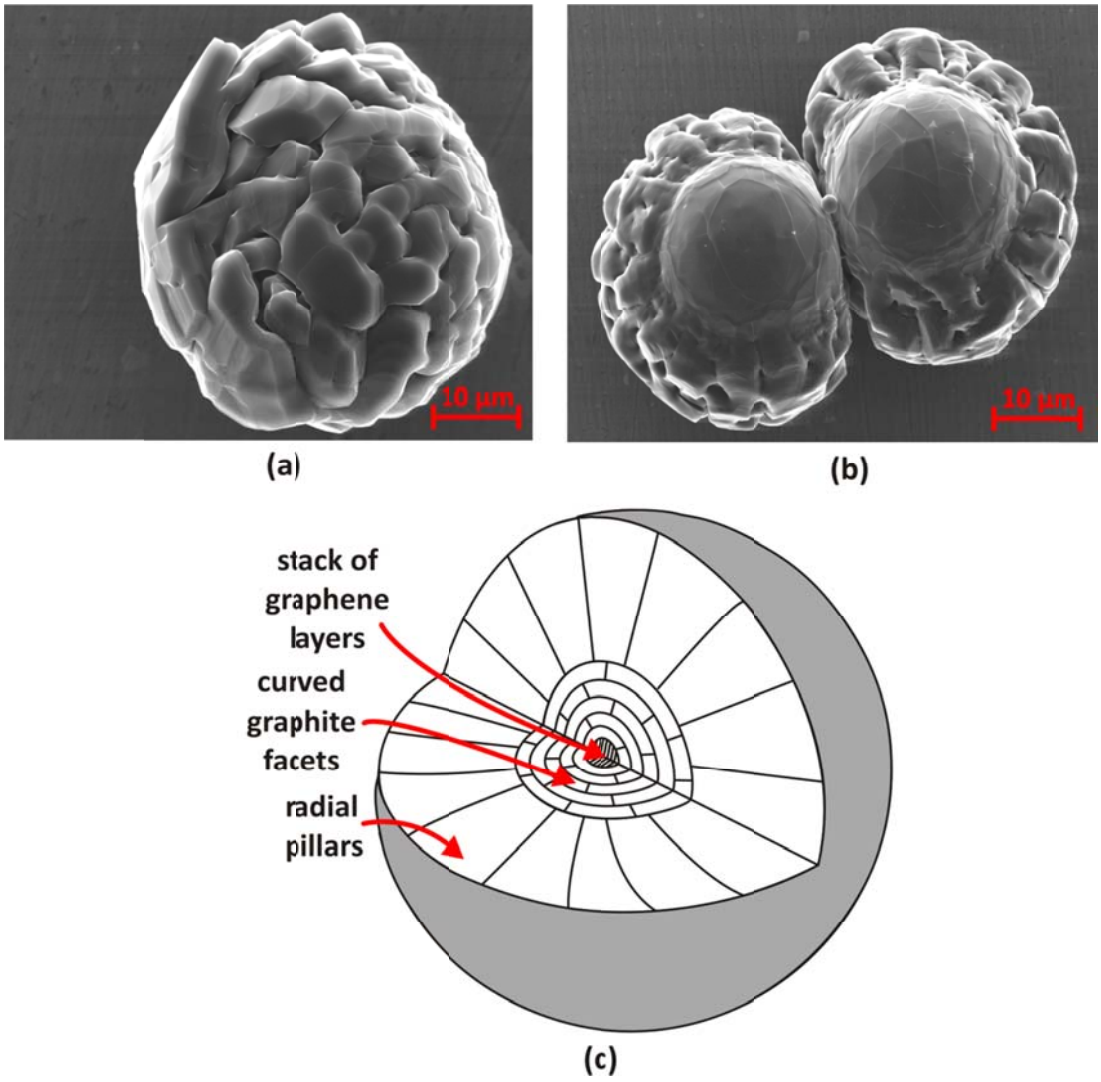

Fig. 70. a) Morphology of a graphite sphere b) morphology of partially grown graphite spheres c) schematic structure of a sectioned graphite sphere

Finally, due to further consumption of carbon atoms in the vicinity of growing sphere driving force decreases even more and causes the radial formation of graphite pillars on the existing crystal. These filaments could be observed in structure of spheres in Fig. 70. Eventually the formation of a nickel envelope around the growing sphere will disconnect it from the melt and bring the growth to an end.

4.3.3. Curved surface graphite

As it was discussed in section 3.1, the surface of molten metal is a suitable site for heterogeneous nucleation and growth of graphite. Upon cooling, the primary surface graphite will grow at the droplet surface. Fig. 71 shows the time elapsed frames of graphite growth in the surface of the melt which has been recorded by a portable microscope.

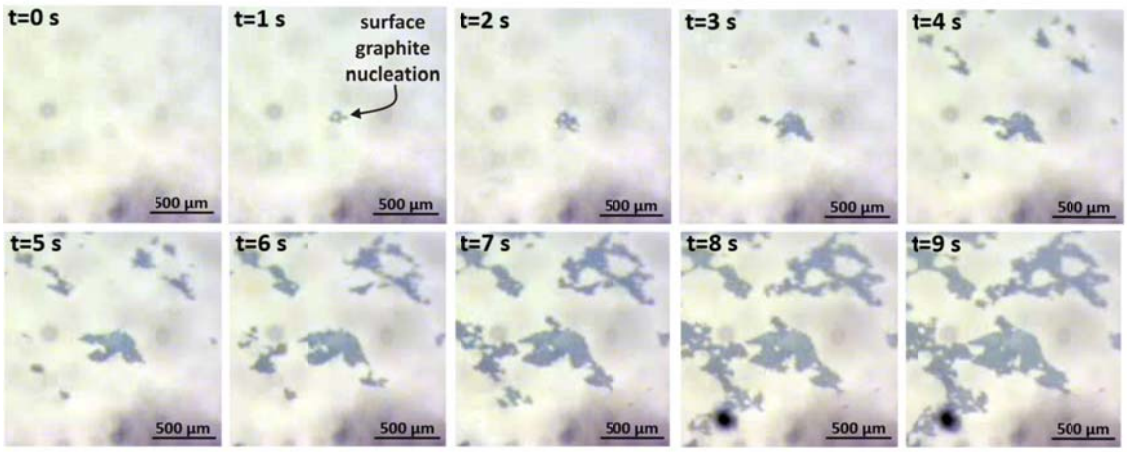

Fig. 71.Time elapsed frames of graphite growth in the surface of the melt

Upon cooling from high temperatures, as the melt intersects with the graphite liquidus temperature, the first nucleation event may occur on the surface (t=1 s in Fig. 71). The nucleated island grows diffusely and smoothly in the tip and basal planes respectively. As the cooling continues, other nucleation events occur (t=3 s in Fig. 71). Newly formed nuclei then grow until they cover the entire surface. The in-plane covalent bonds of carbon atoms in graphene lattice assist the graphite crystal to bend and cover the entire surface without losing their crystalline network. The sudden drop of temperature upon the formation of primary graphite in

Fig. 64 is due to the formation of surface graphite and the fact that it blocks thermal radiation of the melt. Fig. 72 shows the deeply etched surface graphite which had already covered the interior metal-graphite composite.

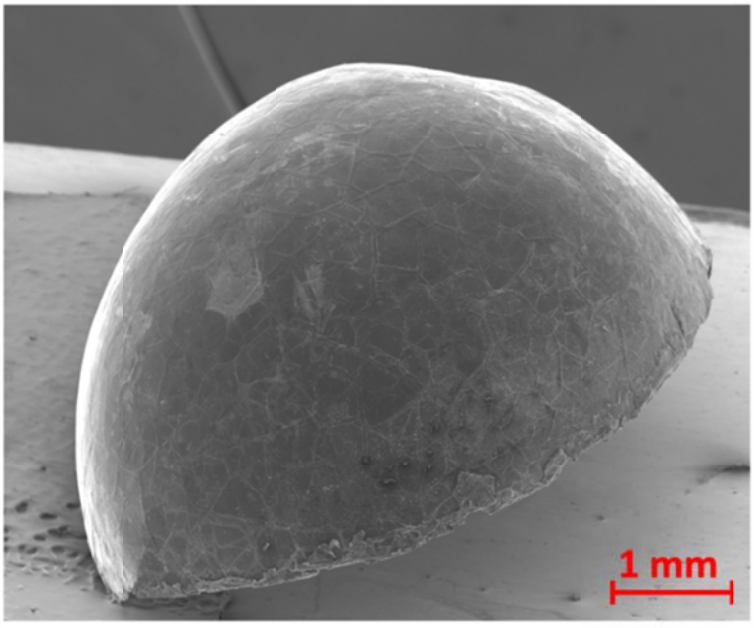

Fig. 72. Curved surface graphite morphology

4.4. Graphite formed in eutectic

4.4.1. Divorced particles

When a hypoeutectic melt is cooled within levitation coil, it is constantly rotating due to EM current. During the cooling of a hypoeutectic alloy of Ni-C, nickel is the first phase which nucleates around 1235 °C in

Fig. 64. The nickel grains are initially small and are constantly mixing with liquid. As the grains become larger, their growth becomes dendritic and the EM current may break these dendrites and mix the solid and liquid. During the interface growth, the solid will take nickel and reject carbon into the liquid. As the liquid is continuously cooled down, parts of it might locally get to eutectic composition and the graphite then starts to nucleate. The formed graphite nuclei are stirred and mixed along with nickel dendrites and meanwhile get coarsened. While the nickel dendrites are not interlocked, the formed graphite particles are not entrapped in between the advancing nickel grains and mixed along with nickel. The nickel grains eventually become so large that they cannot mix anymore. For that reason the liquid would be entrapped in between the nickel boundaries. At this time, according to phase diagram nickel occupies relatively high volume fraction of the structure and the melt are just confined to tiny droplets in between the dendrites. Since the graphite nucleation inside these tiny pools are difficult and needs high undercoolings, the nickel dendrites continue to grow and engulf or entrap the prevailing graphite particles. Since nickel and graphite grow separately, they form the so-called

divorced eutectic [216]. In Fig. 73 deeply etched graphite particles morphologies have been shown.

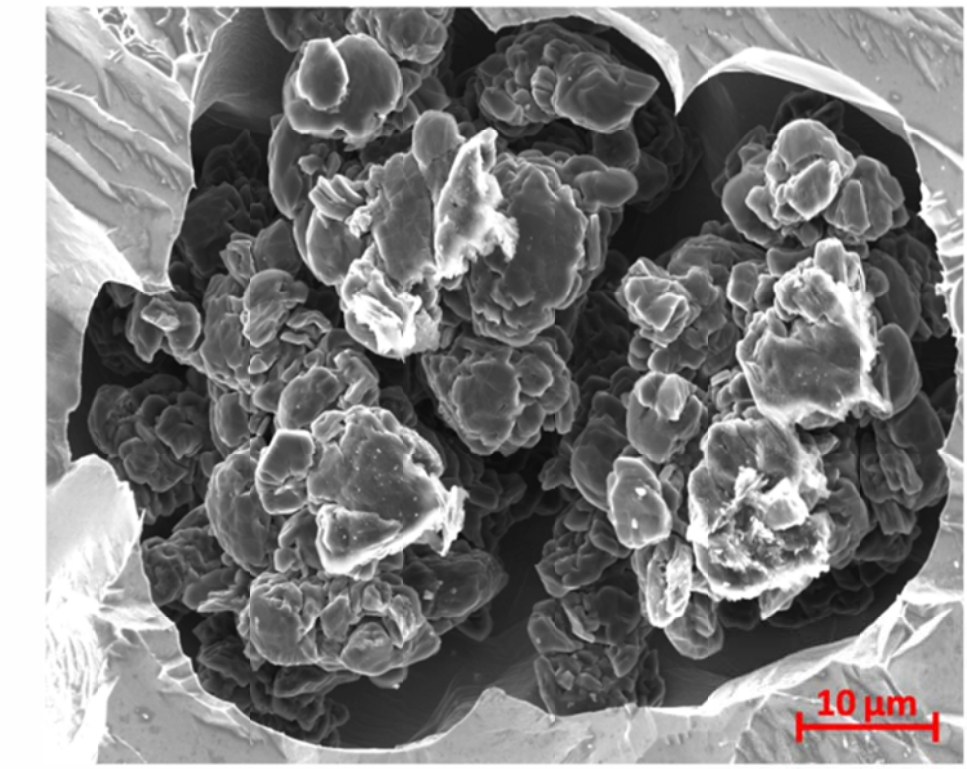

Fig. 73. Graphite particles morphology in deeply etched hypoeutectic alloy

In order to better understand the effect of dynamic cooling and mixing, in ???? the microstructure of hypoeutectic melt Ni-C melt which has been solidified statically within a BN crucible has been shown in Fig. 74.

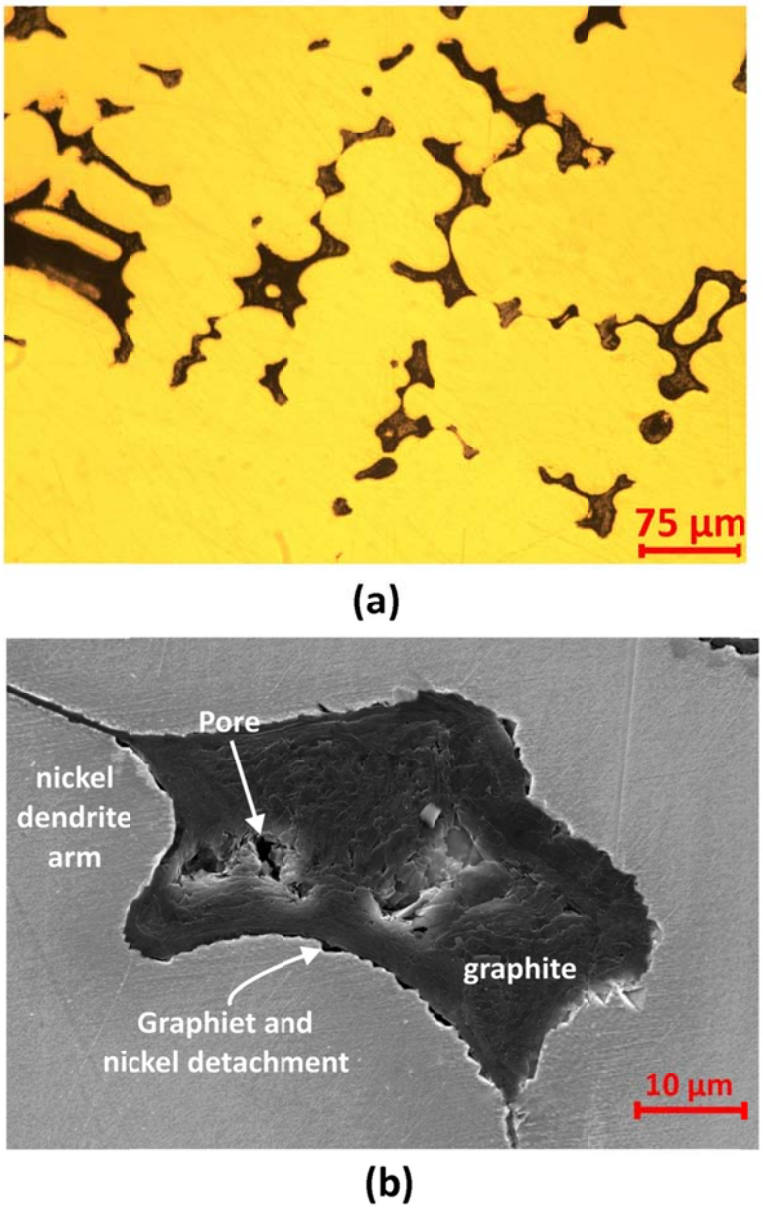

Fig. 74. a) Microstructure of a hypoeutectic Ni-C melt solidified statically within BN crucible b) morphology of a graphite formed in between nickel dendrite in static cooling

In the case of static cooling in Fig. 74, since there is no mixing, while the nickel dendrite is growing, they reject carbon and the liquid become richer in carbon and closer to eutectic composition. While the liquid reached the eutectic composition based on the Ni-C phase diagram and applying the lever rule, it is only confined into tiny pools in between the nickel dendrites. While the nucleation of graphite in these tiny droplets is difficult, the nickel dendrites continue to grow. The graphite particles eventually nucleate and grow separately in a divorced manner in between the dendrites and get the morphology of the Fig. 74(b). Different thermal expansion coefficient of nickel and graphite during further cooling may cause the detachment of graphite and nickel in some regions as it has been shown in Fig. 74(b). Comparing the graphite morphologies in Fig. 73 and Fig. 74 shows that while the graphite morphology in dynamic cooling of hypoeutectic alloys is agglomerated particles, graphite forms a solid particle during the static cooling which its shape is dictated by available interdendritic spaces.

4.4.2. Eutectic flakes

Since graphite and nickel are faceted and non-faceted crystals respectively, the coupled zone region of this system is skewed toward graphite, beneath the eutectic point [217, 218]. The coupled region has been shown as a grey area in the phase diagram of Fig. 75 which has been extracted from the work of Scheil [219]. The eutectic morphology at the periphery of the alloy in Fig. 66 indicates that this portion of the sample grew within the Ni-C coupled zone which is defined as the range of melt composition and growth velocities or temperatures for which the coupled growth leads the growth front.

In phase diagram of Fig. 75 the solidification path of a hypereutectic melt cooled from temperature higher than graphite liquidus has been sketched. As it was explained previously during melt cooling, primary graphites start to form which will consumes the carbon atoms and shift the melt composition toward the nickel side in the phase diagram. Therefore, as the liquid reaches the necessary undercooling for formation of nickel (1235 °C in cooling curve of

Fig. 64), its composition is outside the coupled zone. This can be observed in phase diagram of Fig. 75. Solidification then begins with formation of primary nickel dendrites. Since the liquid is below T_0 line, the formation of nickel dendrites from liquid is initially partitionless. While nickel dendrites nucleate and grow inside the supercooled liquid, a recalescence takes place which raises the liquid temperature above the T_0 line where the melt partitioning will occur. At this temperature as nickel dendrites grow with a composition given by metastable extension of nickel solidus line, the carbon atoms are rejected into liquid. Carbon rejection will cause a compositional shift of the remaining liquid toward higher carbon content. At some temperature, the liquid composition and temperature cross into the Ni-C coupled zone. At this time nickel and graphite grow side by side and form a coupled eutectic.

Fig. 76 shows SEM photo of eutectic graphite flakes which are deeply etched and filtered. The morphology shows that eutectic flakes frequently branch in the plane of the sheets. Possible mechanisms producing this branching with orientation change are twinning and tilting [49].

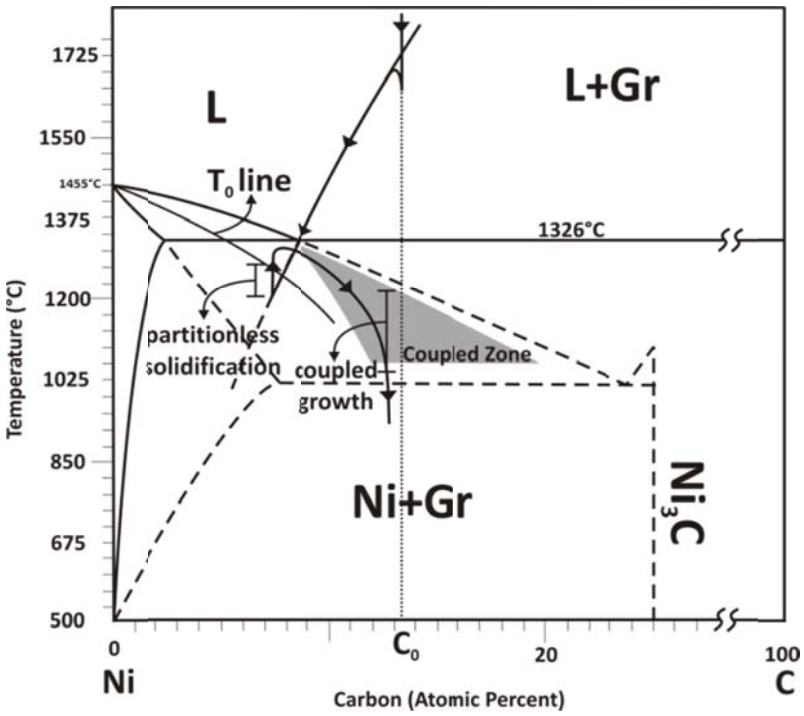

Fig. 75. Solidification path of a hypereutectic alloy (C_0: initial carbon molar fraction of the melt)

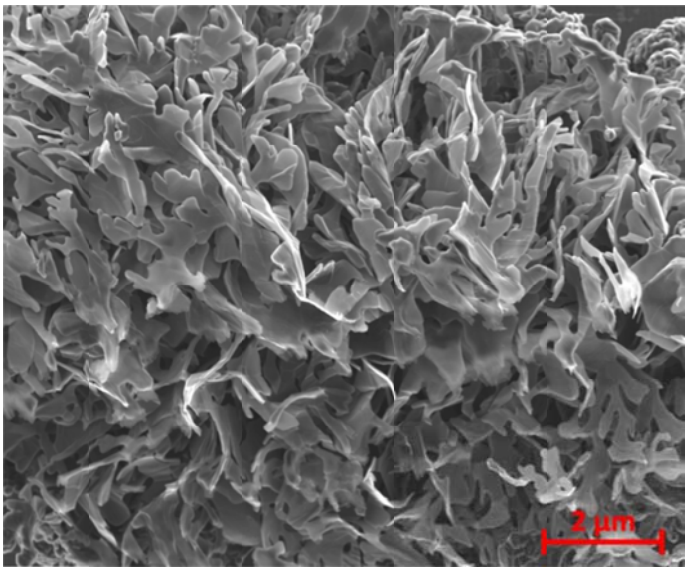

Fig. 76. Eutectic flakes morphology

Fig. 77 shows discussed morphologies of graphite including primary flakes, spheres and eutectic flakes which gathered and formed a graphitic orchid.

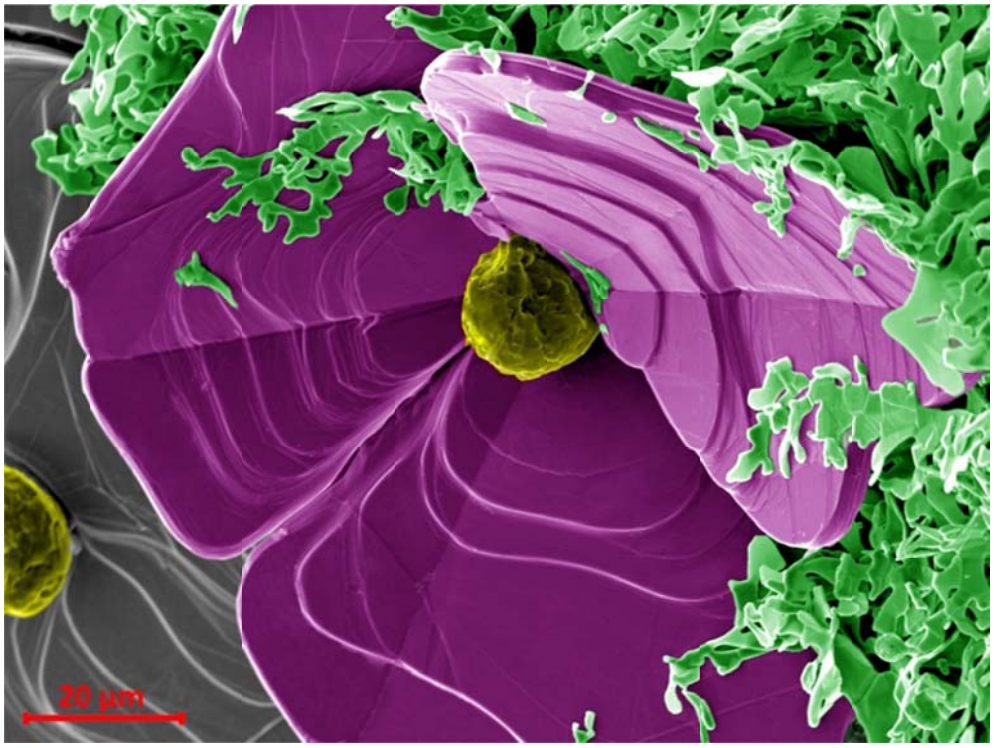

Fig. 77. A graphitic orchid formed by various graphite crystals including primary flakes (purple) , spheres (yellow) and eutectic flakes (green) (the picture has been colored in Photoshop)

Chapter V

Nucleation and growth kinetics of graphene layers[4]

[4] Partially reprinted from Journal of Carbon, Vol. 51, S. Amini and R. Abbaschian, ″Nucleation and Growth Kinetics of Graphene Layers from a Molten Phase″, pp 110-123, Copyright © 2013, with permission from Elsevier.

In this chapter, nucleation and growth kinetics of graphene layers have been investigated in Ni-C system. For this purpose, graphite flakes and spheres which were grown inside molten nickel at different cooling rates (chapter IV) are investigated in more detail. From the geometry of the flakes, their growth rates in the basal and prismatic planes are obtained. A physical model which treats the growth kinetics is then presented and compared to experimental results. Moreover, the morphologies of the grown spheres were examined with detailed microscopy techniques and their multi stage growth mechanism is explained. Finally effect of cooling rates on flake to sphere morphology change kinetics is described.

5.1. Effect of cooling rates on grown morphologies of graphite

Fig. 78(a)-(f) show microstructures of hypereutectic Ni-C melts which have been electromagnetically levitated and then solidified within the coil or quench in the oil. The non-uniformity of the samples and the formed various graphite morphologies were explained previously in chapter IV. However, it is visually observable in Fig. 78 (a)-(e) that as the cooling rates increase the graphite flakes become finer. Moreover, increasing the cooling rates favor the formation of graphite spheres. This is better observable at extremely high cooling rate where the microstructure in quenched samples is fully spherical in Fig. 78(f).

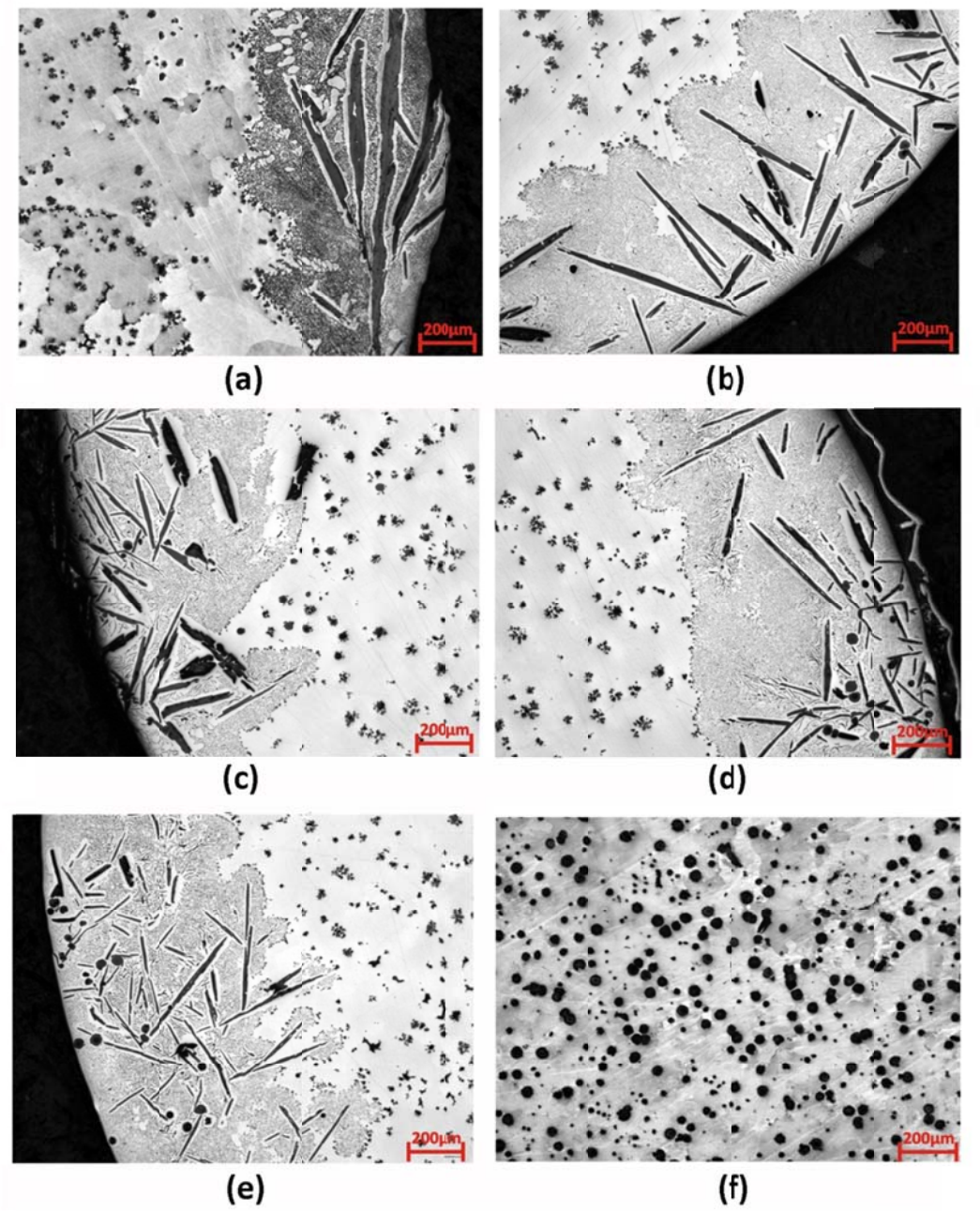

Fig. 78. Grown graphite morphologies Ni-C melts during different cooling rates a) 3 K/s b) 7 K/s c) 13 K/s d) 40 K/a e) 55 K/s and f) quenched in oil

5.2. Geometrical analysis of primary graphite

The graphite flakes were quantitatively analyzed by their width and length sizes while the graphite spheres were characterized by their diameter size. In the polished samples it is pertinent to point out that the flakes and spheres dimensions are not the same as they appear in cross section. This is due to the fact that the flakes may be cut in various directions which change the observed length and width in 2D cross section. Thus, a small flake appearing on a 2D microstructure may be just the edge of a larger one which is partially cut. Furthermore, cross sectioning of a sphere above and below the diametral section will show smaller diameter. Fig. 79(a) and (b) shows the flakes aspect ratio and spheres diameter percentile in different cooling rates respectively. Flakes or spheres do not possess uniform size and a size distribution prevails. As an approximation, the averages of five longest flakes and ten largest spheres geometries in each cross section are considered as the geometry of primary graphites in that sample. Table 1 shows the geometrical analysis of the formed primary flakes and spheres in cross section of the samples along with the averages of five longest flakes and ten largest spheres.

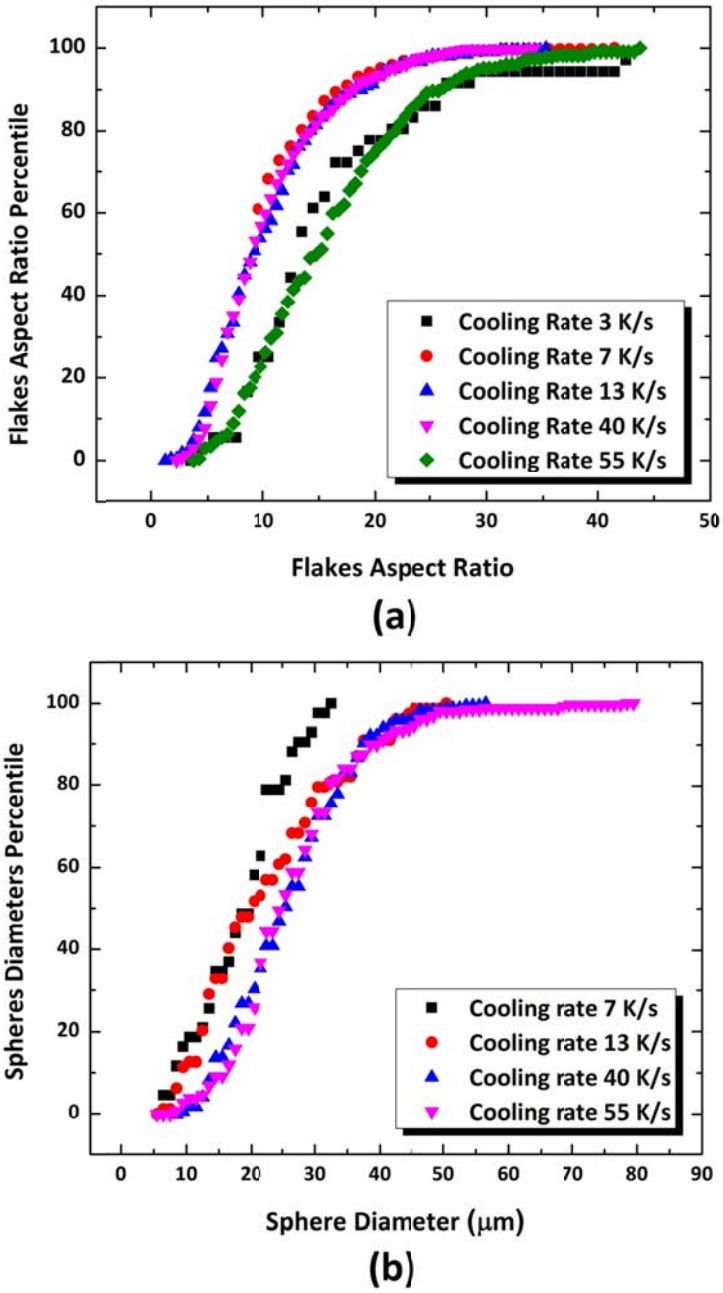

Fig. 79. a) Flakes aspect ratio and b) sphere diameters size percentile in different cooling rate

Table 1. Geometrical analysis of primary graphites in ~40 mm^2 of area

Sample	CR (K/s)	Flakes							Spheres			
		Count	10% of longest flakes (µm)			5 longest flakes			Count	Ave. D (µm)	Ave. D for ten largest (µm)	Max D. (µm)
			Ave. L (µm)	Ave. W (µm)	Ave. AR	Ave. L (µm	Ave. W (µm)	Ave. AR				
Ni+3.0 wt%C	3	36	1025.9	69.6	14.7	918.0	60.7	15.1	0	-	-	-
Ni+3.0 wt%C	7	379	486.3	31.0	15.7	679.2	37.3	18.2	47	18.5	27.3	32.0
Ni+3.0 wt%C	13	222	536.0	33.2	16.14	659.2	32.5	20.2	73	22.2	42.2	62.7
Ni+3.0 wt%C	40	435	382.6	22.9	16.7	479.2	20.8	23.0	167	26.1	46.5	56.0
Ni+3.0 wt%C	55	241	419.6	18.0	23.3	475.2	16.9	28.1	259	26.6	56.0	78.7
CR: cooling rate, Ave: Average , L: length, W: width, AR: aspect ratio, D: diameter												

The results of Table 1 shows that as the cooling rate decrease from 55 to 3 K/s the graphite flakes become coarsened while the quantity and size of spheres reduce. The longest flakes are the ones that probably started to grow from the beginning of cooling and could be used to calculate the growth rate. Moreover, the largest spheres have been probably cut diamterally and represent the diameter of the spheres that start to form from the beginning of cooling.

5.3. Graphite growth model

5.3.1. Graphite interfaces growth kinetics

The ultimate morphology of primary graphite crystals depends on the growth rates of graphite interfaces. For instance the shape of the graphite flakes in Fig. 68 indicates that the growth of prismatic planes were faster than the basal planes which lead the graphite crystal into more lengthening than thickening. The different growth rates of two graphite interfaces (basal and prismatic) are apparently due to different growth mechanisms which operate on the two faces. Before explaining the growth behavior of graphite interfaces, it would be pertinent to take a look at the crystal structure of graphite in more detail. Some typical planes of graphite crystals have been shown in Fig. 80. Due to layered structure, in normal situation the graphite crystal is always bounded by $\{0001\}$ basal plane, as shown in Fig. 80. In normal growth situation, the prismatic faces of graphite, however, include different family of planes including $\{10\bar{1}l\}$ [Fig. 80(a)], $\{11\bar{2}l\}$ [Fig. 80 (b)], or a combination of both [Fig. 80(c)]. In this case, when the hexagonal boundaries of graphite

contain planes of $\{10\bar{1}l\}$, the graphene edges in basal planes possess a zigzag form which has been shown schematically in Fig. 80(a). When the hexagonal boundaries are formed by planes of $\{11\bar{2}l\}$, the graphene edges have an armchair structure as shown in Fig. 80(b). Eventually when the crystal is bounded by both $\{10\bar{1}l\}$ and $\{11\bar{2}l\}$ planes, the graphene boundaries possess a mixed boundary configuration of zigzag and armchair seen in Fig. 80(c). The side view arrangements of the atoms in prismatic faces of $\{10\bar{1}0\}$ and $\{11\bar{2}0\}$ have been shown in Fig. 80(d), respectively.

Later it will be shown that the edge energy of the graphite σ_e, which is the result of dangling bonds in the boundaries, plays dominant role in defining nucleation and growth rates of interface. Considering E as the C-C molar bond energy, the total bonding energy in between two carbon atoms would be:

$$e = \frac{E}{4N_A} \times 2 = \frac{E}{2N_A} \qquad \text{(eq. 1)}$$

where N_A is Avogadro's number.

Assuming C-C bond molar energy and length of E=348 kJ/mol and a=154 pm respectively [1], the graphene edge energy for zigzag and armchair boundary would be:

$$\sigma_{e(zigzag)} = \frac{1}{2aCos\theta} \times \frac{2}{2} \times e = \frac{E}{4N_A aCos\theta} \qquad \text{(eq. 2)}$$

$$\sigma_{e(armchair)} = \frac{1}{3a} \times (1 + \frac{2}{2}) \times e = \frac{E}{3N_A a} \qquad \text{(eq. 3)}$$

where *a* is the C-C bond length in Fig. 80. So the values of edge free energies would be approximately $\sigma_{e(zigzag)}$=1.08 nJm^{-1} and $\sigma_{e(armchair)}$=1.25 nJm^{-1}. Later, these values of edge energy are utilized to calculate the nucleation and growth rates.

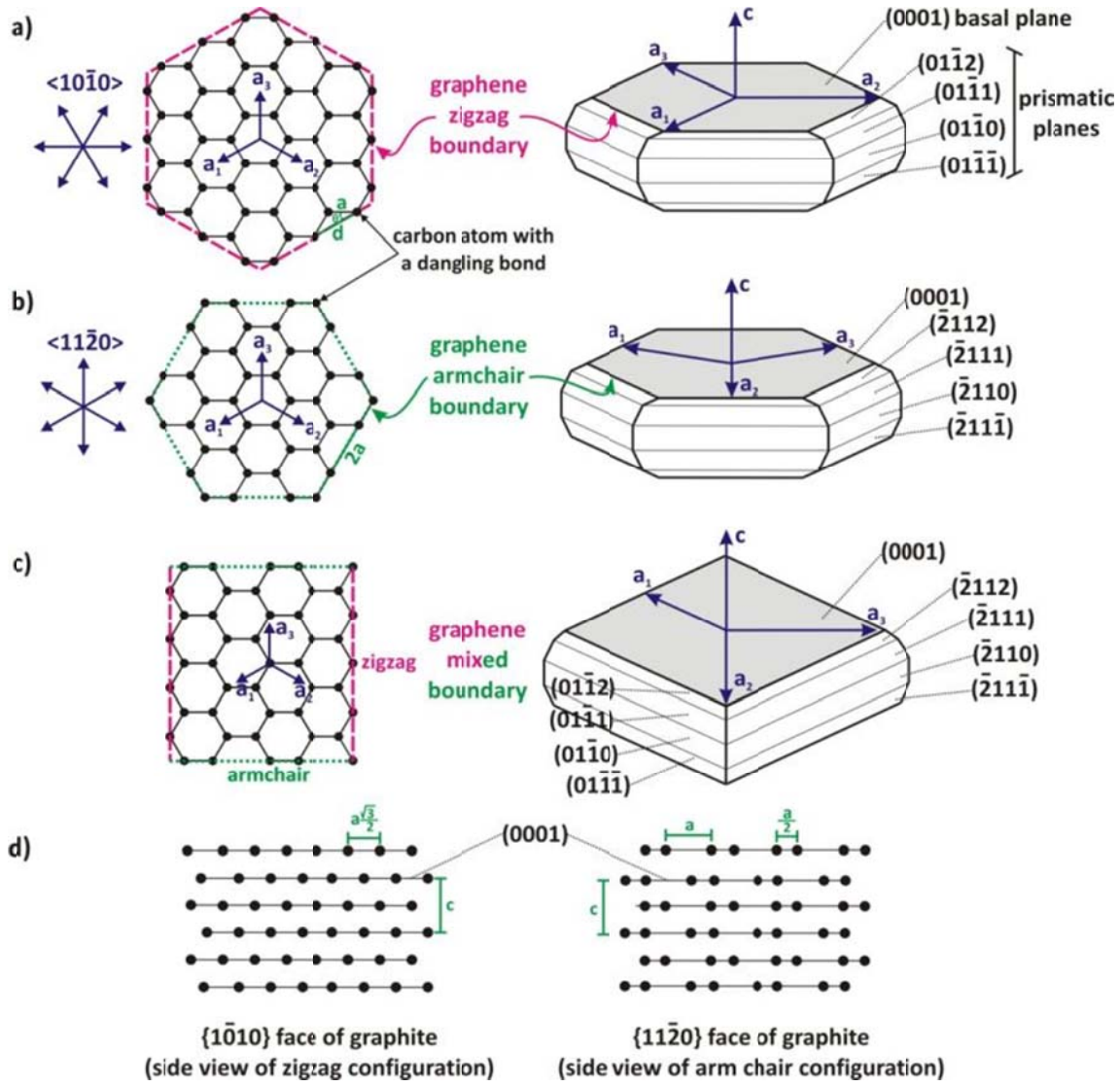

Fig. 80. Various graphite crystal structures and the resultant graphene boundaries

The driving force for nucleation and growth of a graphite crystal from metallic solution is the difference in chemical potential between a carbon atom in solution and that in the

graphite crystal which can be described by supersaturation. In small driving force the prismatic and basal interfaces of graphite are faceted low index planes [70]. Growth of these interfaces in this case takes place by lateral movement of the ledges produced by 2D-nucleation or spiral growth around a screw dislocation. It has been shown that when the crystal grows by 2D nucleation and migration of ledges, its growth rate increases exponentially with the driving force [56]. This has been shown schematically in Fig. 81(a). However, as the driving force increases, the faceted interfaces start to lose their planar structures as it becomes kinetically roughened [54-56]. This transition from faceted to non-faceted depends on the driving force as well as on the nature of the growth plane. In small driving force, interface will grow by a surface-controlled mechanism (e.g. 2D nucleation and growth or spiral growth around a screw dislocation). As the driving force increases, it reaches a critical value where the interface grows continuously by a diffusion-controlled mechanism. It has been shown that the growth rate of a roughened interface increases approximately linearly with the driving force [56] [Fig. 81(a)].

The concept of kinetically roughening transition for prismatic and basal faces of graphite has been shown in graph of Fig. 81(b). The graph depicts that in a definite supersaturation growth velocities change as $V_{\{11\bar{2}l\}} > V_{\{10\bar{1}l\}} > V_{\{0001\}}$. This is basically related to planar density of interfaces and the fact that planes with lower atomic density grow faster.

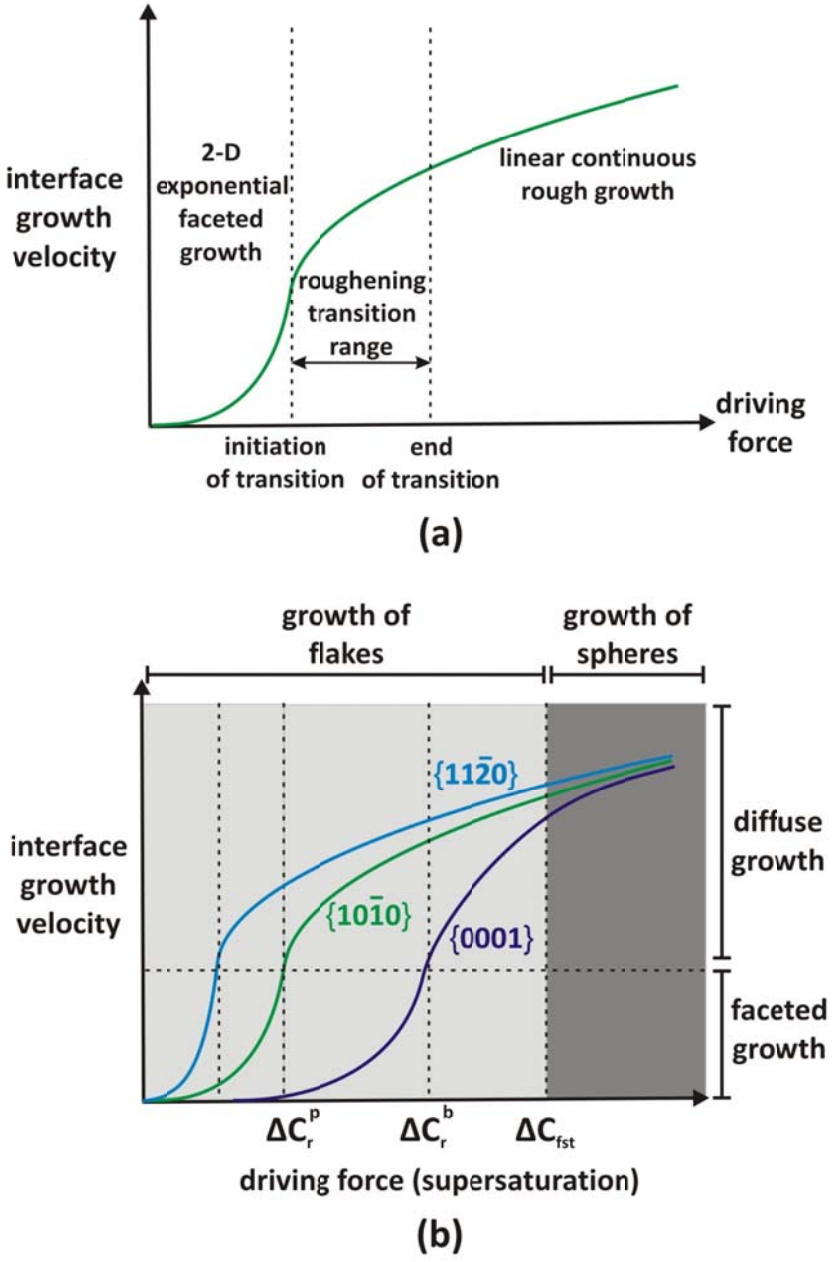

Fig. 81. a) Roughening transition of an interface along with different growth regimes as a function of driving force b) qualitative interface growth rates curves of basal $\{0001\}$ and prismatic $\{10\bar{1}l\}/\{11\bar{2}l\}$ interfaces of graphite: ΔC_r^b and ΔC_r^p are necessary supersaturations for kinetically roughening transition of basal and prismatic interfaces respectively, ΔC_{fst} is the necessary supersaturation for flakes to spheres morphology change

Based on the interface growth rate curves of Fig. 81(b), the kinetically driven flake to sphere morphology change can be understood. At small solidification rates, the graphite crystals are normally bounded by the faceted low index basal and prismatic planes. The prismatic face roughening transition occurs in smaller driving force than the basal plane. As such, at intermediate rates the prismatic interfaces become rough and grow faster while the basal plane is still faceted, leading to the formation of flake graphite. In extremely high growth rates, i.e. higher than ΔC_{fst} in Fig. 81(b), both interfaces grow roughly with a relatively similar rate, resulting in bulky spherical morphology. It is believed that for samples moderately cooled in levitation, the supersaturation is mostly in between ΔC_r^p and ΔC_r^b. So the flakes tips are diffuse and their growth is diffusion controlled. At the same supersaturation, the basal plane is faceted and its growth is surface-controlled. In extremely high supercooling which occurs in quenching of the melt droplets, the supersaturation is higher than ΔC_{fst} where both interfaces are diffuse and grow with relatively similar rate. This will result in the formation of bulky spheres.

5.3.2. Graphite nucleation

Fig. 82 shows the sequence of graphite flakes nucleation and growth schematically. The formed 3D graphite nucleus is shown at the time t_1. For regular nucleation, the surface energy is assumed to be isotropic, i.e. spherical nucleus. However, for graphite because of anisotropy, it is possible for the nucleus to be hockey pock or pancake shaped to minimize the total surface energy for nucleation.

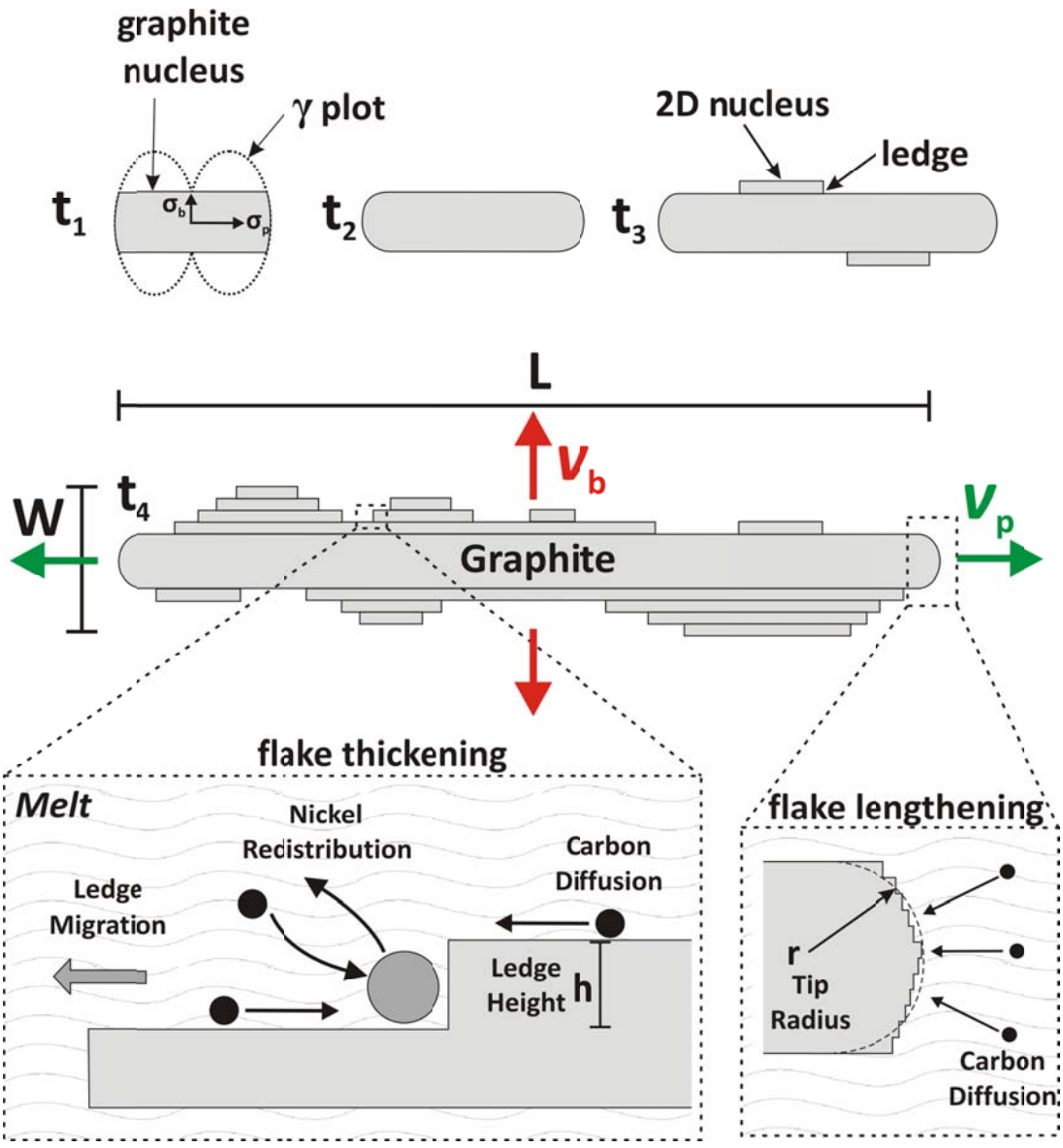

Fig. 82. Nucleation and growth of graphite flakes schematic (t: time, L: flakes length, W: flakes width, v_p: flakes tip growth velocity, v_b: flakes basal plane growth velocity)

The shape of the graphite nucleus could be better understood by its γ plot which is a method to plot variation of surface energy with surface orientation in 3D space [11]. If the surfaces of the graphite were isotropic with equivalent surface energies, the γ plot of

the graphite/melt interfacial energy would be fully spherical and the equilibrium shape of nucleus would be correspondingly spherical. Nevertheless, The surface energy of graphite prism face (σ_p) is about seven to ten times higher than the basal plane (σ_b) [33, 57]. Accordingly, the γ plot of the interfacial energy would be a sphere with two deep cusps normal to the basal plane which has been shown on the nucleus of Fig. 82 at the time t_1.

Based on the Wulff theorem [11] the equilibrium shape of graphite nucleus would now become hockey puck in a way to minimize the total surface energy:

$$\Sigma\sigma = S_b\sigma_b + S_p\sigma_p \qquad \text{(eq. 4)}$$

Where S_b and S_p are the basal and lateral areas respectively. Assuming a constant critical volume $V_{critical}$ for disk-shaped nucleus of diameter D and thickness b the total surface energy would be:

$$\Sigma\sigma = \frac{\pi D^2}{2}\sigma_b + \pi Db\sigma_p \qquad \text{(eq. 5)}$$

Since

$$V_{critical} = \frac{\pi D^2 b}{4} = k\,(\text{constant}) \qquad \text{(eq. 6)}$$

Then

$$\Sigma\sigma = \frac{\pi D^2}{2}\sigma_b + \frac{4k\sigma_p}{D} \qquad \text{(eq. 7)}$$

$$\Sigma\sigma' = \pi D\sigma_b - \frac{4k\sigma_p}{D^2} \qquad \text{(eq. 8)}$$

$$\Sigma\sigma' = 0 \rightarrow \frac{D}{b} = \frac{\sigma_p}{\sigma_b} \qquad \text{(eq. 9)}$$

So the diameter to thickness ratio of the nucleus is equivalent to prism to basal plane surface energy ratio.

5.3.3. Growth of flakes

As it was explained in section 5.3.1 in samples cooled in levitation, at moderate cooling rates the flakes tips are diffuse and their growth is controlled by carbon atoms diffusion toward the interface. The high accommodation factor of atoms in the prism face is owing to the presence of numerous ledges which contains closely spaced jogs. This has been shown schematically in the magnified view of the flake tip in Fig. 82. As such the lengthening of the flakes is by a diffusion controlled mechanism. However, at these moderate cooling rates, the basal plane grows faceted and its growth is controlled by lateral movement of the ledges. The generation of new ledges could dominantly be achieved by repeated 2D surface nucleation or intersection of screw dislocations with free surface. There are also other available mechanisms such as nucleation at the crystal edges, intersection with other crystals or termination of twins at the edges [54]. In our model the formation of ledges is presumed to be dominantly by the 2D nucleation in the basal plane since no evidence of spiral growth around screw dislocation were observed.

As the graphite nucleus form (section 5.3.2), the probability of 2D nuclei formation on top/bottom of it is low in view of the fact that the 2D nucleation rate is proportional to crystal face area [55, 56]:

$$I = AK_n \exp\left(\frac{\Delta G^*}{kT}\right) \qquad \text{(eq. 10)}$$

Where ΔG^*: the work needed to form a critical 2D nucleus, T: temperature, k: Boltzmann constant and K_n is an uncertain constant. As the nucleus grows, the nucleation event occurs repeatedly in the entire basal plane and the movement of the created ledges will contribute to the thickening of the graphite crystal (time t3 in Fig. 82).

Fig. 83(a) shows sequential 2D nuclei, which have been formed on a graphite single crystal. It is observed that as the 2D nuclei grow, they are bounded by polygonal faceted interfaces. The growing ledges of the graphite have also been shown in Fig. 83(b).

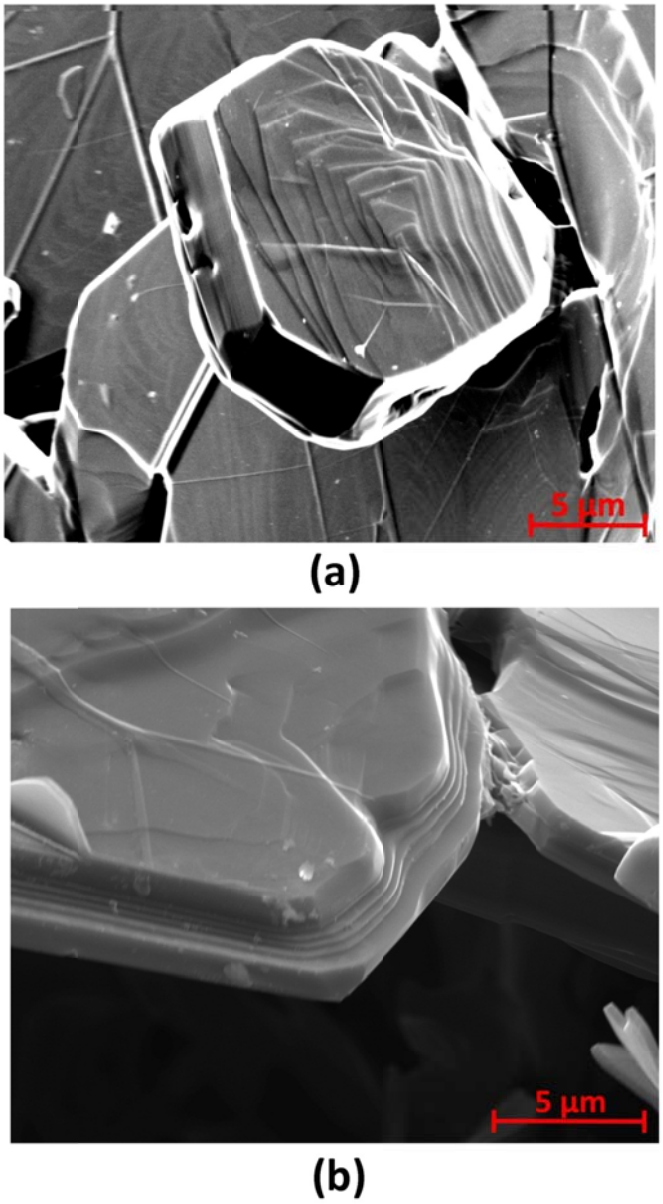

Fig. 83. a) Sequential graphite nuclei which have been formed on the basal plane b) growing ledges at the tip of a flake (cooling rate 55 K/s)

5.3.3.1. Diffusion controlled lengthening of flakes

The growth of a flake tip can be treated by diffusion controlled growth of a plate proposed by Zener [58]. In this case the flake tip velocity would be:

$$v_p = \frac{DV_m^{gr}}{kV_m^L}\left(\frac{C_0 - C_i}{C_C - C_r}\right)\frac{1}{r}\left(1 - \frac{r^*}{r}\right) \qquad \text{(eq. 11)}$$

Where D is carbon diffusivity in liquid metal, V_m^{gr} and V_m^L are molar volume of graphite and liquid metal, C_0 ,C_i, C_C and C_r are the carbon molar fractions at bulk liquid, liquid next to planar flake tip, graphite and liquid next to curved graphite tip, r is the flake tip radius Fig. 82, r^* is the radius of critical nucleus and k is a constant close to unity. The tip of a growing flake along with its concentration profile in front of it has been shown in Fig. 84. The radius of flake tip as well as radius of critical nucleus has also been shown schematically in Fig. 85.

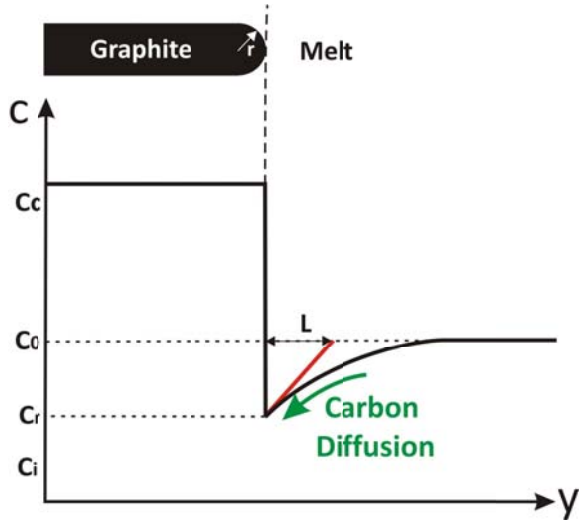

Fig. 84. The tip of a growing flake along with its concentration profile in front of it

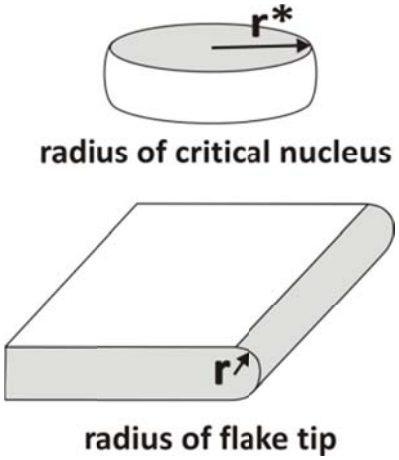

Fig. 85. Radius of curvature of dendrite and flake tips as well as nucleus critical radius

Fig. 86 also shows the nickel side of Ni-C phase diagram along with metastable Ni_3C in which C_0 , C_i and C_C .

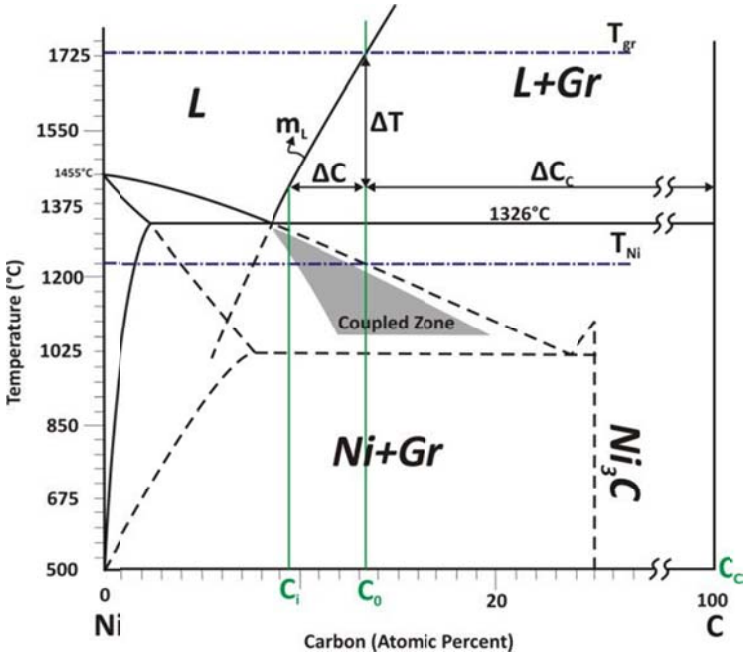

Fig. 86. Nickel-Carbon phase diagram along with metastable extension of nickel and graphite liquidus and carbide phase

Radius of curvature has two opposite effects on the growth velocity of the tip. Firstly, it will decrease the growth rate by reducing the concentration profile through the equation $\nabla C = \Delta C / kr$; Secondly, it increases the growth velocity by a factor proportional to $1 - r^* / r$ [10]. According to Zener suggestion, it is expected that the growing tip radius changes continuously to eventually reach its maximum growth velocity. So the critical radius of curvature in the flake tip would be the one that maximizes the growth rate:

$$\left.\frac{dv_p}{dr}\right|_{v_p^{\max}} = 0 \rightarrow r = 2r* \qquad \text{(eq. 12)}$$

Thus assuming isotropic interfacial energy for prism face, the maximum growth rate will occur when the tip radius of curvature is equivalent to $2r^*$.

By inserting (eq. 12) into (eq. 11):

$$v_p^{\max} = \frac{DV_m^{gr}}{kV_m^L}\left(\frac{C_0 - C_i}{C_C - C_r}\right)\frac{1}{2r^*} \qquad \text{(eq. 13)}$$

Assuming that $\Delta C_C = C_C - C_r \approx C_C - C_0$ is constant and $\Delta C = C_0 - C_i$ the flake tip velocity would be:

$$v_p^{\max} = \frac{DV_m^{gr}}{kV_m^L}\frac{\Delta C}{\Delta C_C}\frac{1}{2r^*} \qquad \text{(eq. 14)}$$

The tip radius of longest graphite flakes in the optical micrographs were measured to be approximately $r^* \approx 5\,\mu m$. Assuming V_m^{gr}=5.3 cm^3/mol, V_m^L=7.5 cm^3/mol, ΔC=3 atom%, ΔC_C=87 atom%, $k \approx 1$, $D = 7.5 \times 10^{-6} cm^2/s$ and $r^* \approx 5\,\mu m$ the $v_p^{\max}$=1.8 μms^{-1}. The

calculated tip growth rates in the prism face can be compared with the growth rate from the experimental results to test the validity of the model. Fig. 87 shows flakes half-length and width of Table 1as a function of total growth time between T_{gr} and T_{ni} in cooling curves. The slope of flake half-length and- width as a function of growth time are the growth rate of flake tip and basal plane respectively. It is observed that the experimental result for the growth velocity of the flakes tip is $1.8\,\mu ms^{-1}$ which is in good agreement with the predicted value by our model.

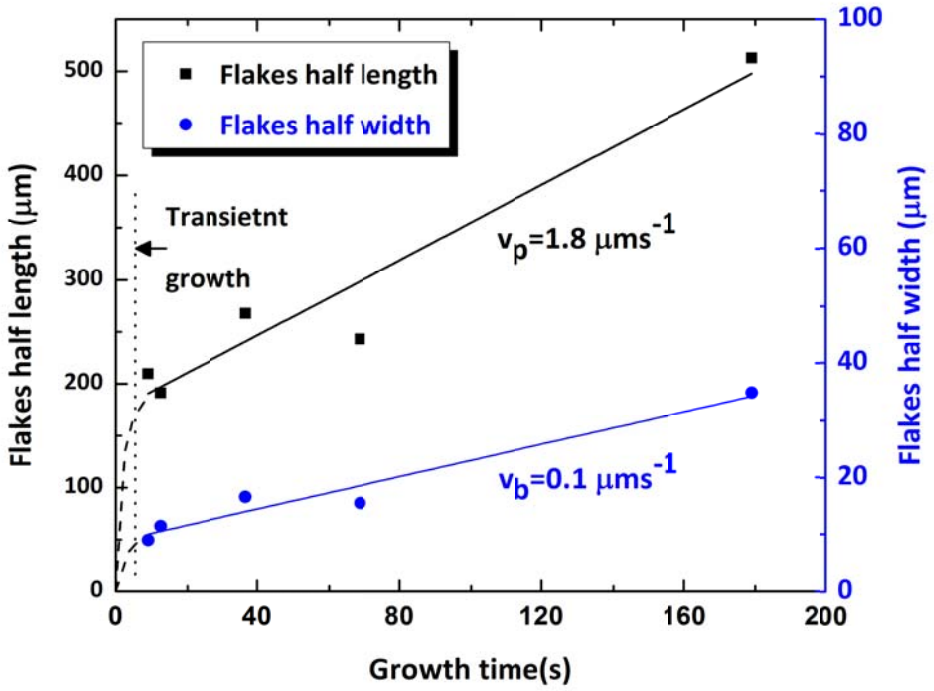

Fig. 87. Flakes half-length and width as a function of growth rate, the slop of steady state regimes are the growth rates in graphite tip and basal plane

The graphs in Fig. 87 show that initially there is a transient regime in both elongating and thickening of the flakes; subsequent to which growth becomes steady state. It is

conceivable that at the beginning of growth; the driving force for migration of interfaces is relatively high due to high amount of supersaturation and availability of carbon atoms in close neighboring of the interfaces.

5.3.3.2. Surface controlled thickening of flakes

The flakes thickening can be treated by 2D nucleation and growth (2DNG) model. 2DNG is divided into two regions based on the relative time between nucleation event and layer spreading. If a single nucleus forms and spread over the entire surface prior to occurring of next nucleation event, the growth is the so called monolayer nucleation and growth (MNG). However, if a large number of 2D nuclei form on the entire surface and also on top of the already growing islands before the layer spreading is complete, the growth is the so called poly nucleation growth (PNG). The MNG is observed to occur in very small driving force [55, 56] and it is believed that in moderate cooling rates of current experiments the PNG are dominant. Utilizing the poly nucleation growth model for graphite in the basal plane, thickening rate of the flakes would be obtained [56]. To use this model the following assumptions are made: a) the 2D nuclei thickness are as small as single graphene layer with a ledge height equal to graphite interlayer spacing, b) the 2D nuclei grow isotropically, c) the growing 2D nuclei are not affected by proximity of their neighbors, d) the ledge migration rate (v_e) is independent of the cluster size. By considering that for a disk shaped 2D nuclei the time, τ, needed for it to cover the interface is equal to the mean time between the genesis of two nuclei (i.e. the second one on top of the first) or otherwise given by:

$$\pi \int_0^{\tau} J(v_e t)^2 dt = 1 \qquad \text{(eq. 15)}$$

Where J is the nucleation rate.

If the thickening rate is assumed constant, it would be equal to:

$$v_b = \frac{h}{\tau} \qquad \text{(eq. 16)}$$

Where h is the ledge height in Fig. 82.

By Integration of (eq. 15) and using (eq. 16) the steady state growth rate of the graphite basal plane by poly nucleation growth model would be:

$$v_b = h\left(\frac{\pi J v_e^2}{3}\right)^{\frac{1}{3}} \qquad \text{(eq. 17)}$$

The 1/3 exponent on the equation is governed based on the assumption that the nucleus radius increases linearly with time. A similar treatment to that given to graphite tip (eq. 14) could be deployed for ledge migration rate. Thus presuming $h \approx 2r^*$ the lateral growth velocity of the ledges would be:

$$v_e = \frac{D V_m^{gr}}{k V_m^L} \frac{\Delta C}{\Delta C_C} \frac{1}{h} \qquad \text{(eq. 18)}$$

And by inserting (eq. 18) into (eq. 17) :

$$v_b = h\left(\frac{\pi J}{3}\right)^{\frac{1}{3}} \left(\frac{D V_m^{gr}}{k V_m^L} \frac{\Delta C}{\Delta C_C} \frac{1}{h}\right)^{\frac{2}{3}} \qquad \text{(eq. 19)}$$

The 2D nucleation rate in (eq. 19) is defined as the attachments frequency of an atom to a cluster of critical size. It has been shown that the 2D nucleation rate per unit area could be obtained by [56, 220]:

$$J = K_n \exp\left(-\frac{\Delta G^*}{kT}\right) \quad \text{(eq. 20)}$$

Where ΔG^*: the work needed to form a critical 2D nucleus, T: temperature, k: Boltzmann constant and K_n is an uncertain constant which is commonly taken to be in the range of $10^{21\pm2}$ [221].

The total formation work of a graphite disk with the height of h and radius of r on the basal plane is:

$$\Delta G = \pi r^2 h \Delta G_V + 2\pi r \sigma_e \quad \text{(eq. 21)}$$

where σ_e: the edge surface energy per unit length, ΔG_V: volumetric Gibbs free energy for formation of graphite from the melt. So:

$$\left(\frac{d\Delta G}{dr}\right)\Big|_{r^*} = 0$$

$$r^* = -\frac{\sigma_e}{h\Delta G_V} \quad \text{(eq. 22)}$$

And from (eq. 21) and (eq. 22):

$$\Delta G^* = -\frac{\pi \sigma_e^2}{h\Delta G_V} \quad \text{(eq. 23)}$$

$$J = K_n \exp\left(\frac{\pi\sigma_e^2}{h\Delta G_V KT}\right) \quad \text{(eq. 24)}$$

Inserting (eq. 24) into (eq. 19) the basal plane growth rate would be:

$$v_b = \left[\frac{\pi h K_n}{3}\exp\left(\frac{\pi\sigma_e^2}{h\Delta G_V KT}\right)\right]^{\frac{1}{3}}\left(\frac{DV_m^{gr}}{kV_m^L}\frac{\Delta C}{\Delta C_C}\right)^{\frac{2}{3}} \quad \text{(eq. 25)}$$

Assuming $h=3.5\times10^{-10}\,m$, $T=1873\,K$, $\Delta G_V=10^{10}\,J/m^3$ [222], $K_n=10^{21}$ [221] and $\sigma_e=1\,nJm^{-1}$ the growth rate of graphite basal plane would be $v_b=0.1\,\mu ms^{-1}$ which is in good agreement with the experimental results of Fig. 87.

5.3.4. Growth of spheres

Result of Table 1 shows that increasing the cooling rate will favor the formation of spheres. This morphology change could also be readily observed in the quenched samples where the microstructure is fully spherical [Fig. 78(e)]. The fact that the high cooling rates promotes the spheres formation have also previously observed in Ni-C, Fe-C-Si, Fe-C and Co-C systems [99, 115, 125-127], yet the nature of this kinetically driven morphology change has not been defined. Detailed microscopy of the spheres revealed that different growth mechanisms in various growth stages exist which are going to be explained in this section.

In high cooling rates (i.e. high driving force), upon the formation of a nucleus, its both basal and prismatic interfaces grow isotropically with relatively similar rates [Fig. 81 (b)]. Since both interfaces are growing fast, there is also high probability of defect

formation in the crystal. This is stage I of the growth and has been shown schematically in Fig. 88(a). Later, as the crystal becomes larger, it consumes the neighboring carbon atoms and the growth slows down. At this stage, the rough interfaces of crystal begin to form semi curved facets. There is high probability of introducing intrinsic defects into these facets owing to the fact that these locally faced interfaces will have to conform to the shape of the existing sphere. This could be understood by analogy with the gluing of flat tiles on a soccer ball where the tiles need to be slightly curved as well as having defective boundaries. The growing facets then run into one another forming boundaries on the surface. From these boundaries, new steps can develop and grow circumferentially over the surface, producing a pattern similar to cabbage leaves. This stage II of the growth has been shown in Fig. 88(b) where a growing step on the crystal has been marked by a red arrow. Later, as the supersaturation decreases more, graphite pillars emanate radially from the existing surface. This stage III of the growth is clearly observable in partially grown sphere of Fig. 88(c). The pillars will grow epitaxially on the existing surface, yet independent of each other to accommodate defects and structural features. The pillar growth continues into the melt until the metallic matrix nucleates and blocks the sphere from further growth. At this stage the spheres growth would be concluded [Fig. 88(d)]. The schematic morphology of a sphere has been shown in Fig. 88(e) in which different stages of growth have been marked. The difference in stage II and III can clearly be observed in schematic representation of Fig. 88(e). In stage II the curved graphite facets grow circumferentially to form a morphology similar to cabbage

leaves while in stage III the graphite pillars grow radially on the existing surface from stage II.

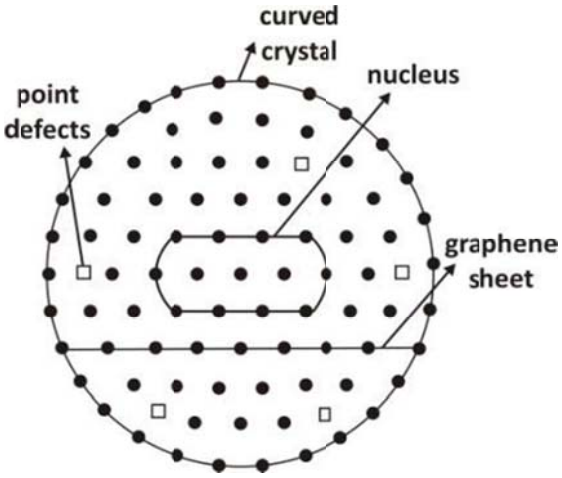

a) Stage I: nucleation and isotropic growth

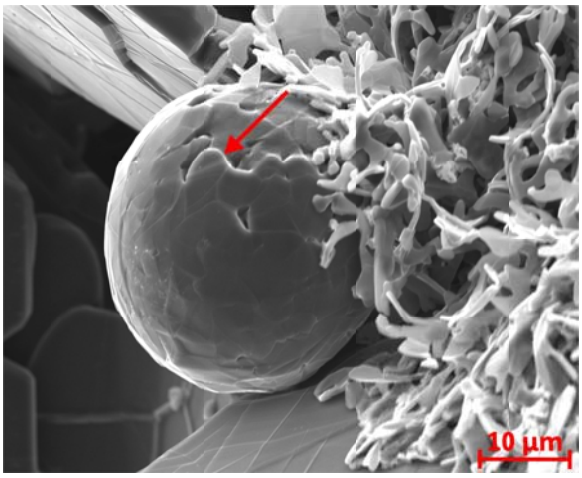

b) Stage II: cabbage leaves growth (circumferential growth of curved facets)

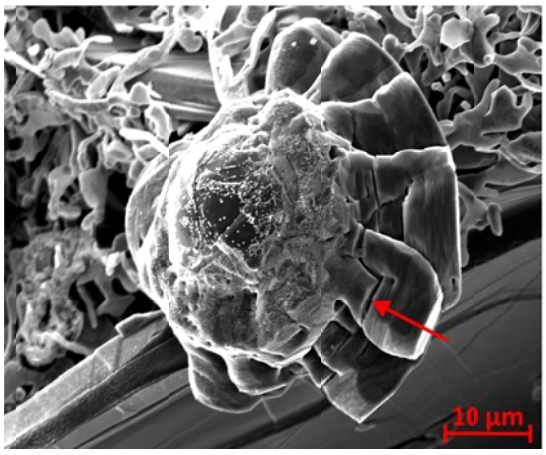

c) stage III: the radial growth of pillars

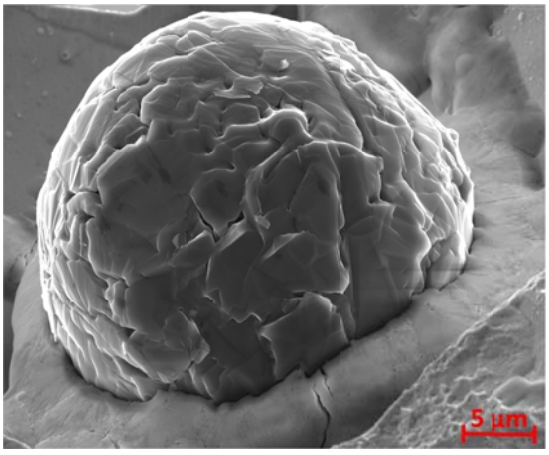

d) Final morphology

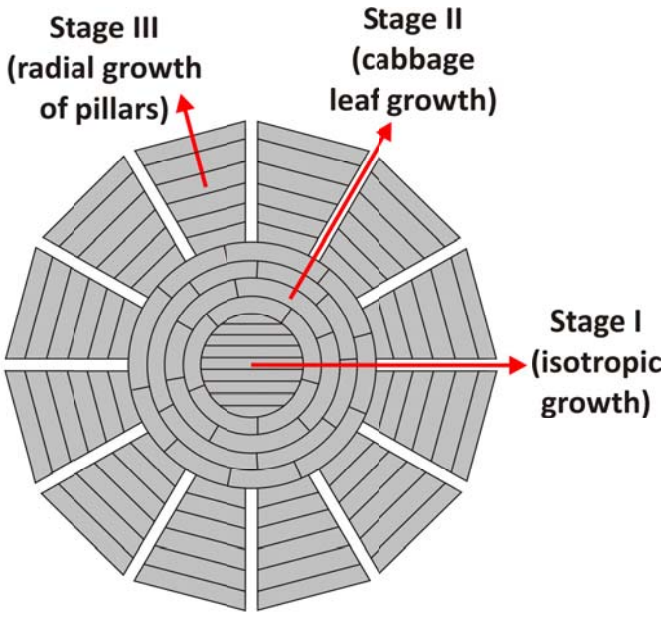

e) A schematic representation of sphere morphology

Fig. 88. Various stages of growth along with schematic morphology of a sphere

As the pillars are growing they may block each other's growth. In Fig. 88(c), as it is marked by a red arrow, some pillars took over and stop the growth of the neighboring ones. Moreover, these pillars are not fully conformed to each other and the regions in between them may be filled by solidified liquid at the last stage of solidification. Later the deep etching of the matrix will leave behind a sphere poly crystal which is porous [Fig. 88(d)].

Moreover, the spheres colonies which have grown in stage III will have a distinct core which frequently visible in the center of spheres in optical micrographs (Fig. 89). This feature is not an optical illusion, yet it is apparently the denser core of the spheres with a crystal structure which is dissimilar to outer region of the sphere.

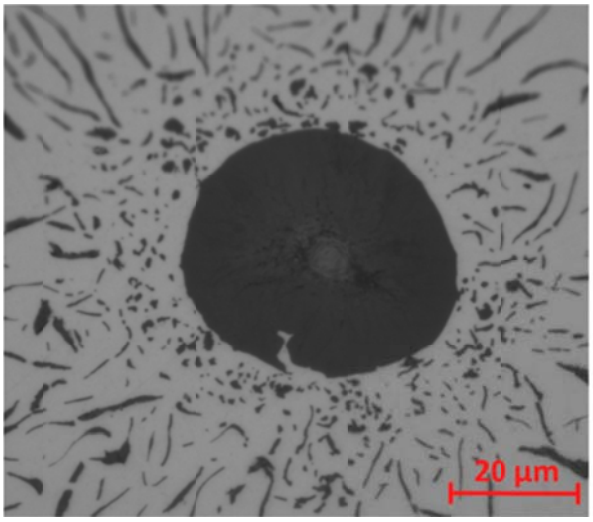

Fig. 89. The distinct core morphology visible in the center of spheres due to different structure

Furthermore, as the pillars are growing they may tilt and twist causing the famous rosette pattern of the spheres. This pattern has been shown in dark field optical micrographs of Fig. 90.

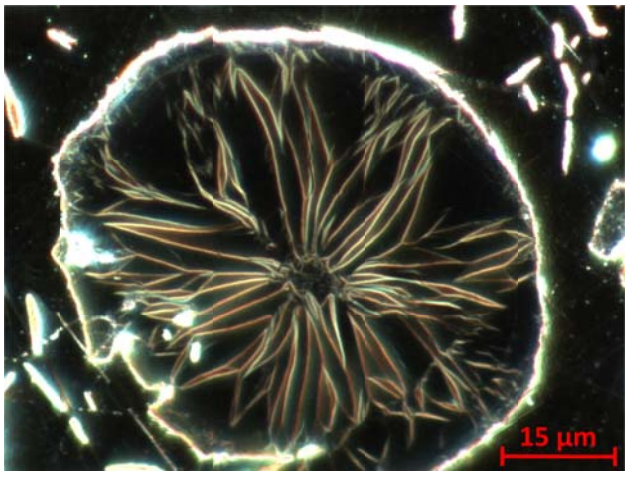

Fig. 90. Dark field optical micrograph shown the rosette pattern of radial graphite pillars in a spheres

It is pertinent to point out that as the spheres are growing in stage III, sphere to flake morphology change may also occur in some particles depending on the local growth conditions. The optical and scanning electron micrographs of this morphology change have been shown in Fig. 91. As the growth slows down in stage III, there are possibilities that the pillars start to take off from the sphere and grow into the liquid and form a flake. It is also conceivable that while a sphere is blocked by a metallic shell, a pillar may continue to grow locally in the form of a flake. To the best of my knowledge, this is the first study which reports a multi stage growth mechanism for graphite spheres. These complex growth mechanisms, to some extent, clarify why it has not been unanimity for growth of spheres for many years.

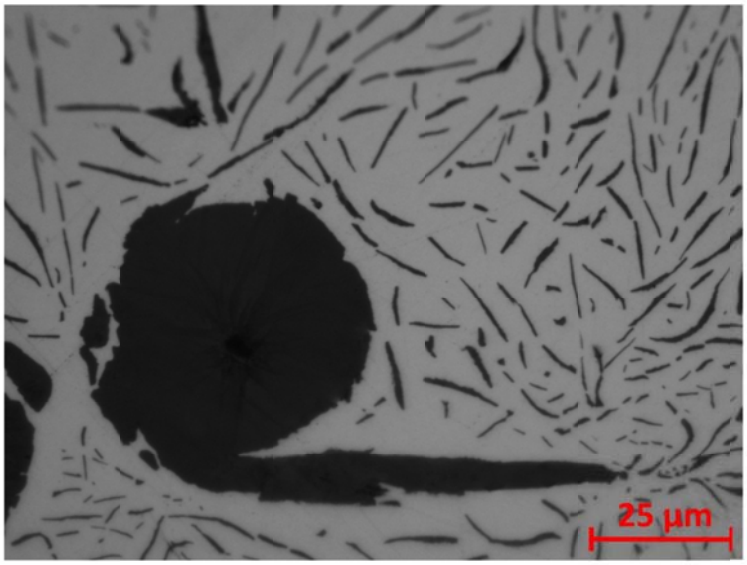

(a)

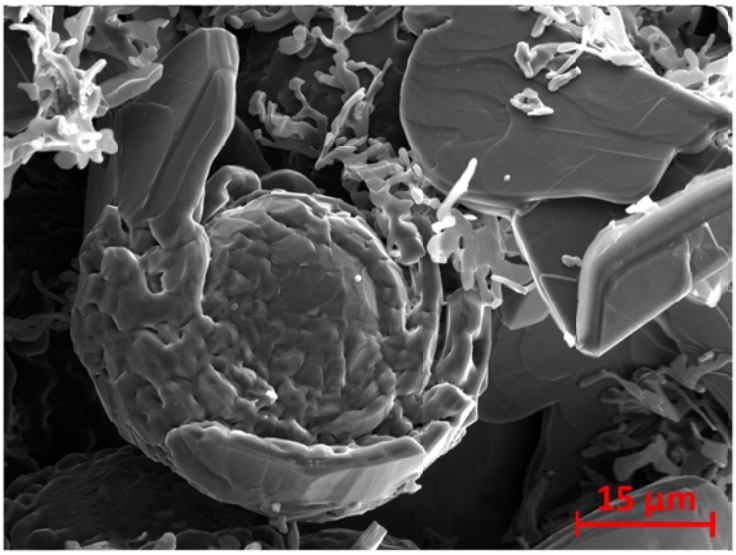

(b)

Fig. 91. a) Optical and b) scanning electron micrographs of sphere to flakes morphology change

5.4. Graphite growth defects and instabilities

Some frequent defects and irregularities were observed in the micrographs of the flakes which are the result of their 2D nucleation and growth in the basal planes. Examples are superledges, overhangs and cavities which are shown schematically along with their micrographs in Fig. 92. As the flakes ledges migrate, their lateral movements may be blocked by obstacles such as foreign impurities, inclusions or even larger metal atoms incorporated into the graphene lattice. In this case the ledges become immobile and pile up on each other and eventually form a superledge. In some instances, however, the upper part of the superledge may take off and continuously grow into the liquid and cause the formation of overhangs. Ultimately when the overhangs thicken, they would meet the crystal again and form internal cavities (Fig. 92).

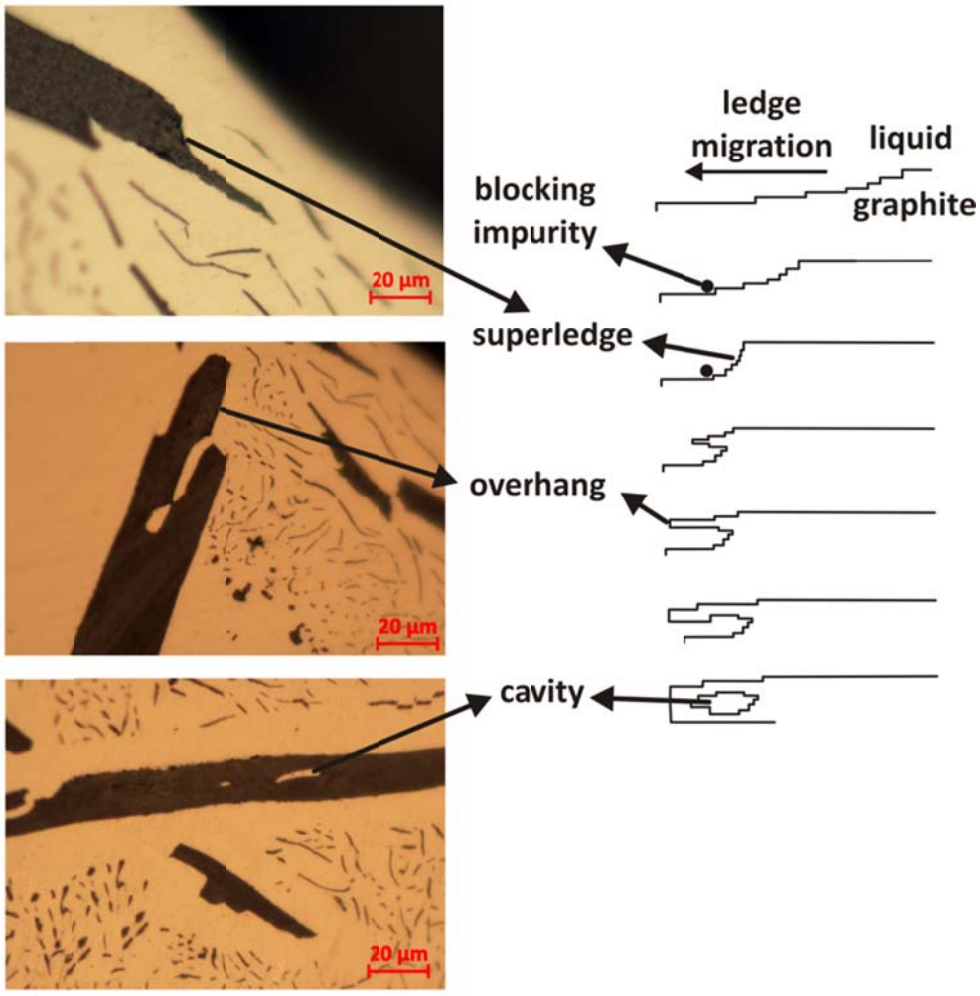

Fig. 92. Micrographs and the formation schematics of superledges, overhangs and cavities

Beside the abovementioned irregularities due to 2D nucleation and growth in the basal planes some growth instabilities in the tip were also observed. Examples include instabilities of growth in crystal corners, flake branching and growth blockage which have been shown and marked by red arrows in Fig. 93(a), (b) and (c) respectively along with their schematics.

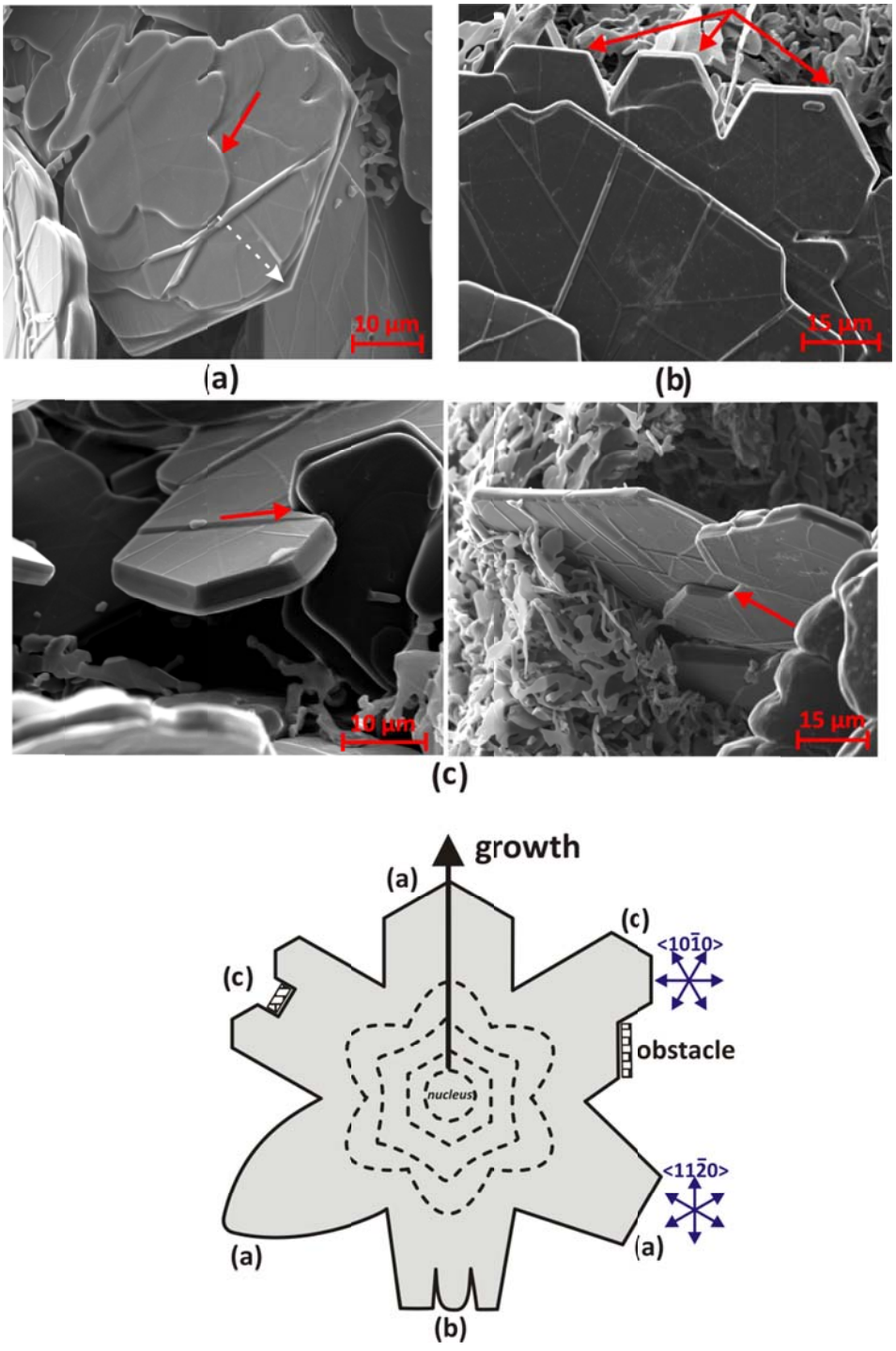

Fig. 93. Growth instabilities of the graphite flakes a) instabilities of growth in the crystal corners b) flake branching and c) growth blockage

Due to higher interfacial energies of graphite in prismatic and basal planes, the graphite nucleus has a hockey puck shape to minimize its total surface energy. However, as the nucleus grows, it may be bounded by faceted low index planes due to carbon atom consumption and reduction of growth driving force. At this stage the hexagons would from, whose corners would eventually become unstable due the fact that the growth in the corners is controlled by a large radial field in front of it while the growth of crystal edges is controlled by a planar field [223]. Therefore the corners would take off and form the morphologies similar to Fig. 93(a). As the growth proceeds the growth may slow down and become faceted once more. This transition has been shown by a dashed arrow in Fig. 93(a). It should be noted that instability of crystal corners is different from growth instabilities of faceted interfaces due to constitutional supercooling. Scale-wise the instability of Fig. 93(a) is large and occurs in the whole crystal while instabilities due to constitutional supercooling are small with an irregular spacing. Nevertheless, instability due to constitutional supercooling (tip branching) could clearly be seen in Fig. 93(b). Finally, the growth may be blocked at the tip by other growing crystals and graphite interfaces as instances are shown in Fig. 93(c).

In investigation of the flakes, both non-faceted and faceted tips were observed in the microstructure. Fig. 94(a) and (b) show two non-faceted and faceted tips respectively. As it was reported in section 5.3, at present cooling rates the flakes tip are mainly non-faceted. However, as the non-faceted tips grow into the liquid, their growth rate may slow down due to consumption of carbon atoms and reduction of growth driving force in the tip vicinity. The fast growing planes would then disappear and the tip rearranges itself

into low index facets. The reason for observation of both faceted and non-faceted tips is conceivably this morphology change due to reduction of growth driving force at the flake tip. This transition has been shown schematically in Fig. 94(c).

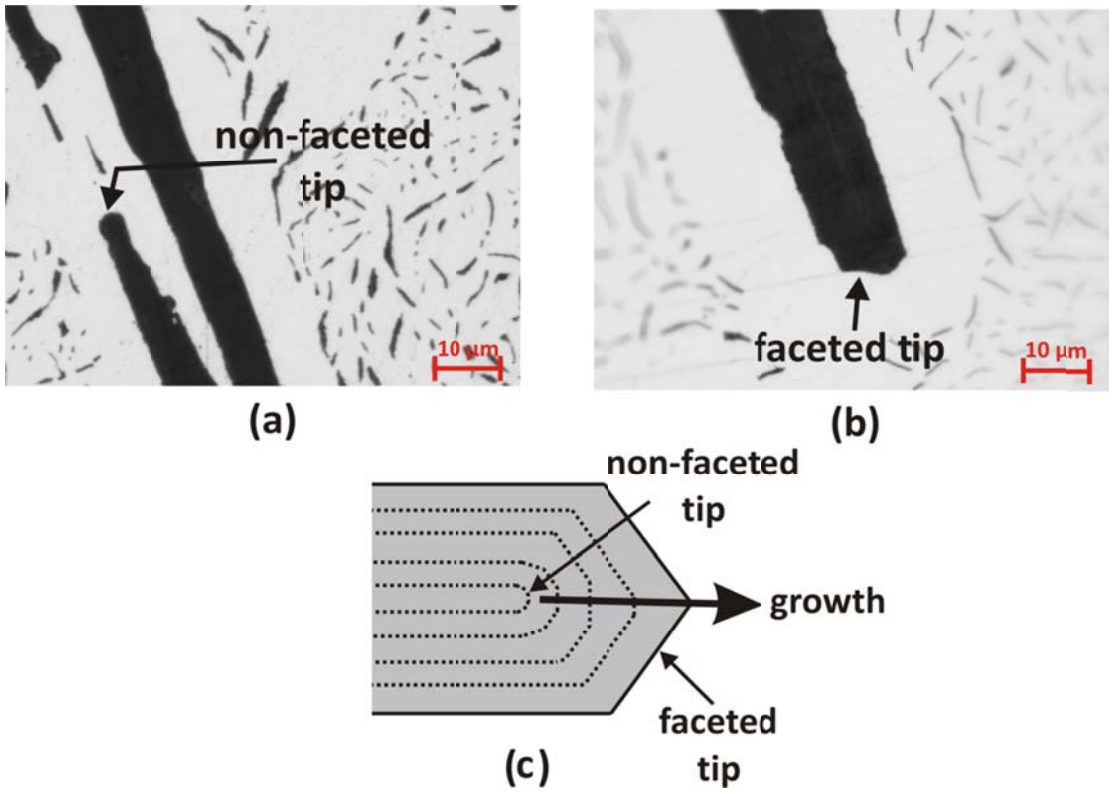

Fig. 94. a) Micrograph of a non-faceted tip b) Micrograph of a faceted tip c) Schematic of non-faceted to faceted transition at flakes tip during growth

It should be noted that a primary graphite flake has an evolving geometry and all these phenomena are occurring constantly due to complexity of the growth. Depending when the growth has been stopped, different shapes may be observed in the entire crystal. This will cause the flake shape to be complicated and similar to morphology of Fig. 68.

6. Conclusion

A new approach for growing large-area graphene and few-layer graphene films was proposed. The technique involved dissolving carbon in a molten metal at a specified temperature and then allowing the dissolved carbon atoms to nucleate and grow on top of the melt at a lower temperature. The detailed microscopy and micro-Raman spectroscopy were utilized to characterize the obtained layers. Different morphology including thick graphite, few and single layers were observed on metal substrates. The bulk graphite microstructure shows the flat areas bounded by the triangular faceted wrinkles formed due to the mismatch in the thermal expansion coefficients of the metal substrate and graphite. few layer graphene was also grown on both nickel and copper substrate. The Raman spectroscopy proved that single layer graphene larger than 125 μm^2 has been successfully grown on nickel substrate. The absence of the D and D' bands in the Raman spectrum of single layer graphene indicates graphene's high quality. It was found that nickel provides a better substrate for growing single layer graphene from the melt.

Various graphite morphologies which grow inside the electromagnetically levitated melts were also investigated. These morphologies included primary flakes and spheres, curved surface graphite, eutectic flakes as well as engulfed and entrapped particles were observed to grow during solidification of electromagnetically levitated nickel-carbon melts. As the hypereutectic melts were cooled from liquidus temperature, graphite flakes and spheres grew and accumulated near the surface due to electromagnetic mixing. The primary surface graphite was also observed to nucleate and grow on the liquid surface

which eventually formed a curved crystal covering the entire liquid. With further cooling, the liquid close to the surface solidified as a fine coupled eutectic while the liquid in the center went under a divorced eutectic reaction and formed engulfed and entrapped graphite particles. It was also observed that the microstructure of hypoeutectic melts was uniform and consisted of engulfed and entrapped graphite particles.

Nucleation and growth of graphene layers from metal-carbon melts was also studied in this research within the system of Ni-C. It was shown that the grown morphologies of graphite during cooling of supersaturated Ni-C melts depend on the solidification rate and supersaturation. At small solidification rates, the graphite crystals are normally bounded by faceted low index basal and prismatic planes. Growth of these faceted interfaces is by migration of the ledges produced by 2D-nucleation, and with a growth rate that increases exponentially with the driving force. However, as the growth rates increase, graphite interfaces become kinetically rough and the growth rate then becomes a linear function of the driving force and becomes limited by the diffusion of carbon to the growth interface. The roughening transition from faceted to non-faceted depends on the driving force as well as on the nature of the growth plane. Due to high number of C-C dangling bonds in prismatic face, its roughening transition occurs in smaller driving force than the basal plane. So at intermediate rates, the prismatic interfaces become rough and grow faster while the basal plane is still faceted, leading to the formation of elongated flaky graphite. In extremely high growth rates, however, both interfaces grow isotropically with a relatively similar rate leading to formation of graphite sphere. It was shown for the first time that the graphite spheres would grow in three different sequential stages including I)

basal and prismatic planes isotropic growth II) circumferential growth of graphite tiles and III) radial growth of pillars. An analytical model was developed for the lengthening and thickening rates of graphite flakes. Comparison of the theoretical results with the ones from experiments proved the validity of the proposed model.

7. References

[1] H.O. Pierson, Handbook of Carbon, Graphite, Diamond and Fullerenes: Properties, Processing, and Applications Noyes Publications, Park Ridge, NJ, 1993.
[2] I. Minkoff, Physical Metallurgy of Cast Iron John Wiley and Sons, 1983.
[3] R. Abbaschian, L. Abbaschian, R.E. Reed-Hill, Physical Metallurgy Principles 4ed., Cengage Learning 2009.
[4] M. Singleton, P. Nash, The C-Ni (Carbon-Nickel) system, Journal of Phase Equilibria, 10 (1989) 121-126.
[5] K. Ishida, T. Nishizawa, The C-Co (Carbon-Cobalt) system, Journal of Phase Equilibria, 12 (1991) 417-424.
[6] R.A. Sidorenko, Carbide Eutectic in Nickel-Carbon Alloys The Physics of Metals and Metallography, 4 (1959) 114-116.
[7] D. Stefanescu, Modeling of Cast Iron Solidification—The Defining Moments, Metallurgical and Materials Transactions A, 38 (2007) 1433-1447.
[8] J.R. Davis, ASM Specialty Handbook : Cast Irons, ASM International Materials Park, OH, 1996.
[9] M.E. Glicksman, Principles of Solidification: an Introduction to Modern Casting and Crystal Growth Concepts, springer, New York, 2011.
[10] P.G. Shewmon, Transformationa in Metals McGRAW HILL, New York, 1969.
[11] D.A. Porter, K.E. Easterling, Phase Transformations in Metals and Alloys Van Nostrand Reinhold, Wokingham, UK, 1981.
[12] B. Lux, Nucleation of Graphite in Fe-C-Si Alloys in: H.D. Merchanst (Ed.) Recent Research on Cast Iron Gordon and Breach Detroit, MI, 1964, pp. 241-279.
[13] D.D. Double, A. Hellawell, The Nucleation and Growth of Graphite—the Modification of Cast Iron, Acta Metallurgica et Materialia, 43 (1995) 2435-2442.
[14] M.-H. Teng, S.-W. Tsai, C.-I. Hsiao, Y.-D. Chen, Using diamond as a metastable phase carbon source to facilitate the synthesis of graphite encapsulated metal (GEM) nanoparticles by an arc-discharge method, Journal of Alloys and Compounds, 434–435 (2007) 678-681.
[15] C.-C. Chiu, J.-C. Lo, M.-H. Teng, A novel high efficiency method for the synthesis of graphite encapsulated metal (GEM) nanoparticles, Diamond and Related Materials, (2011).
[16] R.H. McSwain, C.E. Bates, Surface and Interfacial Energy Relationships Controlling Graphite Formation in Cast Iron, in: B. Lux, I. Minkoff, F. Mollard (Eds.) Second International Symposium on the Metallurgy of Cast Iron Georgi, Geneva, Switzerland 1974, pp. 423-440.
[17] L. Xu, Y. Lin, W. Cai, X. Shao, From multilayered graphite flakes to nanostructures: A tight-binding molecular dynamics study, The Journal of Chemical Physics, 129 (2008) 224709-224706.
[18] H.W. Kroto, J.R. Heath, S.C. O'Brien, R.F. Curl, R.E. Smalley, C60: Buckminsterfullerene, Nature, 318 (1985) 162-163.

[19] R.L. Snezhnoy, A.A. Zhukov, Factors Affecting Graphite Shape in Cast Iron in: B. Lux, I. Minkoff, F. Mollard (Eds.) Second International Symposium on the Metallurgy of Cast Iron Metallurgy of Cast Iron Georgi, Geneva, Switzerland 1974, pp. 13-29.
[20] P.M. Thomas, J.E. Gruzleski, Formation of Nodules in Cast Iron withouit the Addition of a Nodularizer Journal of Iron and Steel Institute 211 (1973) 426-428.
[21] R.J. Warrick, Spheroidal Graphite Nuclei in Rare Earth and Magnesium Inoculated Irons, AFS Transactions, 74 (1966) 722-733.
[22] A. Hatton, M. Engstler, P. Leibenguth, F. Mücklich, Characterization of Graphite Crystal Structure and Growth Mechanisms Using FIB and 3D Image Analysis, Advanced Engineering Materials, 13 (2011) 136-144.
[23] H. Zeedjick, Identification of the Nuclei in Graphite Spheroids, Journal of Iron and Steel Institute, 203 (1965) 737-738.
[24] T. Skaland, Ø. Grong, T. Grong, A Model for the Graphite Formation in Ductile Cast Iron: Part I.Inoculation Mechanisms, Metallurgical and Materials Transactions A, 24 (1993) 2321-2345.
[25] F.C. Campbell, Elements of Metallurgy and Engineering Alloys, in, ASM International, 2008.
[26] J. Campbell, Complete Casting Handbook: Metal Casting Processes, Techniques and Design, Elsevier, 2011.
[27] E. Fras, M. Gorny, H.F. Lopez, Eutectic Cell and Nodule Count in Cast Iron Part I. Theoretical Background, ISIJ International, 47 (2007) 259–268.
[28] A. Velichko, C. Holzapfel, F. Mücklich, 3D Characterization of Graphite Morphologies in Cast Iron, Advanced Engineering Materials, 9 (2007) 39-45.
[29] E. FraŚ, K. Wiencek, M. GÓRny, H.F. LÓPez, Graphite Nodule and Eutectic Cell Count in Cast Iron: Theoretical Model Based on Weibull Statistics and Experimental Verification, Metallurgical and Materials Transactions A, 38 (2007) 385-395.
[30] W.D. Callister, Materials Science and Engineering: An Introduction, 5 ed., John Wiley & Sons, 2000.
[31] ASM Handbook, Metallography and Microstructures, ASM Publication, 2004.
[32] C.A. Cooper, R. Elliott, R.J. Young, Investigation of elastic property relationships for flake and spheroidal cast irons using Raman spectroscopy, Acta Materialia, 50 (2002) 4037-4046.
[33] D.M. Stefanescu, Science and Engineering of Casting Solidification, Kluwer Academic/Plenum Publishers, New York, 2002.
[34] J.E. Rehder, Transaction of American Foundry Society, 16 (1949) 33.
[35] A.P. Lyubchenko, M.V. Mozharov, D.G. Sherman, Phys. Met. Metallogr., 18 (1964) 54-61.
[36] A.P. Lyubchenko, D.G. Sherman, Phys. Met. Metallogr., 20 (1965) 132-135.
[37] A. Hultgren, Y. Lindblom, E. Rudberg, Eutectic Solidification in Grey, White and Mottled Hypo-eutectic Cast Irons, Journal of the Iron and Steel Institute, 176 (1954) 365-374.
[38] A.P. Lyubchenko, M.V. Mozharov, Y.G. Bobro, Phys. Met. Metallogr., 12 (1961) 63-68.

[39] B. Dhindaw, J.D. Verhoeven, Nodular graphite formation in vacuum melted high purity Fe-C-Si alloys, MTA, 11 (1980) 1049-1057.
[40] J.F. Wallace, American Foundry Society Transactions, 83 (1975) 75.
[41] J.S. Park, J.D. Verhoeven, Transitions between type A flake, type D flake, and coral graphite eutectic structures in cast irons, Metallurgical and Materials Transactions A, 27 (1996) 2740-2753.
[42] W. Kurz, The Solidification of Metal, Iron and Steel Institute, 110 (1968) 269.
[43] B. Lux, M. Grages, D. Sapey, W. Kurz, praktische Metallographie, 5 (1968) 123-126, 567-571, 587-603.
[44] H. Fredriksson, S.E. Wetterfall, A Study of Transition from Undercooled to Flake Graphite in Cast Iron, in: B. Lux, I. Minkoff, F. Mollard (Eds.) The Metallurgy of Cast Iron, Georgi Publishing, Geneva, Switzerland, 1974, pp. 277-293.
[45] P.C. Liu, C.R. Loper, T. Kimura, E.N. Pan, Observation of the Graphite Morphology of Compacted Graphite Cast Iron, Transaction of American Foundry Society 89 (1981) 65-77.
[46] M. Bazdar, H.R. Abbasi, A.H. Yaghtin, J. Rassizadehghani, Effect of sulfur on graphite aspect ratio and tensile properties in compacted graphite irons, Journal of Materials Processing Technology, 209 (2009) 1701-1705.
[47] J.M. Radzikowska, Effect of specimen preparation on evaluation of cast iron microstructures, Materials Characterization, 54 (2005) 287-304.
[48] R.D. Scheleng, Effect of Certain Elements on the Form of Graphite in Cast Iron, Journal of Cast Metals Research, 3 (1967) 30-38.
[49] B. Lux, I. Minkoff, F. Mollard, E. Thury, Branching of Graphite Crystals Growing From a Metallic Solution, in: B. Lux, I. Minkoff, F. Mollard (Eds.) Second International Symposium on the Metallurgy of Cast Iron Georgi Publishing, Geneva, Switzerland 1974, pp. 495-508.
[50] M. Hamasumi, On the Imperfection of Graphite Spherulite in Nodular Iron, Transactions of the Japan Institute of Metals, 5 (1964) 259-272.
[51] M. Hamasumi, A Newly Observed Pattern of Imperfect Graphite Spherulite in Nodular Iron Transactions of the Japan Institute of Metals, 6 (1965) 234-239.
[52] M. Hamasumi, Journal of Cast Metals Research 1(1965) 9-22.
[53] G.S. Cole, Solidification of Ductile Iron, Transaction of American Foundry Society, 80 (1972) 335-346.
[54] J.W. Cahn, W.B. Hillig, G.W. Sears, The Molecular Mechanism of Solidification, Acta Metallurgica, 12 (1964) 1421-1439.
[55] S. Peteves, R. Abbaschian, Growth Kinetics of Solid-Liquid Ga Interfaces: Part I. Experimental, Metallurgical and Materials Transactions A, 22 (1991) 1259-1270.
[56] S. Peteves, R. Abbaschian, Growth Kinetics of Solid-Liquid Ga Interfaces: Part II. Theoretical, Metallurgical and Materials Transactions A, 22 (1991) 1271-1286.
[57] M. Hillert, Some Theoretical Considerations in Nucleation and Growth during Solidification of Graphitic and White Cast Iron in: H.D. Merchant (Ed.) Recent Research on Cast Iron Gordon and Breach, Detroit, MI, 1964, pp. 101-127.
[58] C. Zener, Theory of Growth of Spherical Precipitates from Solid Solution, Journal of Applied Physics, 20 (1949) 950-953.

[59] I. Minkoff, Crystal Growth Theory and Cast Iron Structures, in: G. Ohira, T. Kusakawa, E. Niyama (Eds.) Physical Metallurgy of Cast Iron IV, Materials Research Society Tokyo, Japan, 1989, pp. 3-13.
[60] R. Elliott, Cast Iron Technology, Butterworth & Co., UK, 1988.
[61] W.K. Burton, N. Cabrera, F.C. Frank, The Growth of Crystals and the Equilibrium Structure of their Surfaces, Philosophical Transactions of the Royal Society of London. Series A, Mathematical and Physical Sciences, 243 (1951) 299-358.
[62] K. Byrappa, T. Ohachi, Crystal Growth Technology, William Andrew Inc., 2003.
[63] A. Munitz, S. Nadiv, Effect of doping elements on the morphology of graphite grown from Ni-C melts, Journal of Materials Science, 17 (1982) 3409-3422.
[64] I. Minkoff, W.C. Nixon, Scanning Electron Microscopy of Graphite Growth in Iron and Nickel Alloys, Journal of Applied Physics, 37 (1966) 4848-4855.
[65] N. Cabrera, D.A. Vermilyea, Growth and Perfection of Crystals, John Wiley, 1958.
[66] D.D. Double, A. Hellawell, Cone-helix growth forms of graphite, Acta Metallurgica et Materialia, 22 (1974) 481-487.
[67] J.A. Jaszczak, G.W. Robinson, S. Dimovski, Y. Gogotsi, Naturally occurring graphite cones, Carbon, 41 (2003) 2085-2092.
[68] M. Orona, I. Minkoff, Growth Twining in Graphite Dendrites, The Philosophical Magazine 9(1964) 1059-1062.
[69] M. Oron, I. Minkoff, A novel form of x-ray diffraction microbeam camera, Journal of Scientific Instruments, 42 (1965) 337.
[70] I. Minkoff, B. Lux, Graphite Growth From the Melt, in: B. Lux, I. Minkoff, F. Mollard (Eds.) Second International Symposium on the Metallurgy of Cast Iron Metallurgy of Cast Iron Georgi Geneva, Switzerland, 1974, pp. 473-491.
[71] D.D. Double, A. Hellawell, Defects in Eutectic Flake Graphite, Acta Metallurgica et Materialia, 19 (1971) 1303.
[72] W. Bollmann, B. Lux, Grain Boundaries in Graphite, in: B. Lux, I. Minkoff, F. Mollard (Eds.) Second International Symposium on the Metallurgy of Cast Iron Georgi, Geneva, Switzerland 1974, pp. 461-471.
[73] J. Keverian, H.F. Taylor, J. Wulff, Experiments on Spherulite Formation in Cast Iron, Journal of American Foundryman, 23 (1953) 85-91.
[74] F.H. Buttner, H.F. Taylor, J. Wulff, Graphite Nodules: a Note on Spherulization of Graphite in Cast Iron Journal of American Foundryman, 20 (1951) 49-50.
[75] H. Geilenberg, A Critical Review on the Crystallization of Graphite from Metallic Solutions after the Surface Tension Theory in: H.D. Merchant (Ed.) Recent Research on Cast Iron Gordon and Breach, Detroit, MI, 1964, pp. 195-210.
[76] J.P. Sadocha, J.E. Gruzleski, The Mechanism of Graphite Spheroid Formation in Pure Fe-C-Si Alloys in: B. Lux, I. Minkoff, F. Mollard (Eds.) The Metallurgy of Cast Iron, Georgi Publishing, Switzerland, 1974, pp. 443-456.
[77] J.Keverian, H.F.Taylor, J.Wulff, Experiments on Spherulite Formation in Cast Iron, Journal of American Foundryman, 23 (1953) 85-91.
[78] B. Lux, H. Tannenberger, ", , No. 3, . Inoculation Effect on Graphite Formation in Pure Fe-C-Si, Modern Casting, 41 (1962) 57.
[79] B. Lux, AFS Cast Metals Research Journal, 8 (1972) 49–65.

[80] P.M. Thomas, J.E. Gruzleski, A method for laboratory scale melting and solidification studies of cast irons, Journal of Materials Science, 7 (1972) 358-359.
[81] W.C. Johnson, H.B. Smartt, Solidification and Casting of Metals, The Metal Society, 1979.
[82] B. Lux, On the Theory of Nodular Graphite Formation in Cast Iron: Part I - Experimental Observations of Spherulitic Graphite Formation During Solidification of Cast Iron Melts, Journal of Cast Metals Research 8(1972) 25-45.
[83] C.K. Donoho, Modern Castings, 46 (1964) 608.
[84] J.C. Sawyer, J.F. Wallace, American Foundry Society Transactions, 76 (1968) 386.
[85] H. Morrogh, The Harmful Influence of Some Residual Elements in Magnesium Treated Nodular Cast Irons and their Neutralisation by Cerium, BCIRA Journal of Research and Development, 4 (1952) 292–314.
[86] T. Carlberg, H. Fredriksson, Influence of Silicon and Aluminuim on the Solidification fo Cast Iron in: International Conefernce on Solidification and Casting of Metals Sheffield, UK, 1977.
[87] H. Morrogh, W.J. Williams, Journal of Iron and Steel Institute, 159 (1948) 306-322.
[88] H. Morrogh, W.J. Williams, Journal of Iron and Steel Institute, 160 (1948) 21-29.
[89] R.P. Dumphy, W.S. Pellini, Foundry, 50 (1952) 82-86.
[90] R.P. Dumphy, W.S. Pellini, Foundry, 50 (1952) 195-196.
[91] R.P. Dumphy, W.S. Pellini, Foundry, 50 (1952) 198-200.
[92] A. Wittmoser, Giesserei techn. wiss. Beih, 40 (1953) 8-16.
[93] E. Scheil, Giesserei techn. wiss. Beih, 24 (1959) 1313-1338.
[94] E. Piwowarsky, A. Wittmoser, in, German Patent, No.864 404, 1949.
[95] E. Scheil, L. Hutter, Untersuchungen uber die kristallisation des Gusseisens mit Kugelgraphite Arch. Eisenhuttenweses, 4 (1953) 24.
[96] J.D. Schobel, Precipitation of Graphite during the Solidification of Nodular Cast Iron in: H.D. Merchant (Ed.) Recent Research of Cast Iron Detroit, MI, 1964, pp. 303-331.
[97] H. Siepman, F.W. Hauptvogel, Rheinstahl-Techn., 1 (1963) 16-23.
[98] H. Kempers, Giesserei, 53 (1966) 841-846.
[99] S. Banerjee, A Review of the Formation of Spheroidal Graphite in Cast Iron, British Foundaryman, 58 (1965) 344-352.
[100] E. Scheil, J.D. Schobel, Giesserei techn. wiss. Beih, 13 (1961) 203-213.
[101] H. Muhlberger, Arch. Eisenhuttenweses, 33 (1962) 681-698.
[102] D. Venugopalan, A kinetic model of the $\gamma \rightarrow \alpha$ + Gr eutectoid transformation in spheroidal graphite cast irons, Metallurgical and Materials Transactions A, 21 (1990) 913-918.
[103] S.E. Wetterfall, H. Fredriksson, M. Hillert, Solidification Process of Nodular Cast Iron Journal of Iron and Steel Institute, 210 (1972) 323.
[104] E. Scheil, L. Hutter, Arch. Eisenhuttenweses, 24 (1953) 237-246.
[105] M. Hillert, Y. Lindblom, Journal of the Iron and Steel Institute, 176 388.
[106] A.V. Shubnikov, Soviet Physics Crystallography, 2 (1959) 578-582.
[107] I. Minkoff, Solidification of Metals Iron and Steel Institute, 110 (1968).

[108] H.D. Keith, J.F.J. Padden, A Phenomenological Theory of Spherulitic Crystallization, Journal of Applied Physics, 34 (1963) 2409-2421.
[109] H.D. Keith, J.F.J. Padden, Spherulitic Crystallization from the Melt. I. Fractionation and Impurity Segregation and Their Influence on Crystalline Morphology, Journal of Applied Physics, 35 (1964) 1270-1285.
[110] H.D. Keith, J.F.J. Padden, Spherulitic Crystallization from the Melt. II. Influence of Fractionation and Impurity Segregation on the Kinetics of Crystallization, Journal of Applied Physics, 35 (1964) 1286-1296.
[111] W. Oldfield, G.T. Geering, W.A. Tiller, Solidification of Spheroidal and Flake Graphite Cast Iron, The Solidification of Metals, Iron and Steel Institute, 110 (1967) 256-262.
[112] T. Alp, F. Yilmaz, A.A. Wazzan, Microstructural Characteristics-Property Relationships in Cast Irons, in: The 6th Saudi Engineering Conference, KFUPM, Dhahran, 2002.
[113] M.B. Haanstra, W.F. Knippenber, G. Verspui, in: 5th European Congress on Electron Microscopy, Manchester (Institute of Physics), 1972, pp. 214.
[114] M.J. Hunter, G.A. Chadwick, Structure of Spheroidal Graphite, Journal of the Iron and Steel Institute, 210 (1972) 117-123.
[115] M.J. Hunter, G.A. Chadwick, Nucleation and Growth of Spheroidal Graphite Alloys, Journal of the Iron and Steel Institute, 210 (1972) 707-717.
[116] W. Johnson, H. Smartt, The Role of Interphase Boundary Adsorption in the Formation of Spheroidal Graphite in Cast Iron, Metallurgical and Materials Transactions A, 8 (1977) 553-565.
[117] S. Chang, D. Shangguan, D. Stefanescu, Modeling of the liquid/solid and the eutectoid phase transformations in spheroidal graphite cast iron, Metallurgical and Materials Transactions A, 23 (1992) 1333-1346.
[118] K. Kinsman, E. Eichen, H. Aaronson, Thickening kinetics of proeutectoid ferrite plates in Fe-C alloys, Metallurgical and Materials Transactions A, 6 (1975) 303-317.
[119] T. Skaland, Ø. Grong, T. Grong, A model for the graphite formation in ductile :Part II. Solid State Transformation Reactions Metallurgical and Materials Transactions A, 24 (1993) 2347-2353.
[120] H. Fredriksson, J. Stjerndahl, J. Tinoco, On the solidification of nodular cast iron and its relation to the expansion and contraction, Materials Science and Engineering: A, 413-414 (2005) 363-372.
[121] D.M. Stefanescu, Solidification of Flake, Compacted/Vermicular and Spheroidal Graphite Cast Irons as Revealed by Thermal Analysis and Directional Solidification, in: H. Fredriksson, M. Hillert (Eds.) The Physical Metallurgy of Cast Iron Materials Research Society Stockholm, Sweden 1984, pp. 151-162.
[122] D.K. Bandyopadhyay, D.M. Stefenascu, I. Minkoff, Structural Transitions in Directionally Solidified Spheroidal Graphite Cast Iron in: G. Ohira, T. Kusakawa, E. Niyama (Eds.) Physical Metallurgy of Cast Iron IV, Materials Research Society Tokyo, Japan, 1989, pp. 27-34.
[123] D. Argo, J.E. Gruzleski, Structural Transactions in Directionally Solidified Graphite Cast Irons, Materials Science & Technology, 10 (l986) 1019.

[124] Y.X. Li, B.C. Liu, C.R. Loper, Study of the Solid-Liquid Interface during Unidirectional Solidification of Cast Iron, Transaction of American Foundry Society 101 (1990) 101.
[125] A. Hellawell, M.P. Wilkinson, Directional Freezing of Eutetcic Alloys Containing Graphite, Journal of Iron and Steel Institute, 203 (1965) 834-835.
[126] R.J. Brigham, G.R. Purdy, J.S. Kirkaldy, Unidirectional Solidification of Fe-C, Ni-C and Fe-C-Si Eutectics, Journal of Crystal Growth 20-24 (1967) 161-169.
[127] H. Morrogh, W.J. Williams, Graphite Formation in Cast Irons and in Nickel-Carbon and Cobalt-Carbon Alloys, Journal of Iron and Steel Institute, 155 (1947) 321–371.
[128] F. Hurum, Effect of Silicon Carbide in the Fe-FeSi-Fe_3C System, Modern Casting, 47 (1965) 77-88.
[129] H.D. Merchant, Solidification of Cast Iron- a Review of Literature in: H.D. Merchant (Ed.) Recent Research on Cast Iron Gordon and Breach, Detroit, MI, 1964, pp. 1-100.
[130] H. Morrogh, Graphite Formation in Grey Cast Iron and Related Alloys, BCIRA Journal of Research and Development, 5 (1955) 655-673.
[131] C.R. Loper, Ductile Iron Solidification Study using Electron Microscope, Transaction of American Foundry Society, 70 (1962) 963-967.
[132] M. Hillert, V.V.S. Rao, Gray and White Solidification of Cast Iron in: Solidification of Metals: Proceeding of the conference on solidification of metals Brighton 1967, pp. 204-211.
[133] S.V. Subramanian, D.A.R. Kay, G.R. Purdy, Graphite Morphology Control in Cast Iron in: H. Fredriksson, M. Hillert (Eds.) The Physical Metallurgy of Cast Iron Materials Research Society Stockholm, Sweden 1984, pp. 47-56.
[134] A.A. Chernov, The Spiral Growth of Crystals, Soviet Physics Uspekhi, 4 (1961) 116-148.
[135] D.D. Double, A. Hellawell, The structure of flake graphite in Ni-C eutectic alloy, Acta Metallurgica, 17 (1969) 1071-1083.
[136] I. Minkoff, B. Lux, Metallography in three dimensions. Some aspects of the microstructure of alloys containing silicon and graphite observed by scanning electron microscopy, Micron (1969), 2 (1970) 282-289.
[137] N.M.R. Peres, Graphene, new physics in two dimensions, Europhysics News 40 (2009) 17-20.
[138] A.K. Geim, K.S. Novoselov, The rise of graphene, Nat Mater, 6 (2007) 183-191.
[139] X. Lu, M. Yu, H. Huang, R.S. Ruoff, Tailoring graphite with the goal of achieving single sheets, Nanotechnology, 10 (1999) 269-272.
[140] Y. Zhang, J.P. Small, W.V. Pontius, P. Kim, Fabrication and electric-field-dependent transport measurements of mesoscopic graphite devices, APPLIED PHYSICS LETTERS 86 (2005) 073104-073101.
[141] A.M. Affoune, B.L.V. Prasad, H. Sato, T. Enoki, Y. Kaburagi, Y. Hishiyama, Experimental evidence of a single nano-graphene, Chemical Physics Letters, 348 (2001) 17-20.

[142] K.S. Novoselov, A.K. Geim, S.V. Morozov, D. Jiang, Y. Zhang, S.V. Dubonos, I.V. Grigorieva, A.A. Firsov, Electric Field Effect in Atomically Thin Carbon Films, Science, 306 (2004) 666-669.
[143] M.I. Katsnelson, Graphene: carbon in two dimensions, Materials Today, 10 20-27.
[144] C. Lee, X. Wei, J.W. Kysar, J. Hone, Measurement of the Elastic Properties and Intrinsic Strength of Monolayer Graphene, Science, 321 (2008) 385-388.
[145] I.W. Frank, D.M. Tanenbaum, A.M. van der Zande, P.L. McEuen, Mechanical properties of suspended graphene sheets, in, AVS, 2007, pp. 2558-2561.
[146] A.A. Balandin, S. Ghosh, W. Bao, I. Calizo, D. Teweldebrhan, F. Miao, C.N. Lau, Superior Thermal Conductivity of Single-Layer Graphene, Nano Letters, 8 (2008) 902-907.
[147] S. Ghosh, I. Calizo, D. Teweldebrhan, E.P. Pokatilov, D.L. Nika, A.A. Balandin, W. Bao, F. Miao, C.N. Lau, Extremely high thermal conductivity of graphene: Prospects for thermal management applications in nanoelectronic circuits, APPLIED PHYSICS LETTERS, 92 (2008) 151911-151913.
[148] S. Ghosh, W. Bao, D.L. Nika, S. Subrina, E.P. Pokatilov, C.N. Lau, A.A. Balandin, Dimensional crossover of thermal transport in few-layer graphene, Nat Mater, 9 (2010) 555-558.
[149] D.L. Nika, E.P. Pokatilov, A.S. Askerov, A.A. Balandin, Phonon thermal conduction in graphene: Role of Umklapp and edge roughness scattering, Physical Review B, 79 (2009) 155413.
[150] Y.-M. Lin, P. Avouris, Strong Suppression of Electrical Noise in Bilayer Graphene Nanodevices, Nano Letters, 8 (2008) 2119-2125.
[151] S. Qinghui, L. Guanxiong, D. Teweldebrhan, A.A. Balandin, S. Rumyantsev, M.S. Shur, Y. Dong, Flicker Noise in Bilayer Graphene Transistors, Electron Device Letters, IEEE, 30 (2009) 288-290.
[152] G. Liu, W. Stillman, S. Rumyantsev, Q. Shao, M. Shur, A.A. Balandin, Low-frequency electronic noise in the double-gate single-layer graphene transistors, APPLIED PHYSICS LETTERS, 95 (2009) 033103-033103.
[153] C. Berger, Z. Song, X. Li, X. Wu, N. Brown, C. Naud, D. Mayou, T. Li, J. Hass, A.N. Marchenkov, E.H. Conrad, P.N. First, W.A. de Heer, Electronic Confinement and Coherence in Patterned Epitaxial Graphene, Science, (2006) 1125925.
[154] C. Berger, Z. Song, T. Li, X. Li, A.Y. Ogbazghi, R. Feng, Z. Dai, A.N. Marchenkov, E.H. Conrad, P.N. First, W.A. de Heer, Ultrathin Epitaxial Graphite: 2D Electron Gas Properties and a Route toward Graphene-based Nanoelectronics, The Journal of Physical Chemistry B, 108 (2004) 19912-19916.
[155] C. Berger, Z. Song, X. Li, X. Wu, N. Brown, D. Maud, C. Naud, W.A.d. Heer, Magnetotransport in high mobility epitaxial graphene, physica status solidi (a), 204 (2007) 1746-1750.
[156] V.W. Brar, Y. Zhang, Y. Yayon, T. Ohta, J.L. McChesney, A. Bostwick, E. Rotenberg, K. Horn, M.F. Crommie, Scanning tunneling spectroscopy of inhomogeneous electronic structure in monolayer and bilayer graphene on SiC, APPLIED PHYSICS LETTERS, 91 (2007) 122102-122103.

[157] S.J. Chae, F. Gu¨nes, K.K. Kim, E.S. Kim, G.H. Han, S.M. Kim, H.-J. Shin, S.-M. Yoon, J.-Y. Choi, M.H. Park, C.W. Yang, D. Pribat, Y.H. Lee, Synthesis of Large-Area Graphene Layers on Poly-Nickel Substrate by Chemical Vapor Deposition: Wrinkle Formation, Adv. Mater. , 21 (2009) 2328–2333.
[158] K.S. Kim, Y. Zhao, H. Jang, S.Y. Lee, J.M. Kim, K.S. Kim, J.-H. Ahn, P. Kim, J.-Y. Choi, B.H. Hong, Large-scale pattern growth of graphene films for stretchable transparent electrodes, Nature, 457 (2009) 706-710.
[159] A. Reina, X. Jia, J. Ho, D. Nezich, H. Son, V. Bulovic, M.S. Dresselhaus, J. Kong, Large Area, Few-Layer Graphene Films on Arbitrary Substrates by Chemical Vapor Deposition, Nano Letters, 9 (2008) 30-35.
[160] Q. Yu, J. Lian, S. Siriponglert, H. Li, Y.P. Chen, S.-S. Pei, Graphene segregated on Ni surfaces and transferred to insulators, APPLIED PHYSICS LETTERS, 93 (2008) 113103-113103.
[161] A.J. Pollard, R.R. Nair, S.N. Sabki, C.R. Staddon, L.M.A. Perdigao, C.H. Hsu, J.M. Garfitt, S. Gangopadhyay, H.F. Gleeson, A.K. Geim, P.H. Beton, Formation of Monolayer Graphene by Annealing Sacrificial Nickel Thin Films, The Journal of Physical Chemistry C, 113 (2009) 16565-16567.
[162] Y. Gamo, A. Nagashima, M. Wakabayashi, M. Terai, C. Oshima, Atomic structure of monolayer graphite formed on Ni(111), Surface Science, 374 (1997) 61-64.
[163] A. Starodubov, M. Medvetskii, A. Shikin, V. Adamchuk, Intercalation of silver atoms under a graphite monolayer on Ni(111), Physics of the Solid State, 46 (2004) 1340-1348.
[164] H. Ueta, M. Saida, C. Nakai, Y. Yamada, M. Sasaki, S. Yamamoto, Highly oriented monolayer graphite formation on Pt(1 1 1) by a supersonic methane beam, Surface Science, 560 (2004) 183-190.
[165] J. Vaari, J. Lahtinen, P. Hautojärvi, The adsorption and decomposition of acetylene on clean and K-covered Co(0001), Catalysis Letters, 44 (1997) 43-49.
[166] A.L.V.d. Parga, F. Calleja, B. Borca, M.C.G.P. Jr, J.J. Hinarejo, F. Guinea, R. Miranda, Periodically rippled graphene: growth and spatially resolved electronic structure, Phys. ReV. Lett., 100 (5) (2008) 056807–056804.
[167] S. Marchini, S. Gunther, J. Wintterlin, Scanning tunneling microscopy of graphene on Ru(0001), Physical Review B (Condensed Matter and Materials Physics), 76 (2007) 075429-075429.
[168] P.W. Sutter, J.-I. Flege, E.A. Sutter, Epitaxial graphene on ruthenium, Nat Mater, 7 (2008) 406-411.
[169] N. Gall', E. Rut'kov, A. Tontegode, Interaction of silver atoms with iridium and with a two-dimensional graphite film on iridium: Adsorption, desorption, and dissolution, Physics of the Solid State, 46 (2004) 371-377.
[170] J. Coraux, A.T. N`Diaye, C. Busse, T. Michely, Structural Coherency of Graphene on Ir(111), Nano Letters, 8 (2008) 565-570.
[171] X. Li, W. Cai, J. An, S. Kim, J. Nah, D. Yang, R. Piner, A. Velamakanni, I. Jung, E. Tutuc, S.K. Banerjee, L. Colombo, R.S. Ruoff, Large-Area Synthesis of High-Quality and Uniform Graphene Films on Copper Foils, Science, 324 (2009) 1312-1314.

[172] Q. Yu, L.A. Jauregui, W. Wu, R. Colby, J. Tian, Z. Su, H. Cao, Z. Liu, D. Pandey, D. Wei, T.F. Chung, P. Peng, N.P. Guisinger, E.A. Stach, J. Bao, S.-S. Pei, Y.P. Chen, Control and characterization of individual grains and grain boundaries in graphene grown by chemical vapour deposition, Nat Mater, 10 (2011) 443-449.
[173] A. Guermoune, T. Chari, F. Popescu, S.S. Sabri, J. Guillemette, H.S. Skulason, T. Szkopek, M. Siaj, Chemical vapor deposition synthesis of graphene on copper with methanol, ethanol, and propanol precursors, Carbon, 49 (2011) 4204-4210.
[174] D. Geng, B. Wu, Y. Guo, L. Huang, Y. Xue, J.C.G. Yu, L. Jiang, W. Hu, Y. Liu, Uniform hexagonal graphene flakes and films grown on liquid copper surface, PNAS, Early Edition (2012).
[175] L.M. Viculis, J.J. Mack, R.B. Kaner, A Chemical Route to Carbon Nanoscrolls, Science, 299 (2003) 1361-.
[176] S. Stankovich, D.A. Dikin, G.H.B. Dommett, K.M. Kohlhaas, E.J. Zimney, E.A. Stach, R.D. Piner, S.T. Nguyen, R.S. Ruoff, Graphene-based composite materials, Nature, 442 (2006) 282-286.
[177] C. Liu, Z. Yu, D. Neff, A. Zhamu, B.Z. Jang, Graphene-Based Supercapacitor with an Ultrahigh Energy Density, Nano Letters, 10 (2010) 4863-4868.
[178] T. Georgiou, L. Britnell, P. Blake, R.V. Gorbachev, A. Gholinia, A.K. Geim, C. Casiraghi, K.S. Novoselov, Graphene bubbles with controllable curvature, APPLIED PHYSICS LETTERS, 99 (2011) 093103-093103.
[179] V. Tozzini, V. Pellegrini, Reversible Hydrogen Storage by Controlled Buckling of Graphene Layers, The Journal of Physical Chemistry C, 115 (2011) 25523-25528.
[180] D. Gosálbez-Martínez, J.J. Palacios, J. Fernández-Rossier, Spin-orbit interaction in curved graphene ribbons, Physical Review B, 83 (2011) 115436.
[181] X.H. Chen, H.S. Yang, G.T. Wu, M. Wang, F.M. Deng, X.B. Zhang, J.C. Peng, W.Z. Li, Generation of curved or closed-shell carbon nanostructures by ball-milling of graphite, Journal of Crystal Growth, 218 (2000) 57-61.
[182] V.L. Kuznetsov, A.L. Chuvilin, Y.V. Butenko, S.V. Stankus, R.A. Khairulin, A.K. Gutakovskii, Closed curved graphite-like structures formation on micron-size diamond, Chemical Physics Letters, 289 (1998) 353-360.
[183] D.V. Kosynkin, A.L. Higginbotham, A. Sinitskii, J.R. Lomeda, A. Dimiev, B.K. Price, J.M. Tour, Longitudinal unzipping of carbon nanotubes to form graphene nanoribbons, Nature, 458 (2009) 872-876.
[184] S.M. Winder, D. Liu, J.W. Bender, Synthesis and characterization of compound-curved graphite, Carbon, 44 (2006) 3037-3042.
[185] N. El-Kaddah, J. Szekely, Heat and fluid flow phenomena in a levitation melted sphere under zero gravity conditions, Metallurgical and Materials Transactions B, 15 (1984) 183-186.
[186] L. Jiao, B. Fan, X. Xian, Z. Wu, J. Zhang, Z. Liu, Creation of Nanostructures with Poly(methyl methacrylate)-Mediated Nanotransfer Printing, Journal of the American Chemical Society, 130 (2008) 12612-12613.
[187] A. Reina, X. Jia, J. Ho, D. Nezich, H. Son, V. Bulovic, M.S. Dresselhaus, J. Kong, Large Area, Few-Layer Graphene Films on Arbitrary Substrates by Chemical Vapor Deposition, Nano Letters, 9 (2009) 30-35.

[188] A.C. Ferrari, J.C. Meyer, V. Scardaci, C. Casiraghi, M. Lazzeri, F. Mauri, S. Piscanec, D. Jiang, K.S. Novoselov, S. Roth, A.K. Geim, Raman Spectrum of Graphene and Graphene Layers, Physical Review Letters, 97 (2006) 187401-187404.
[189] A. Gupta, G. Chen, P. Joshi, S. Tadigadapa, P.C. Eklund, Raman Scattering from High-Frequency Phonons in Supported n-Graphene Layer Films, Nano Letters, 6 (2006) 2667-2673.
[190] I. Calizo, F. Miao, W. Bao, C.N. Lau, A.A. Balandin, Variable temperature Raman microscopy as a nanometrology tool for graphene layers and graphene-based devices, APPLIED PHYSICS LETTERS, 91 (2007) 071913-071913.
[191] I. Calizo, A.A. Balandin, W. Bao, F. Miao, C.N. Lau, Temperature Dependence of the Raman Spectra of Graphene and Graphene Multilayers, Nano Letters, 7 (2007) 2645-2649.
[192] M.A. Pimenta, G. Dresselhaus, M.S. Dresselhaus, L.G. Cançado, A. Jorio, R. Saito, Studying disorder in graphite-based systems by Raman spectroscopy, Phys. Chem. Chem. Phys., 9 (2007) 1276 - 1290.
[193] I. Calizo, I. Bejenari, M. Rahman, G. Liu, A.A. Balandin, Ultraviolet Raman microscopy of single and multilayer graphene, Journal of Applied Physics, 106 (2009) 043509-043505.
[194] I. Calizo, W. Bao, F. Miao, C.N. Lau, A.A. Balandin, The effect of substrates on the Raman spectrum of graphene: Graphene- on-sapphire and graphene-on-glass, APPLIED PHYSICS LETTERS, 91 (2007) 201904-201903.
[195] Y.y. Wang, Z.h. Ni, T. Yu, Z.X. Shen, H.m. Wang, Y.h. Wu, W. Chen, A.T. Shen Wee, Raman Studies of Monolayer Graphene: The Substrate Effect, The Journal of Physical Chemistry C, 112 (2008) 10637-10640.
[196] E. Spiecker, A.K. Schmid, A.M. Minor, U. Dahmen, S. Hollensteiner, W. Jäger, Self-Assembled Nanofold Network Formation on Layered Crystal Surfaces during Metal Intercalation, Physical Review Letters, 96 (2006) 086401.
[197] T.G. Kollie, Measurement of the thermal-expansion coefficient of nickel from 300 to 1000 K and determination of the power-law constants near the Curie temperature, Physical Review B, 16 (1977) 4872.
[198] N. Mounet, N. Marzari, First-principles determination of the structural, vibrational and thermodynamic properties of diamond, graphite, and derivatives, Physical Review B, 71 (2005) 205214.
[199] W. Bao, F. Miao, Z. Chen, H. Zhang, W. Jang, C. Dames, C.N. Lau, Controlled ripple texturing of suspended graphene and ultrathin graphite membranes, Nat Nano, 4 (2009) 562-566.
[200] M.W. Barsoum, A. Murugaiah, S.R. Kalidindi, T. Zhen, Y. Gogotsi, Kink bands, nonlinear elasticity and nanoindentations in graphite, Carbon, 42 (2004) 1435-1445.
[201] P. Thrower, The study of defects in graphite by transmission electron microscopy, in: P. Walker (Ed.) Chemistry and physics of carbon, Marcel Dekker, NY.
[202] D. Graf, F. Molitor, K. Ensslin, C. Stampfer, A. Jungen, C. Hierold, L. Wirtz, Spatially Resolved Raman Spectroscopy of Single- and Few-Layer Graphene, Nano Letters, 7 (2007) 238-242.

[203] P.A. Thrower, The study of defects in graphite by transmission electron microscopy, in: Chemistry and physics of carbon, NY: Marcel Dekker, 1969.
[204] J.M. Blakely, Segregation to surfaces: Dilute alloys of the transition metals, Critical Reviews in Solid State and Materials Sciences, 7 (1978) 333 - 355.
[205] M. Eizenberg, J.M. Blakely, Carbon interaction with nickel surfaces: Monolayer formation and structural stability, The Journal of Chemical Physics, 71 (1979) 3467-3477.
[206] M. Eizenberg, J.M. Blakely, Carbon monolayer phase condensation on Ni(111), Surface Science, 82 (1979) 228-236.
[207] L.C. Isett, J.M. Blakely, Binding energies of carbon to Ni(100) from equilibrium segregation studies, Surface Science, 47 (1975) 645-649.
[208] L.C. Isett, J.M. Blakely, Binding of carbon atoms at a stepped-Ni surface, Journal of Vacuum Science and Technology, 12 (1975) 237-241.
[209] J.C. Shelton, H.R. Patil, J.M. Blakely, Equilibrium segregation of carbon to a nickel (111) surface: A surface phase transition, Surface Science, 43 (1974) 493-520.
[210] L.C. Isett, J.M. Blakely, Segregation isosteres for carbon at the (100) surface of nickel, Surface Science, 58 (1976) 397-414.
[211] A.A. Balandin, Chill Out: New Materials and Designs Can Keep Chips Cool, IEEE Spectrum, (Oct 2009) 29-33.
[212] J. Kim, R. Abbaschian, Influence of solidification variables on the microporosity formation on Al–Cu (4.5 wt%) alloy with axial heat processing, Journal of Materials Science, 46 (2011) 6213-6223.
[213] Metals Handbook, Atlas of Microstructures of Industrial Alloys, 8 ed., 1972.
[214] S. Berry, R. Hyers, B. Abedian, L. Racz, Modeling of turbulent flow in electromagnetically levitated metal droplets, Metallurgical and Materials Transactions B, 31 (2000) 171-178.
[215] R.T. Frost, M.C. Flemings, J. Szekely, N. El.Kaddah, Y. Shiohara, Electromagnetic Containerless Undercooling Facility and Experimnets for the Shuttle, Advanced Space Research, 4 (1984) 99-103.
[216] M.D. Nave, A.K. Dahl, D.H. StJohn, Eutectic Growth Morphologies in Magnesium-Aluminium Alloys, in: H.I. Kaplan, J.N. Hryn, B.B. Clow (Eds.) Magnesium Technology 2000, 2000, pp. 233-242.
[217] B. Lux, A. Vendl, H. Hahn, on the Formation of Microstructures in Grey Cast Iron, Crystal Research and Technology, 16 (1981) 531–556.
[218] W. Kurz, D.J. Fisher, Dendrite Growth in Eutectic Alloys: the Coupled Zone International Metals Review 24 (1979) 177-204.
[219] B. Lux, On the Theory of Nodular Graphite Formation in Cast Iron: Part II - Theorical Interpretation of the Experimental Observations Journal of Cast Metals Research, 2 (1972) 49-65.
[220] J.P. Hirth, On Two Dimensional Nucleation, Acta Metallurgica, 7 (1959) 755-756.
[221] B. Lewis, The Growth of Crystals of Low Supersaturation: I. Theory, Journal of Crystal Growth, 21 (1974) 29-39.
[222] D.R. Gaskell, Introduction to the Thermodynamics of Materials, Fourth Edition ed., Taylor and Francis 2009.

[223] K.A. Jackson, Kinetic Processes, WILEY-VCH, 2004.